

# Polarimetric Properties of Optically Resonant Nanostructures

by

Michael John Theisen

Submitted in Partial Fulfillment

of the

Requirements for the Degree

Doctor of Philosophy

Supervised by

Thomas Gordon Brown

The Institute of Optics

Arts, Sciences and Engineering

Edmund A. Hajim School of Engineering and Applied Sciences

University of Rochester

Rochester, New York

2015

UMI Number: 3686567

All rights reserved

INFORMATION TO ALL USERS

The quality of this reproduction is dependent upon the quality of the copy submitted.

In the unlikely event that the author did not send a complete manuscript and there are missing pages, these will be noted. Also, if material had to be removed, a note will indicate the deletion.



UMI 3686567

Published by ProQuest LLC (2015). Copyright in the Dissertation held by the Author.

Microform Edition © ProQuest LLC.

All rights reserved. This work is protected against unauthorized copying under Title 17, United States Code



ProQuest LLC.  
789 East Eisenhower Parkway  
P.O. Box 1346  
Ann Arbor, MI 48106 - 1346

# Biographical Sketch

Michael John Theisen was born on May 15, 1984 in West Bend, Wisconsin. He grew up outside of West Bend, where he started his education at Holy Angels Preschool at age 3, continued at Farmington Elementary School for kindergarten through fifth grade, and finished middle and high school in Kewaskum. In 2002, he moved to La Crosse, Wisconsin to begin his college career at the University of Wisconsin - La Crosse. As a freshman, he started out as a physics major with a biomedical emphasis where he did research with Prof. Thomas Kernozek. As a sophomore, he switched his major to physics with an optics emphasis, and started research with Prof. Michael Jackson, where he would work for the remaining three years. In 2006, he graduated with a B.S., double majoring of physics with an optics emphasis and mathematics. He was a member of Sigma Pi Sigma and Sigma Xi. He was awarded the physics department's "Outstanding Physics Senior Award." Later that year he moved to Rochester, New York to begin his graduate studies in optics at the The Institute of Optics at the University of Rochester. In 2007 he joined the group of Prof. Thomas G. Brown, where he began his work on a variety of topics covering polarization. A portion of that work will be presented in this thesis.

The following publications were a result of work conducted during doctoral study:

[A] M. J. Theisen, B. L. McIntyre, and T. G. Brown, Measurement of the polarimetric response of suspended gallium doped silicon nanowires, in SPIE BiOS (In-

ternational Society for Optics and Photonics, 2012), pp. 82 270P82 270P.

[B] M. J. Theisen and T. G. Brown, Phase effects in guided mode resonances: spectral phase, *Journal of Modern Optics*, in press (2014).

[C] M. J. Theisen and T. G. Brown, Phase effects in guided mode resonances II: Measuring the angular phase of a surface plasmon polariton, *Journal of Modern Optics*, accepted for publication pending minor revision (2014).

[D] M. J. Theisen and T. G. Brown, Phase effects in guided mode resonances III: parametric analysis and Fano resonances, *Journal of Modern Optics*, in press (2014).

# Acknowledgements

I wish to extend my sincerest thanks to Professor Thomas Brown, who for the past seven years has helped guide me through my research, and for his cultivation of a group of students that has often felt more like family than coworkers. He has helped me not only with my education over the years but with practically any issues that have arisen, from car problems to providing me a place to live when my apartment burned down. I also have to thank him for introducing me to Indian cuisine. I had been unaware of this wondrous food prior to my first of many group lunches.

I want to thank those members of the Brown group that I've had the pleasure to work with over the years, listed chronologically: Dr. Amber Beckley, Dr. Dean Brown, Dr. Alexis Spilman Vogt, Dillen Li, Roshita Ramkhalawon, Brandon Zimmerman, Dr. Jason Neiser, Guoke "Jerry" Yang, Katelynn Sharma, Anthony Vella and Steve Head. We had the "opportunity" of starting the lab anew, moving from Wilmot to Goergen; I still remember when Tom got annoyed at us for throwing away his box of expired foot powder, informing us that it was an excellent infrared reflector.

I'd like to thank Professor Michael Jackson, as he is the man who got me interested in optics in the first place. The opportunities that he provided allowed me to see the path that I wanted to follow. If not for him, I'd have never come to Rochester in the first place. I'd also like to thank Shekhar Guha and Leo Gonzalez

for allowing me to work in their laboratory at Wright Patterson Air Force Base. The valuable experience I gained while working on experiments in their lab came in quite useful when I started at the Institute.

I'd also like to thank Brooke Beier, it is always easier to move somewhere new when you know that you already have a friend there.

Throughout my research, I needed to fabricate many different types of samples and through it all, Brian McIntyre was always willing to provide advice. He taught me how to use almost every piece of equipment I needed, and if not for his help I'm certain my samples would not have come out as well as they have. He taught me many lessons over the years. Once, we were trying to get the thermal evaporator working, but it kept tripping the circuit breaker. We started taking a look at the power supply, and when we compared it to the wiring diagram we noticed a small red wire in the power supply that wasn't in the wiring diagram. When we took it out the the evaporator started working. I still think that you were the one that originally put that jumper in there. I'd like to thank Alex Mann, Sergey Korjenevski, and Donnell Jackson for all their time spent with me in URnano with Brian, as well as our boss, Professor Nicholas Bigelow. The weekly meetings were a blast with all of you, even if they were a waste of time. I'd also like to thank our Zeiss microscope service representative, Tom Rathgeb, for keeping our SEM/FIB in nearly working order most of the time. I'd like to thank Dr. Neil Lafferty for his help at the RIT cleanroom. It was a great help both for the fabrication advise, as well as the information he taught me about cleanrooms. This knowledge helped when setting up the clean room here with the URnano folks.

The department administrators and optics staff: Lori, Gina, Noelene, Gale, Betsy, Lissa and Kari deserve our thanks for the work that they do everyday to keep this department running smooth. I'd like to thank Per Adamson for all the equipment that I borrowed throughout my time here. Without the help and support you provide when students need something to finish a setup, far less

research would get accomplished here at the Institute.

Thanks to Dr. Miguel Alonso and Dr. Jon Ellis for their help and guidance on the IBM project. I'm looking forward to see how the system develops in my absence.

Thanks to my officemate Tony Visconti, for always being willing to talk football.

I'd like to thank my closest friends: Amber Beckley, Jordan Leidner, and Nick Hamala for all the good times we've had together. Without you guys my time spent in Rochester would not have been as fun as it has been.

Special thanks to Luke Reilly for introducing me to the joys of Tichu; weekly sessions with Kara Morse, Frank Dinoff, Jordan Leidner, and him were often a highlight of my week.

I would like to give my deepest thanks and acknowledgement to my parents, John and Michele. They have always believed in me, and if not for their love and support, I'd never have been able to accomplish what I have. I'd also like to thank the rest of my immediate family: Jennie, Brian, Xander, Xavier, Xane and Xack, and to Nick, Terisha, and little Elijah, who only get to see me twice a year, but have always been supportive.

# Abstract

Optically resonant nanostructures have been incorporated into a variety of devices used in a number of different fields. In this thesis, we explore optically resonant nanostructures in two forms.

First we investigate a relatively new material, gallium implanted silicon (Si:Ga). We cover the fabrication process and experimentally find the optical properties as a function of both dose and wavelength. We then use the properties of this new material to create suspended arrays of Si:Ga nanowires, and determine their optical characteristics.

In the second part of this thesis, we use more conventional materials and fabrication procedures to investigate the phase effects of guided mode resonators. We look at the *spectral* phase effects for a grating coupled silicon-on-insulator based guided mode resonator. We also look the *angular* phase effects of a surface plasmon polariton based guided mode resonator, comparing experimental results to theory calculated with rigorous coupled wave analysis for both cases. In addition, the guided mode resonance is modeled as a Fano resonance to gain insight into the functional form of the phase. Knowing the phase response of guided mode resonances may allow the creation of guided mode resonance based devices with higher sensitivity than traditional reflectance based devices.

## Contributors and Funding Sources

This work was supported by a dissertation committee consisting of Professor Thomas G. Brown (advisor), Assistant Professor A. Nickolas Vamivakas and Professor Gary W. Wicks of The Institute of Optics, and Associate Professor Zeljko Ignjatovic of the Department of Electrical and Computer Engineering. The thin film code used in chapters 2 and 4, the multi-parameter simplex optimization code, code used to register images for the polarimetric microscope algorithm, and part of the Fourier phase extraction code was written by Thomas Brown, as well as the Fano phase derivation in chapter 6. Our RCWA software is implemented on a Matlab platform and includes code credited to Song Peng, Jason Neiser, Robert Fabrizio and Thomas Brown. The initial version of the experimental setup used for chapter 4 was put together by Dr. Jason Neiser and Guoke Yang. All other work conducted for the dissertation was completed by the student. Graduate study was supported by grants from the National Science Foundation, working part-time for URnano nanofabrication facility, and contributions from the International Business Machines Corporation.

# Table of Contents

<b>Biographical Sketch</b>	<b>ii</b>
<b>Acknowledgements</b>	<b>iv</b>
<b>Abstract</b>	<b>vii</b>
<b>Contributors and Funding Sources</b>	<b>viii</b>
<b>List of Figures</b>	<b>xii</b>
<b>1 Introductory Concepts</b>	<b>1</b>
1.1 Polarization . . . . .	1
1.1.1 Mueller Calculus . . . . .	7
1.1.2 Jones Calculus . . . . .	8
1.2 Waveguides . . . . .	9
1.3 Guided Mode Resonances . . . . .	9
1.4 Surface Plasmon Polaritons . . . . .	13
1.5 Nanofabrication . . . . .	14
1.5.1 Parallel vs. Series methods . . . . .	14
1.5.2 Fabrication Platform . . . . .	16
1.6 Nanostructure Modeling . . . . .	17
1.6.1 Basic Slab Model for Waveguides . . . . .	17
1.6.2 Thin Film Stack Modeling . . . . .	23
1.6.3 Rigorous Coupled Wave Analysis . . . . .	26
1.7 Thesis Chapter Breakdown . . . . .	27
<b>2 Optical Properties of Gallium Implanted Silicon</b>	<b>29</b>
2.1 Introduction . . . . .	29
2.2 Implantation - Sample Fabrication . . . . .	31
2.2.1 Determination of the Milling Rate at Standard Operating Parameters ( $30kV\text{Ga}^+$ ) . . . . .	34
2.3 Implantation Model - Ion Ranging Statistics . . . . .	35
2.4 Si:Ga Elipsometry - Experimental Results . . . . .	37

2.5	Broadband Measurement of Si:Ga Optical Properties . . . . .	40
2.6	Drude Model . . . . .	43
2.7	Implantation Masks . . . . .	45
2.7.1	Aluminum Oxide Masks . . . . .	46
2.7.2	Silicon Dioxide Masks . . . . .	47
2.7.3	Carbon Masks . . . . .	48
2.8	Discussion of Applications . . . . .	49
2.9	Conclusion . . . . .	52
<b>3</b>	<b>Fabrication, Measurement, and Analysis of Gallium Implanted Silicon Nanostructures</b>	<b>53</b>
3.1	Introduction . . . . .	53
3.2	Sample Fabrication . . . . .	54
3.2.1	Gallium Implantation . . . . .	54
3.2.2	Sample Processing . . . . .	57
3.3	Polarimetric Microscope . . . . .	60
3.4	Sample Jones Matrix Retrieval Algorithm . . . . .	62
3.5	Polarization Properties of Si:Ga Nanowires . . . . .	65
3.6	Nanowire Thickness . . . . .	67
3.7	Rigorous Coupled Wave Analysis . . . . .	67
3.8	Discussion and Conclusions . . . . .	74
<b>4</b>	<b>Spectral Phase Effects in Guided Mode Resonances</b>	<b>75</b>
4.1	Introduction . . . . .	75
4.2	Waveguide Description and Fabrication . . . . .	77
4.3	Measuring the Optical Response . . . . .	78
4.4	Amplitude and Phase Measurement . . . . .	80
4.5	Discussion . . . . .	82
4.6	Conclusion . . . . .	86
<b>5</b>	<b>Angular Phase Effects in Guided Mode Resonances</b>	<b>88</b>
5.1	Introduction . . . . .	88
5.2	Sample Description and Fabrication . . . . .	90
5.3	Measuring the Optical Response . . . . .	91
5.4	Discussion of Results . . . . .	97
5.5	Conclusion . . . . .	100
<b>6</b>	<b>The Parametric Plot: A New Way of Looking at Guided Mode Resonances</b>	<b>103</b>
6.1	Introduction . . . . .	103
6.2	The Phase of the Fano Resonance . . . . .	105
6.3	The Generalized Fano Resonance . . . . .	108
6.4	Parametric Analysis in the Design of Guided Mode Resonances . . . . .	109
6.5	Experimental Example . . . . .	111
6.6	Discussion . . . . .	114
6.7	Conclusion . . . . .	117

<b>7 Conclusions and Future Work</b>	<b>118</b>
<b>Bibliography</b>	<b>124</b>
<b>A Si:Ga Nanowire Fabrication Using a Focused Ion Beam (FIB)</b>	<b>131</b>
<b>B FIB Beam Start-up Troubleshooting Guide</b>	<b>144</b>
<b>C Sample Fabrication Using Electron Beam Lithography (Nanopattern Generation System)</b>	<b>147</b>
<b>D Fabrication of Silver Guided Mode Resonators</b>	<b>155</b>
<b>E Fano Phase Derivation</b>	<b>157</b>

# List of Figures

1.1	The Poincaré sphere. . . . .	7
1.2	Guided mode resonance filter reported by Magnusson and Wang where $n_{cover} = 1$ , $n_{1h} = 2.42$ , $n_{1l} = 2.28$ , $n_2 = 1.38$ , $n_{substrate} = 1.52$ , $d_1 = 404$ nm, $d_2 = 688$ nm and $\Lambda = 1$ $\mu\text{m}$ for normal incidence. . . . .	11
1.3	Top: Neiser Optically Resonant Periodic Electrode (ORPEL) GMR structures viewed in visible light. Bottom: Reflectance spectra from gratings of varying period. . . . .	12
1.4	Diagram of the slab model waveguide. . . . .	18
1.5	Diagram of the propagating waves used for the thin film model. . . . .	23
2.1	Light microscope and AFM images of sample 1. . . . .	32
2.2	Light microscope and SEM images of sample 2. . . . .	33
2.3	AFM slice through all three pads on sample 1 (figure 2.1(b)). . . . .	34
2.4	SRIM Monte Carlo simulation of 50,000 $\text{Ga}^+$ accelerated at 30kV implanted into silicon. . . . .	35
2.5	Simplistic normalized gallium profile (figure 2.4) taking milling into account. Dashed curve shows the equilibrium case. . . . .	36
2.6	Diagram of the ellipsometric experimental setup. . . . .	37
2.7	Left: Geometry used for thin film model consisting of a 40 nm implanted region with unknown refractive indices $n$ and $k$ on top of a 40 nm region of disordered (amorphous) silicon. Right: Example set of Stokes parameters (S1,S2,S3) vs angle on reflection off a 0.3 $\text{nC}/\mu\text{m}^2$ Si:Ga pad on silicon at 632.8 nm. Lines shown are plotted from the thin film model fit to the data. . . . .	38
2.8	Refractive index (n and k) vs dose for four Si:Ga pads at 532nm and 632.8nm. Lines shown are a guide to the eye. The diamonds and squares represent the measurements of Fried et. al. for amorphous silicon. . . . .	39
2.9	Broadband reflectance data from a 0.1 $\text{nC}/\mu\text{m}^2$ dose Si:Ga pad. Upper: Reflectance from a BK7/Air/Si:Ga structure; Lower: Reflectance from a bare Si:Ga pad. . . . .	41
2.10	Thin film fit of optical constants n and k versus wavelength for pads with gallium implantation doses of 0.1 and 0.3 $\text{nC}/\mu\text{m}^2$ . . . . .	42
2.11	Plasmonic quality factor ( $Q_{\text{SPP}}$ and $Q_{\text{LSP}}$ ) of 0.3 $\text{nC}/\mu\text{m}^2$ Si:Ga. . . . .	43

2.12	Real and imaginary parts of the dielectric function plotted vs. $\omega$ for silver, gold and $0.3\text{nC}/\mu\text{m}^2$ Si:Ga. Drude model shown with dotted lines for the materials. . . . .	45
2.13	SRIM - $30\text{kV}$ $\text{Ga}^+$ implanted into $\text{SiO}_2$ mask on silicon. . . . .	47
2.14	SRIM - $30\text{kV}$ $\text{Ga}^+$ implanted into $\text{SiO}_2$ mask on silicon. . . . .	48
2.15	Si:Ga: carbon mask . . . . .	49
2.16	AFM slice through all three pads of the Si:Ga: carbon mask sample. . . . .	50
2.17	SEM micrograph of a Si:Ga sample dose array ( $0.01 - 0.25\text{nC}/\mu\text{m}^2$ ) following a 30 minute bake at $250^\circ\text{C}$ . . . . .	51
3.1	SEM micrograph of Si:Ga dose array following a ten minute RIE etch in 30:1 Ar: $\text{SF}_6$ taken at $54^\circ$ and a tilt compensation of $36^\circ$ . . . . .	55
3.2	SEM micrograph of gallium implantation taken at $54^\circ$ and a tilt compensation of $36^\circ$ . . . . .	56
3.3	Comparison of different reactive ion etch recipes. . . . .	58
3.4	Comparison of air dried and critical point dried wet etched nanowire arrays. . . . .	59
3.5	Schematic design of the polarimetric microscope. . . . .	61
3.6	SEM micrograph and retardance of linear nanowires. . . . .	66
3.7	Orientation of the retardance and diattenuation of linear nanowires. . . . .	68
3.8	SEM micrograph and retardance of concentric circle nanowires. . . . .	69
3.9	Orientation of the retardance and diattenuation of concentric circle nanowires. . . . .	70
3.10	SEM micrograph of a Si:Ga nano-ribbon taken at $54^\circ$ with tilt compensation of $36^\circ$ . . . . .	71
3.11	Rigorous coupled wave analysis of Si:Ga nanowire array. . . . .	73
4.1	Cross-sectional view of silver GMR structure under test. . . . .	78
4.2	Experimental setup. The rotating diffusor is inserted for viewing and alignment. The dashed (solid) line shows the light path in the tangential (sagittal) plane of the cylindrical lens. . . . .	79
4.3	Spectrogram used for amplitude and phase analysis. (a) Interference between then normalized reflected signal and the substrate reflection. (b) Fringes after Fourier filtering. . . . .	80
4.4	Experimental data compared with the RCWA fit for (a) reflection and (b) phase. An arbitrary offset has been added to the phase plots for display. . . . .	81
4.5	Comparison of the RCWA fit with several models. Left: RCWA fit compared with the design target; Right: RCWA fit compared with two different slab waveguide models . . . . .	85
4.6	Electric field reconstruction of the TE mode of our sample using the multi-layer mode solver. The TE resonance of our structure uses first order grating coupling into the 15 <sup>th</sup> order waveguide mode. . . . .	86
5.1	Illustrations showing the grating geometry and orientation with respect to the illumination of the microscope entrance pupil. . . . .	90

5.2	Experimental setup with lens set to the Bertrand configuration. The rotating diffuser is inserted for viewing and alignment. . . .	92
5.3	Calcite, Wollaston prism and analyzer combination used to interfere TE and TM polarization. Calcite optical axes are displayed in red. The incident beam is a mixture of TE and TM light and ends polarized at $45^\circ$ due to the analyzer. . . . .	93
5.4	Raw data taken of a structure with 981 nm corrugated silver grating. Multiple reflections off surfaces of the microscope objective can be seen in the center of the field, along with scatter from other contaminants throughout the field. The square root of the measured intensity is plotted to make the edge of the pupil more visible; it also reduces the appearance of the non uniform illumination. . . .	94
5.5	Experimental and theoretical phase response (in waves) of a 981 nm period corrugated silver layer on fused silica. . . . .	95
5.6	Experimental and theoretical phase response (in waves) of a 956 nm period corrugated silver layer on fused silica. . . . .	95
5.7	Experimental and theoretical reflectance of a 981 nm period corrugated silver layer on fused silica. . . . .	96
5.8	Experimental and theoretical reflectance of a 956 nm period corrugated silver layer on fused silica. . . . .	96
5.9	Microscope pupil images overlaid with the solution to equation 5.3 given that $\varepsilon_{Ag} = -46 - 3.36i$ for a wavelength of $\lambda = 1064$ nm. . .	97
5.10	Slices through the phase and reflectance plots for both experiment and RCWA for analysis. . . . .	98
5.11	Theoretical TE reflectance and phase of a 713 nm period silver guided mode resonator. . . . .	101
5.12	Theoretical TM reflectance and phase of a 713 nm period silver guided mode resonator. . . . .	101
5.13	Experimental results of the reflectance vs angle of the grating-coupled silver guided mode resonator described in chapter 4. . . .	102
6.1	Parametric plot showing the amplitude and phase of the Fano resonance for various values of the asymmetry parameter $q$ . The circles indicate the endpoints of the spectrum. . . . .	106
6.2	The Fano resonance for all values of $q$ when each is rotated by the phase $\psi(q)$ . Left: Geometry of the rotation. Right: Three values of $q$ rotated to the real axis. The symbols indicate the end points for the trajectories: asterisk: $q = +0.5$ ; diamond: $q = 0$ ; circle: $q = -0.5$ . . . . .	107
6.3	The Fano resonance for three values of $q$ in which the imaginary part varies while the real part is 0. . . . .	109
6.4	Diagram of example structure. The thicknesses are as follows: silicon waveguide layer, $2.411 \mu\text{m}$ ; buried oxide, $1.080 \mu\text{m}$ ; $\text{SiO}_2$ isolation layer, $110 \text{ nm}$ ; grating layer, $18 \text{ nm}$ ; the oxide cap layer is varied to control the coupling conditions ( $80 - 106 \text{ nm}$ ). . . . .	110
6.5	Examples of critically coupled, under coupled and over coupled resonances modeled using rigorous coupled wave analysis. Each structure is based on the structure shown in figure 6.4, each differing by $13 \text{ nm}$ in the $\text{SiO}_2$ cap layer thickness. . . . .	110

6.6	Parametric representation of three designs. The experiment is shown in the dashed (red) circle . . . . .	112
6.7	Reconstruction of the fringe pattern using a Fano resonance model (solid line) compared with the normalized spectrum from the OSA (data points). The spectral width FWHM of the Fano resonance is 0.34 nm; $q = .022 + 0.37i$ ; the quadratic phase correction was $-1.71 \times 10^4 rad/nm^2$ . . . . .	113
6.8	Amplitude and Phase of the resonance extracted from the experimental fit of figure 6.7. . . . .	114
7.1	Initial Si:Ga nanowire emission results. Sample was fabricated on a commercial silicon wafer, and consisted of two Si:Ga pads separated by Si:Ga nanowires. . . . .	121
7.2	Si:Ga guided mode resonator fabricated in a silicon on glass substrate.	123

# Chapter 1

## Introductory Concepts

### 1.1 Polarization

In this thesis, we will be discussing the polarimetric properties of a variety of optically resonant nanostructures. To understand this, we will first lay out one of the foundations of optics, polarization. The nature of light was debated for hundreds of years, and there were two main theories of light that were put forth. The corpuscular theory of light stated that light was a particle, whereas the wave theory stated that light was a wave phenomenon. One of the reasons the debate lasted for so long was because light seemed to have properties of both of these things (particles and waves). In the early 1600s, René Descartes viewed light to be a pressure (longitudinal) wave that propagated in a perfectly elastic medium (the æther), and he attributed color to arise from different velocities of particles in this medium. By 1676, Olaf Römer discovered that light had a finite speed from observations of Jupiter's moons[1]. In 1669, Erasmus Bartholinus discovered that if an ordinary beam of light is passed through Icelandic spar (a crystal similar to calcite which is shown in figure 5.3), the light will split into two spots of equal intensity [2]. Icelandic spar is what we now know to be a uniaxial crystal, which has a different refractive index depending on the polarization of light. One of

the spots (ordinary ray) seemed to obey the normal law of refraction while the other (extraordinary ray) did not. This particular property, later termed double refraction, was unable to be explained with the theories of light that existed at the time, and was a leading cause for others to begin working out explanations for what we now know as the polarization of light. Three years later, Christiaan Huygens demonstrated that a second piece of calcite oriented correctly could be used to extinguish one of the beams of light, and that to extinguish the other beam, the crystal needed to be rotated ninety degrees. In 1690, he published his famous book on optics entitled, *Traité de la lumière* [3], which detailed a revolutionary new view of light, in which light behaved as a superposition of spherical waves emitted from a source. Each point in space that the light hits becomes a secondary source of spherical waves, and all these spherical waves are added together to obtain the propagating wavefront.

The leading opponent to the wave theory was arguably Sir Isaac Newton, who supported a corpuscular theory of light; he viewed light as a stream of small particles with variations in color corresponding to particles of different size and mass. This suggested that physicists should use standard Newtonian mechanics to model light-matter interactions. Since this theory was put forth with his theories on gravity that were validated by correctly predicting Haley's comet's return in 1758, the corpuscular theory of light remained the accepted scientific view of light until the experiments of Thomas Young in 1801. Young showed that under certain conditions, two beams of light can constructively and/or destructively interfere, this is readily understood in the wave interpretation, but is impossible to explain using the corpuscular theory. Two years later, he gave a lecture to the Royal Society of London on a series of experiments done with sunlight and pinholes [4].

In 1808 Étienne-Louis Malus discovered that light can become polarized when it reflects off a planar interface. He was able to determine this by looking at the reflection off windows and extinguishing the reflection with a piece of Icelandic

spar. He determined experimentally that the intensity through the second crystal fell off as the cosine squared when the crystal was rotated, what is now termed Malus' Law. Four years later, Sir David Brewster was able to determine that the incident angle at which unpolarized light is reflected as fully polarized light depends on the composition (refractive index) of the two materials that make up the interface. This angle is now known as "Brewster's angle", and is defined as the arctangent of the ratio of the refractive indices of the two dielectrics.

In 1815, Jean-Baptiste Biot discovered optical activity in various liquids [5], which is the rotation of linearly polarized light as it propagates through the medium. In 1822 Sir John Herschel discovered that the optical rotation properties in quartz are caused by the crystallographic structure [6; 7], and in 1848, Louis Pasteur published his Ph.D. thesis discussing how molecular symmetry leads to optical rotation in certain solutions [8].

At this time, the particle vs. wave nature of light was still being debated, and to this end, in 1818 the French Academy of Sciences had a competition to see who could come up with the best theory to explain how diffraction works. Augustin Jean Fresnel submitted an entry detailing a scalar wave theory of light. One of the judges for the competition was Siméon Denis Poisson, who was a proponent of Newton's corpuscular theory. After studying Fresnel's entry, he determined that if his wave theory was correct, then if a circular obscuration was illuminated, some distance behind the mask a bright spot would appear. He believed that the existence of the bright spot was preposterous since there was no way to explain this spot with his corpuscular views, and thus wanted to reject the theory. The head of the competition committee, Dominique-François-Jean Arago, decided to set up an experiment to test if this spot was real, and found it did indeed occur. To this day the spot is named the Poisson spot in "honor" of the person who discovered its existence. It should be noted that this spot was seen by Delisle [9] and Maraldi [10] over 100 years prior to this competition. By 1823, Fresnel

had refined his theory using a basis of the elastic theory of æther to calculate the reflection and transmission amplitudes of a plane wave of light impinging upon a dielectric interface, now known as the Fresnel coefficients [11]. By the 1830's, most scientist were convinced by the experimental evidence that light was indeed a transverse wave, but a full explanation of the optical field was not yet known.

Hans Christian Ørsted constructed an experiment where he was able to affect a magnetic compass needle by running electric current through a loop of wire, in 1820[12]. This was a landmark experiment in the history of light, since it was the first to show the direct connection between electricity and magnetism. The magnetic force for a long coil of wire appeared to have a cylindrical shape. In 1831, Michael Faraday discovered electromagnetic induction. He took an iron ring, and wrapped two insulated wires around opposite sides of it. He found that he could induce a transient current (measured with a galvanometer) though one wire when he connected the opposite wire to a battery; he also noted that when he disconnected the battery, a current was induced in the opposite wire again, but this time the current flowed in the opposite direction. It was upon the experimental work of Faraday that James Clerk Maxwell tried to develop a unified mathematical theory of electromagnetism. In 1864, he published his seminal paper on it entitled, "A dynamical theory of the electromagnetic field," in which he put forth his theory describing how electromagnetic waves propagate through space (æther). This theory was refined over the years, and in 1873 Maxwell published a textbook entitled "A Treatise on Electricity and Magnetism," in which he distilled his previous equations from 1864 to four differential equations that are now called Maxwell's equations. The modern form of Maxwell's equations, in their vector form, was first constructed by Oliver Heaviside in the 1890's:

$$\nabla \times \mathbf{H} = \frac{\partial \mathbf{D}}{\partial t} + \mathbf{J} \quad (1.1)$$

$$\nabla \times \mathbf{E} = -\frac{\partial \mathbf{B}}{\partial t} \quad (1.2)$$

$$\nabla \cdot \mathbf{D} = \rho \quad (1.3)$$

$$\nabla \cdot \mathbf{B} = 0 \quad (1.4)$$

The mathematical formalism was then set in place which described how the electric and magnetic fields of light are orthogonal waves that oscillate transverse to the direction of propagation.

A major advancement in the field was introduced in 1852 by Sir George Gabriel Stokes, who proposed the use of four *measurable* quantities to describe the polarization of light. These parameters are now put together in a 4 element column vector called the Stokes Vector.

The mid 20th century was a time of big advances in polarization, as there were two major polarization analysis methods developed. In 1941 R. Clark Jones published his first of many papers on his new calculus, in which he breaks light into its x and y electric fields (Jones vector) and uses  $2 \times 2$  matrices to model polarization elements [13]. In 1947, Jones published a new paper where he talks about “The More Powerful Calculus,” which acts on Stokes parameters directly [14]; this new calculus was being developed by Hans Mueller. Mueller published the method in a classified journal in 1943 [15], but it wasn’t until he started lecturing about it in 1945 that it became more well known. Mueller and Jones Calculi are covered in a bit more detail in sections 1.1.1 and 1.1.2 respectively.

When we talk about the polarization of light, we are referring to the orientation of the *electric* field. In general, the electromagnetic field is often written as a

harmonic plane wave that can be separated into its Cartesian components [16],

$$\begin{aligned} E_x &= a_1 \cos(\tau + \delta_1) \\ E_y &= a_2 \cos(\tau + \delta_2) \end{aligned} \quad \text{for } (a_1, a_2 > 0), \quad (1.5)$$

where  $\tau$  denotes the variable part of the phase factor. With a bit of algebra, we square and sum these two equations to obtain the shape that the electric field traces in time. We get,

$$\left(\frac{E_x}{a_1}\right)^2 + \left(\frac{E_y}{a_2}\right)^2 - 2\frac{E_x}{a_1}\frac{E_y}{a_2}\cos\delta = \sin^2\delta, \quad (1.6)$$

where  $\delta = \delta_2 - \delta_1$ . This is the equation of an ellipse. Thus in general, the electric field will trace out an ellipse in time. There are a few interesting points to consider when looking at equation 1.6. First, we can see that for cases where  $\delta = m\pi$  (where  $m$  is an integer) we get linear polarization. A linearly polarized beam of light has an electric field that oscillates in a plane parallel to propagation. For  $0 < \delta < \pi$ , we get left-handed elliptical polarization. Left-handed polarized light has an electric field vector that rotates clockwise in time when looking toward the source. For  $\pi < \delta < 2\pi$  we get right-handed elliptical polarization, whose electric field vector rotates counter-clockwise when looking toward the source. The last special case is circular polarization, which occurs when  $a_1 = a_2$  and  $\delta = +/\!-\frac{\pi}{2}$  for right-hand circular and left-hand circular polarization respectively. An easy way to visualize all of the different polarization states is to use the Poincaré sphere, as seen in figure 1.1. It maps all the linear polarization states to the equator of a sphere, right-hand and left-hand elliptical polarizations occupy the upper and lower hemispheres respectively, with right-hand and left-hand circular displayed at the north and south poles respectively. There have been a variety of methods created for handling calculations of the polarization of light as it interacts with various elements in a system. The two main methods are Mueller calculus and

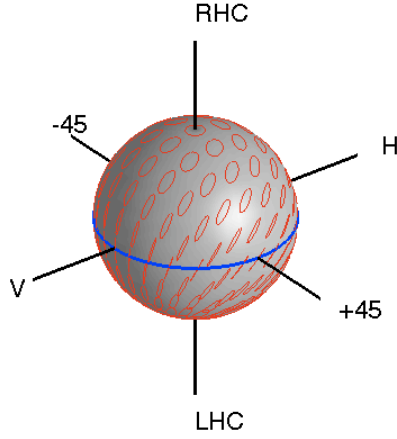


Figure 1.1: The Poincaré sphere.

Jones calculus.

### 1.1.1 Mueller Calculus

Mueller calculus represents the polarization of a beam of light with a four dimensional vector quantity. If we represent the  $x$  and  $y$  components of the electric field as,

$$\begin{aligned} E_x(t) &= E_{0x}e^{-i(\omega t + \delta_x(t))} \\ E_y(t) &= E_{0y}e^{-i(\omega t + \delta_y(t))}, \end{aligned} \quad (1.7)$$

where  $E_{0x}$  and  $E_{0y}$  are the instantaneous amplitudes,  $\omega$  is the angular frequency, and  $\delta_x(t)$  and  $\delta_y(t)$  are the instantaneous phase factors. The four dimensional Stokes vector is then defined as,

$$\mathbf{s} = \begin{pmatrix} S_0 \\ S_1 \\ S_2 \\ S_3 \end{pmatrix} = \begin{pmatrix} |E_{0x}|^2 + |E_{0y}|^2 \\ |E_{0x}|^2 - |E_{0y}|^2 \\ 2\text{Re}[E_{0y}^* E_{0x}] \\ -2\text{Im}[E_{0y}^* E_{0x}] \end{pmatrix}, \quad (1.8)$$

Polarization elements are expressed as a  $4 \times 4$  real valued matrix, and the output Stokes vector for a beam interacting with an element is simply,

$$\mathbf{S}_{out} = \mathbf{M}\mathbf{S}_{in}, \quad (1.9)$$

where  $\mathbf{M}$  is a Mueller matrix for a polarization element. Mueller calculus is able to handle partially polarized light, as well as elements that have depolarization (the reduction of the degree of polarization of light that passes through them). One thing that Stokes vectors can not take into account is a global phase.

### 1.1.2 Jones Calculus

Jones calculus uses a two dimensional complex valued vector to describe an electric field, and a  $2 \times 2$  complex valued matrix to represent polarization elements. If we take an electric field as stated in equation 1.7, then the Jones vector representation is,

$$\mathbf{J} = \begin{pmatrix} E_x \\ E_y \end{pmatrix} = \begin{pmatrix} E_{0x}e^{i\delta_x} \\ E_{0y}e^{i\delta_y} \end{pmatrix}, \quad (1.10)$$

which is often rewritten as,

$$\mathbf{J} = \begin{pmatrix} E_x \\ E_y \end{pmatrix} = Ae^{i\phi} \begin{pmatrix} \cos \Psi \\ \sin \Psi e^{i\Delta} \end{pmatrix}, \quad (1.11)$$

where  $A$  is the amplitude of the field,  $\phi = \delta_x$  is the global phase,  $\tan \Psi = \left| \frac{E_{0y}}{E_{0x}} \right|$ , and  $\Delta = \delta_y - \delta_x$  is the relative phase between  $x$  and  $y$  components, thus Jones calculus is able to model global phase. One drawback is that it is unable to model partially polarized light or any depolarization in elements.

## 1.2 Waveguides

The function of a waveguide is exactly as the name implies; when applied to optics, it describes a structure that is used to guide electromagnetic waves. The first waveguide was proposed by J.J. Thomson in 1893, for use with microwaves, and consisted of a hollow metal tube [17]. For the purpose of this thesis, we'll restrict ourselves to visible and near-infrared optical waves of the electromagnetic regime. An optical waveguide can be used to confine light in either one or two dimensions depending on waveguide geometry. A slab waveguide can be used to confine the light into a two dimensional sheet, and is typically constructed of three planar dielectric (lossless) layers. Light is confined in the core (center layer) by total internal reflection. To do this, the refractive index of the core layer must be higher than that of the substrate (bottom layer) and the cover (top layer), as seen in figure 1.4. The mathematics of the slab waveguide model are covered in section 1.6.1. Examples of waveguides that confine light to propagated in one dimension are optical fibers and rib and slot waveguides.

## 1.3 Guided Mode Resonances

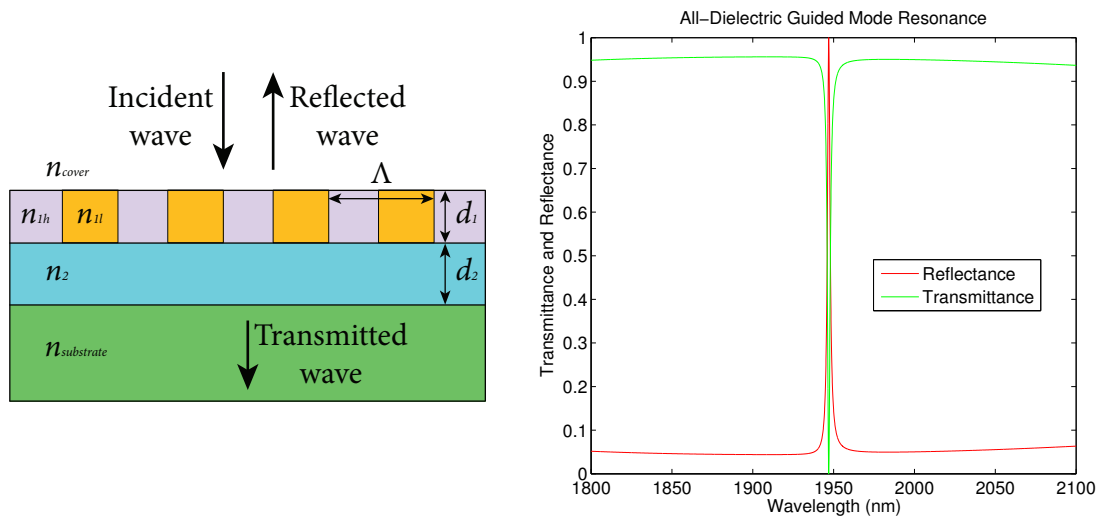
Guided mode resonances have been studied since the early 1900's, although not necessarily under that name. In 1902, Robert W. Wood published a paper entitled "On a Remarkable Case of Uneven Distribution of Light in a Diffraction Grating Spectrum [18]." In this paper, Wood describes two different types of anomalies. He noted that the grating theory of the time was unable to explain why, with light incident on a metal grating, a sharp peak can be seen in the diffraction at a certain angle. It was five years later that Lord Rayleigh proposed a suitable explanation [19]; this anomaly often called a Rayleigh anomaly now, or simply the diffraction edge. He explained that most of the singularities observed by Wood

occurred when a diffracted order was mapped to a grazing angle. He went on to put forth a theory that explained the majority of the anomalies put forth by Wood, but not quite all of them. Some of the anomalies that Wood observed only seemed to occur with TM polarized light. This type of anomaly was not categorized until Fano in 1941 [20] and fully explained until Hessel and Oliner in 1965 [21]; these polarization dependent anomalies turned out to be surface plasmon polaritons. Guided wave devices can be put into three main categories: surface plasmon polaritons (SPPs) and surface waves, guided waves, and leaky modes. SPP and surface wave structures were investigated by a number of people beginning in the 1950's[22; 23; 24; 25; 26; 27; 28; 29]. Guided wave devices have been studied at length by Magnusson *et al.* [30; 31; 32] and Morris *et al.* [33; 34]. Leaky mode devices have been studied by Bieber & Brown[35; 36], Fabrizio *et al.* [37], and others.

A guided mode resonance is created when an externally propagating wave is coupled to a leaky waveguide mode. This happens when the external wave is phase matched to a waveguide mode supported by the structure [31]. In order to achieve the phase matching conditions, a grating is typically used, either a planar interface with periodic refractive index changes or a corrugated surface. The resonance is essentially created by the interference of light that is specularly reflected from the surface with light that has been coupled into and out of the waveguide. Phase matching between the external wave and the waveguide mode is governed by applying the Bragg condition to the waveguide structure [38].

$$n_c k_0 \sin \theta_B + m \frac{2\pi}{\Lambda} = \beta, \quad (1.12)$$

where  $n_c$  denotes the refractive index of the cover,  $k_0 = \frac{2\pi}{\lambda_0}$  is the magnitude of the wavevector ( $\lambda_0$  is the vacuum wavelength),  $m$  is an integer denoting the order of diffraction,  $\Lambda$  is the grating period,  $\theta$  is the angle with respect to the surface



(a) Schematic of an all-dielectric guided mode resonance filter. (b) Transverse electric spectral response of the all-dielectric guided mode resonance filter calculated with rigorous coupled wave analysis.

Figure 1.2: Guided mode resonance filter reported by Magnusson and Wang where  $n_{cover} = 1$ ,  $n_{1h} = 2.42$ ,  $n_{1l} = 2.28$ ,  $n_2 = 1.38$ ,  $n_{substrate} = 1.52$ ,  $d_1 = 404$  nm,  $d_2 = 688$  nm and  $\Lambda = 1$   $\mu$ m for normal incidence.

normal, and  $\beta = \frac{2\pi}{\lambda_0} n_{eff}$  is the wavevector of the guided mode ( $n_{eff}$  is the effective index of the waveguide mode).

One of the main purposes of studying these resonances was to try and use them as narrowband pass filters. The all-dielectric structures investigated by Magnusson *et. al.* typically have a low baseline reflectance and a reflectance that approaches unity at resonance, as seen in figure 1.2(b). Likewise, the structure has a very high baseline transmission which falls almost to zero at resonance. In this example, the grating layer itself is acting as the waveguide. While there was much work done on the theory of guided mode resonance filters throughout the 1990s, there was not much experimental work done. In 2000, Boye and Kostuk published a paper investigating the effects of the finite size of a guided mode resonance filter where they fabricated devices of varying length [39]. A previous student under the tutelage of Prof. Brown, Jason Neiser, designed and fabricated guided mode

resonance structures that had resonances at different wavelengths for his Ph. D. thesis, an example of which is shown in figure 1.3 [40].

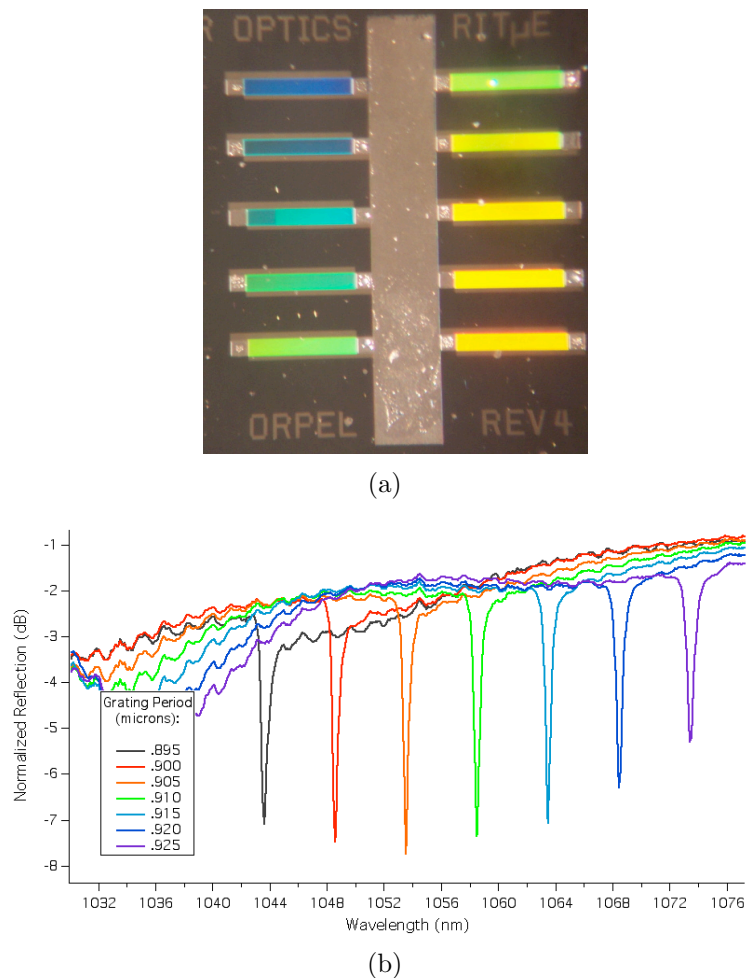


Figure 1.3: Top: Neiser Optically Resonant Periodic Electrode (ORPEL) GMR structures viewed in visible light. Bottom: Reflectance spectra from gratings of varying period.

While there are a handful of paper that have experimental results on the reflectance or transmittance of guided mode resonance filters, to the best of our knowledge there has been no published results on the phase properties through resonance. The latter half of this thesis will be devoted to investigating both the spectral and angular phase characteristics of guided mode resonators. As it stands today, guided mode resonators are used in a variety of different applications, and

one of the primary ones is to use it as a chemical or biological sensors. The reason for this is that a guided mode resonance is quite sensitive if there is a change in the refractive index of its environment. Thus if they coat the surface of resonator with some chemical or biological receptor, the local refractive index will change if some chemical or pathogen binds to it, thus changing the reflectance or transmittance. We will show that the phase of light reflected or transmitted is potentially more sensitive to these changes, and could result in a more sensitive detector.

## 1.4 Surface Plasmon Polaritons

In 1952 Pines and Bohm were trying to explain the energy loss of fast electrons passing through metal foils. They proposed that it was caused by a quantized bulk plasma oscillation of electrons in the metal, which they termed a “plasmon.” Plasmons can be separated into two main categories, and they depend primarily on geometry. These are bulk or volume plasmons, and surface plasmons. Surface plasmons, which will be the focus of most of chapter 5, were originally investigated by Ritchie in 1957 [22]. According to Maxwell’s equations, a surface plasmon can exist at an interface of two materials when the real part of their dielectric function changes sign [41]. A surface plasmon polariton is essentially a light wave that has been trapped on the surface of a conductor because of its interactions with its free electrons. The free electrons on the conductor’s surface will oscillate coherently with the electric field of the light wave, and it is the resonant interaction between the two that give the SPP its properties [42].

## 1.5 Nanofabrication

### 1.5.1 Parallel vs. Series methods

The various methods used for nanostructure fabrication can be divided into two main categories, parallel and series methods. A parallel method either replicates a simple feature or prints an entire complex pattern at the same time. The most common parallel fabrication method is photolithography. Photolithography uses a mask that contains the pattern information that is imaged onto a sample. The sample needs to be coated in a photosensitive material that is developed in a chemical bath after exposure to create the pattern in relief. Typically this imaging of the mask is done with a  $4\times$  or  $10\times$  reduction in scale. This reduction makes the mask easier to fabricate since the features on it need not be as small as the final printed pattern.

There are two primary benefits to photolithography. The first, which is fundamental to all parallel processes, is that it is able to produce many of the same pattern at once. This makes the process much faster than a serial process, which needs to draw out a pattern one line at a time. Speed of manufacturing translates to a higher output, which in turn results in more money for the manufacturer. The second major benefit to photolithography is that the process is non-destructive to the mask. As masks are expensive to make, damaging them is bad for business. Processes such as nanoimprint lithography are parallel, but the mask is often damaged. Nanoimprint lithography uses a master die. This die is then pressed into a polymer layer on the sample and the pattern is transferred physically. A quick etch is typically done after imprinting to ensure that the substrate is exposed in the troughs of the pattern. One of the drawbacks of this process is the master die can be damaged in the process of extracting it from the sample.

Serial processes tend to be much slower, since they draw a pattern out on a

substrate as one might draw a picture using a pencil; this tends to make the process expensive for fabricating large numbers of devices. However, serial processes have the benefit of being much cheaper for small number of samples because of the large tooling cost associated with photo- or nanoimprint lithography. As a result, serial processes are mostly used for prototyping. All of the samples fabricated in this thesis were done using two serial processes: electron beam lithography and direct ion writing.

Electron beam lithography uses a focused beam of electrons that is deterministically moved across a sample that has been coated with an electron sensitive resist. Commonly this is done using a scanning electron microscope (SEM). Electron beam lithography This pattern is then developed and can either be used as a mask for deposition, or it can be transferred to the substrates via an etch process. Samples fabricated for chapters 4-6 used this method.

For direct ion writing, a focused beam of ions is moved across the sample much like that used in electron beam lithography. The difference is that an ion has much more energy than an electron, and is able to ablate off material of the substrate; this allows three dimensional relief patterns to be directly written into the substrate.

This process, can also be used for extremely low ion doses, where there is minimal ion milling, with a significant fraction of ions implanted into the substrate. This allows the creation of patterns in two dimensions simply by varying the ion implantation dose. Changing the ion implantation dose will change the refractive index in the implanted region, and can also produce chemical changes that under some circumstances result in etch resistance.

## 1.5.2 Fabrication Platform

### Silicon

Silicon has been the material of choice for the microelectronics industry since its inception. Over the past century, the silicon wafer manufacturing process has been greatly refined, and for this reason, silicon wafers can be made with better quality and lower price than any other semiconductor. This fact makes silicon very attractive for photonics, and motivates a drive to integrate microelectronics and photonics. Any photonic system requires a light source (laser or LED), light control (waveguides & modulators) and detectors. Both modulators and detectors have been demonstrated in the near and sub band gap wavelength range. However, light emission remains a major challenge due to the indirect bandgap.

### Silicon-on-Insulator (SOI)

The silicon-on-insulator geometry consists of a typically thin layer of single crystal silicon isolated from a substrate by an insulating layer. One of the first techniques in producing such a platform was the method of epitaxial deposition of silicon on a crystalline sapphire wafer; this was first done by Manasevit and Simpson in 1964 [43]. Although the lattice match between sapphire and silicon was close enough for the sapphire to act as a seed crystal for the silicon, the lattice constants are not a perfect match. As a result, the single crystal silicon films tended to have numerous defects in the crystal lattice, which typically caused a fair amount of loss. In 1985, Celler, Hemment, West, and Gibson published a new technique of making SOI wafers. They used a large dose oxygen implantation followed by a lamp annealing process at 1405 °C, which is close to the melting point of silicon [44]. This high annealing temperature solved the problem of earlier work that had issues with an oxygen rich defective layer between the insulating region and the surface [45; 46]. This process is now called the SIMOX process (Separation by IMplanted

OXygen); the other primary method of producing SOI is the BESOI (Bond and Etch Back SOI) method. The process of bonding two silicon wafers, one with a thermally grown oxide, to create SOI was started by Lasky in 1986 [47]. Haisma, Spierings, Biermann and Pals published a paper covering a few different methods of thinning the top (device) layer of bonded SOI wafers in 1989 [48].

SOI wafers are useful for a variety of different systems. Their first commercial use was in 1998, when IBM started using SOI wafers for their chip fabrication process in their PowerPC microprocessor and S/390, AS/400, and RS/6000 line of servers [49]. For this thesis, SOI wafers are used primarily for their inherent ability to act as infrared waveguides. The light will be guided in the silicon device layer since its refractive index is much higher than the surrounding oxide and air, as mentioned in section 1.2.

## 1.6 Nanostructure Modeling

Throughout this thesis, we will use a variety of different modeling methods. The primary method used was rigorous coupled wave analysis (RCWA), but a variety of simpler models were used, including slab model for waveguides, thin film code, and fitting to parameterized functions such as those used to describe Fano resonances. In order to accurately model the both that amplitude and phase response of TE and TM light for a nanostructure to get the polarimetric response since both are necessary to describe the interaction.

### 1.6.1 Basic Slab Model for Waveguides

Often when looking at a multi-layer structure that contains a waveguide, the energy is confined extremely well in the wave-guiding layer. If this is the case where the evanescent waveguide fields are sufficiently small by the time they propagate

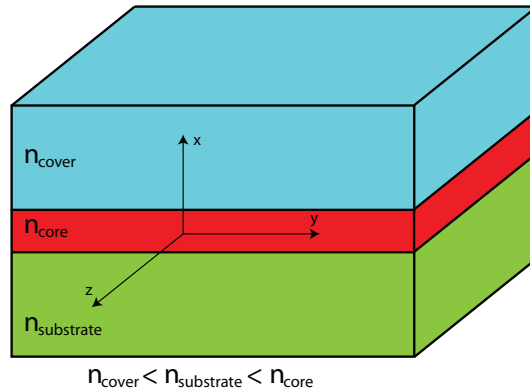


Figure 1.4: Diagram of the slab model waveguide.

beyond the cladding layer, a basic slab model will work well. A slab model is useful for estimating the waveguide propagation constant ( $\beta$ ), the number of modes ( $m_{max}$ ), and the field profile. The following paragraphs follow the treatments of Kogelnik [50] and Agrawal [51].

We define the time dependent electric and magnetic fields as

$$\tilde{\mathbf{E}}(t) = \mathbf{E}e^{-i\omega t} \quad \text{and} \quad \tilde{\mathbf{H}}(t) = \mathbf{H}e^{-i\omega t}, \quad (1.13)$$

where  $\tilde{\mathbf{E}}(t)$  and  $\tilde{\mathbf{H}}(t)$  are the time-dependent vectors of the electric and magnetic field,  $\mathbf{E}$  and  $\mathbf{H}$  are the complex amplitudes and  $\omega$  is the angular frequency. If we take the first two Maxwell's equations 1.1 and 1.2, and the constitutive equations,

$$\mathbf{D} = \varepsilon\mathbf{E}, \quad (1.14)$$

$$\mathbf{B} = \mu\mathbf{H}, \quad (1.15)$$

we can get the following form of Maxwell's equations,

$$\nabla \times \mathbf{E} = i\omega\mu\mathbf{H}, \quad (1.16)$$

$$\nabla \times \mathbf{H} = -i\omega\varepsilon\mathbf{E}, \quad (1.17)$$

where  $\varepsilon = \varepsilon_0\varepsilon_r = \varepsilon_0n^2$  is electric permittivity,  $n$  is the refractive index of a medium, and  $\mu = \mu_0\mu_r$  is the magnetic permeability. For this derivation, and for most natural materials, the relative magnetic permeability,  $\mu_r$ , is essentially equal to one. If we assume a planar geometry with the  $x$ -axis normal to the waveguide, and light propagating along the  $z$ -axis, we can impart the following condition on the partial derivatives of equations 1.16 and 1.17,

$$\frac{\partial \mathbf{E}}{\partial y} = 0, \quad \frac{\partial \mathbf{H}}{\partial y} = 0, \quad \frac{\partial \mathbf{E}}{\partial z} = i\beta\mathbf{E}, \quad \frac{\partial \mathbf{H}}{\partial z} = i\beta\mathbf{H}. \quad (1.18)$$

These six equations allow us to solve for the two linearly independent solutions of transverse electric (TE,  $E_z = 0$ ) and transverse magnetic (TM,  $H_z = 0$ ) polarization. For TE modes,  $E_y$  satisfies

$$\frac{d^2 E_y}{dx^2} + (n^2 k_0^2 - \beta^2) E_y = 0, \quad (1.19)$$

where  $k_0 = \omega\sqrt{\varepsilon_0\mu_0} = \frac{\omega}{c}$ , with the magnetic components:

$$H_x = \frac{\beta}{\omega\varepsilon_0} E_y, \quad H_y = 0, \quad H_z = -\frac{i}{\omega\mu_0} \frac{dE_y}{dx}. \quad (1.20)$$

Likewise, for TM modes  $H_y$  will satisfy

$$\frac{d^2 H_y}{dx^2} + (n^2 k_0^2 - \beta^2) H_y = 0, \quad (1.21)$$

with electric field components of

$$E_x = \frac{\beta}{\omega\varepsilon_0 n^2} H_y, \quad E_y = 0, \quad E_z = -\frac{i}{\omega\mu_0 n^2} \frac{dH_y}{dx}. \quad (1.22)$$

If we look first at the TE case, equation 1.19 can be solved in each layer of the

waveguide. The general solution can be written as:

$$E_y(x) = \begin{cases} B_c \exp[-q_1(x-d)]; & x > d, \\ A \cos(px - \phi) & ; \quad |x| \leq d, \\ B_s \exp[q_2(x+d)] & ; \quad x < -d, \end{cases} \quad (1.23)$$

where we have discarded the exponentially growing terms in the cover and substrate since we know that the energy is confined in the waveguide core. The constants  $p$ ,  $q_1$  and  $q_2$  are defined as:

$$p^2 = n_1^2 k_0^2 - \beta^2, \quad q_1^2 = \beta^2 - n_c^2 k_0^2, \quad q_2^2 = \beta^2 - n_s^2 k_0^2, \quad (1.24)$$

where  $n_c$  is the refractive index of the cover layer,  $n_1$  is the index of the core, and  $n_s$  is the index of the substrate.

The constants in equation 1.23  $B_c, B_s, A$ , and  $\phi$  can be determined via the boundary conditions at the two planar interfaces by requiring the tangential components of both  $\mathbf{E}$  and  $\mathbf{H}$  to be continuous. Continuing with the TE case, this is satisfied if  $E_y$  and  $H_z$  are continuous at  $x = \pm d$ . Using equation 1.23 we can see that  $E_y$  is continuous if

$$B_c = A \cos(pd - \phi); \quad B_s = A \cos(pd + \phi). \quad (1.25)$$

To ensure that  $H_z$  is continuous, we look at equation 1.20 and see that  $H_z$  is related to the derivative  $\frac{dE_y}{dx}$ . If we constrain the derivative to be continuous at  $x = \pm d$ ,  $H_z$  will be continuous. Applying this constraint, we obtain the series of equations relating  $A$  and  $\phi$

$$pA \sin(pd - \phi) = q_1 A \cos(pd - \phi) \quad (1.26)$$

$$pA \sin(pd + \phi) = q_2 A \cos(pd + \phi) \quad (1.27)$$

Simplifying equations 1.26 and 1.27 we obtain

$$\tan(pd - \phi) = \frac{q_1}{p}, \quad \tan(pd + \phi) = \frac{q_2}{p}. \quad (1.28)$$

Solving for  $\phi$ , we get:

$$2\phi = m\pi - \tan^{-1}\left(\frac{q_1}{p}\right) + \tan^{-1}\left(\frac{q_2}{p}\right) \quad (1.29)$$

We can also solve the equations in 1.28 in such a way to eliminated  $\phi$ . Doing so gives us what is known as the *eigenvalue equation* for TE<sub>m</sub> modes,

$$2pd = m\pi + \tan^{-1}\left(\frac{q_1}{p}\right) + \tan^{-1}\left(\frac{q_2}{p}\right). \quad (1.30)$$

By doing the same process but starting with equations 1.21 and 1.22, the eigenvalue equation for TM<sub>m</sub> modes can be obtained:

$$2pd = m\pi + \tan^{-1}\left(\frac{n_1^2 q_1}{n_c^2 p}\right) + \tan^{-1}\left(\frac{n_1^2 q_2}{n_s^2 p}\right). \quad (1.31)$$

We can use the eigenvalue equations to solve for the effective index,  $\bar{n}$ , of a waveguide mode. To do so, it is helpful to define two new quantities,

$$b = \frac{\bar{n}^2 - n_s^2}{n_1^2 - n_s^2}, \quad \delta = \frac{n_s^2 - n_c^2}{n_1^2 - n_s^2} \quad (1.32)$$

where  $b$  is a normalized propagation constant defined in the range  $0 < b < 1$ , and  $\delta$  is a measure of the how asymmetric the waveguide is. Using these new parameters, we can rewrite the TE and TM eigenvalue equations 1.30 and 1.31 to get

$$2V\sqrt{1-b} = m\pi + \tan^{-1}\sqrt{\frac{b}{1-b}} + \tan^{-1}\sqrt{\frac{b+\delta}{1-b}}, \quad (1.33)$$

$$2V\sqrt{1-b} = m\pi + \tan^{-1}\left(\frac{n_1^2}{n_s^2}\sqrt{\frac{b}{1-b}}\right) + \tan^{-1}\left(\frac{n_1^2}{n_c^2}\sqrt{\frac{b+\delta}{1-b}}\right), \quad (1.34)$$

respectively, where  $V = k_0d\sqrt{n_1^2 - n_s^2}$ . For most of the structures modeled in this thesis, the general model can be simplified even more to the symmetric slab model. In this case, the substrate and the cover layer are the same material, thus setting  $\delta = 0$ .

To determine the maximum number of propagating orders, we can find the cutoff frequency by setting  $b = 0$  in equations 1.33 and 1.34 getting,

$$2V_m = m\pi + \tan^{-1}\sqrt{\delta}, \quad (1.35)$$

$$2V_m = m\pi + \tan^{-1}\left(\frac{n_1^2}{n_c^2}\sqrt{\delta}\right), \quad (1.36)$$

respectively. For the symmetric slab case,  $n_c = n_s$  which makes  $\delta = 0$ . Plugging that into equations 1.35 and 1.36 allows us to see that there will be an equal number of TE and TM modes that can propagate in the symmetric case:

$$V_m = \frac{m\pi}{2}. \quad (1.37)$$

Solving for  $m$ , and plugging in the definition of  $V$  we get the total number of propagating modes for each polarization,

$$m = \frac{4d}{\lambda}\sqrt{n_1^2 - n_s^2}. \quad (1.38)$$

Using equation 1.38, for a silicon waveguide with thickness  $1\ \mu\text{m}$  thickness with silica substrate and cover layers, we get  $m = 6.1$ , rounding up we get 7 TE and TM modes for a total of 14 supported waveguide modes.

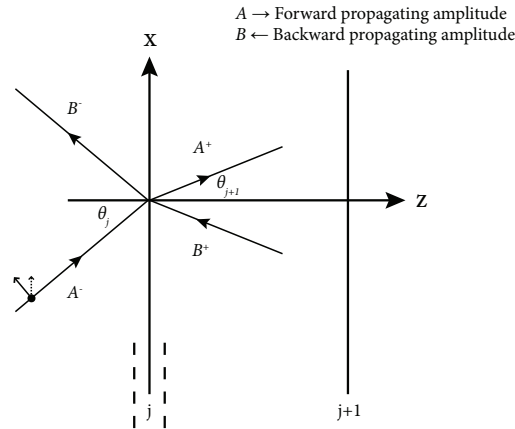


Figure 1.5: Diagram of the propagating waves used for the thin film model.

## 1.6.2 Thin Film Stack Modeling

Structures that are composed of many layers are sometimes modeled better with a thin film stack model as opposed to a waveguide model. Many times when designing a guided mode structure, it is beneficial to use the slab model to determine what fundamental modes of the waveguide supports, then switch to a thin film model to plot the electric field profile as a function of position in the structure. This can be used to optimize the layers around the waveguide to get an optimal coupling condition. The thin film modeling done for this thesis was implemented in MATLAB. The method that we used involved using forward and backward propagating waves, and matching boundary conditions at each interface.

Figure 1.5 shows the  $j^{\text{th}}$  and  $j + 1^{\text{st}}$  interface in a film stack, with  $A$  representing the amplitude of forward propagating waves ( $e^{ikz}$ ), and  $B$  representing the amplitude of the backwards propagating waves ( $e^{-ikz}$ ). We use the  $+$  ( $-$ ) superscripts to denote fields on the right (left) side of the interface. In region 1,

$$A(z) = A^- e^{ik_j z}, \text{ and} \quad (1.39)$$

$$B(z) = B^- e^{-ik_j z}. \quad (1.40)$$

In region 2,

$$A(z) = A^+ e^{ik_{j+1}z}, \text{ and} \quad (1.41)$$

$$B(z) = B^+ e^{-ik_{j+1}z}, \quad (1.42)$$

where  $k_j = n_j k_0 \cos \theta_j$  is the  $z$  component of the wave vector in layer  $j$ . To solve for the multilayer transmission and reflection coefficients, we start by applying boundary conditions at the  $j^{\text{th}}$  interface by requiring  $E_y$  and  $H_y \propto \frac{\partial E_y}{\partial z}$  to be continuous. These constraints yield the following relations,

$$A^- + B^- = A^+ + B^+ \quad (1.43)$$

$$k_j A^- - k_j B^- = k_{j+1} A^+ - k_{j+1} B^+. \quad (1.44)$$

Adding these together we can obtain  $A^-$ ,

$$2A^- = \left(1 + \frac{k_{j+1}}{k_j}\right) A^+ + \left(1 - \frac{k_{j+1}}{k_j}\right) B^+, \quad (1.45)$$

and subtracting, we get  $B^-$

$$2B^- = \left(1 - \frac{k_{j+1}}{k_j}\right) A^+ + \left(1 + \frac{k_{j+1}}{k_j}\right) B^+. \quad (1.46)$$

This allows us to put it in matrix form as,

$$\begin{bmatrix} A^+ \\ B^+ \end{bmatrix} = \frac{1}{2} \begin{bmatrix} 1 + \frac{k_{j+1}}{k_j} & 1 - \frac{k_{j+1}}{k_j} \\ 1 - \frac{k_{j+1}}{k_j} & 1 + \frac{k_{j+1}}{k_j} \end{bmatrix} \begin{bmatrix} A^- \\ B^- \end{bmatrix}, \quad (1.47)$$

This matrix shows what happens to the TE electric field amplitudes as the light passes through the  $j^{\text{th}}$  interface of the multi-layer.

A similar process is used to obtain the TM electric field amplitudes. We define the forward and backward propagating waves the same as in equations 1.39-1.42, but change our boundary conditions. This time we require that  $E_x$  be continuous, and that  $\epsilon_j \mathbf{E}_z^- = \epsilon_{j+1} \mathbf{E}_z^+$ , which we can rewrite as:

$$\epsilon_j |\mathbf{E}| \sin \theta_j = \epsilon_{j+1} |\mathbf{E}| \sin \theta_{j+1}. \quad (1.48)$$

Now substituting in  $|\mathbf{E}| = \frac{E_x}{\cos \theta}$ , we get:

$$\frac{\epsilon_j \mathbf{E}_x \sin \theta_j}{\cos \theta_j} = \frac{\epsilon_{j+1} \mathbf{E}_x \sin \theta_{j+1}}{\cos \theta_{j+1}} \quad (1.49)$$

Thus our two TM boundary condition constraints become,

$$A^- + B^- = A^+ + B^+, \quad (1.50)$$

$$\frac{\epsilon_j \sin \theta_j}{\cos \theta_j} (A^- - B^-) = \frac{\epsilon_{j+1} \sin \theta_{j+1}}{\cos \theta_{j+1}} (A^+ - B^+), \quad (1.51)$$

where  $A$  and  $B$  are now the coefficients on  $E_x$  instead of  $E_y$  as was the case in the TE derivation. By definition,  $\epsilon_j = n_j^2$ , and if we apply Snell's Law,  $n_j \sin \theta_j = n_{j+1} \sin \theta_{j+1}$ , we can simplify to:

$$\frac{n_j}{\cos \theta_j} (A^- - B^-) = \frac{n_{j+1}}{\cos \theta_{j+1}} (A^+ - B^+). \quad (1.52)$$

We can now generalize equation 1.47 by defining a new parameter  $\gamma$ ,

$$\underline{\underline{R}}_j = \frac{1}{2} \begin{bmatrix} 1 + \gamma_j & 1 - \gamma_j \\ 1 - \gamma_j & 1 + \gamma_j \end{bmatrix} \quad \text{where} \quad \gamma_j = \begin{cases} \frac{n_{j+1} \cos \theta_{j+1}}{n_j \cos \theta_j} & \text{TE} \\ \frac{n_{j+1} / \cos \theta_{j+1}}{n_j / \cos \theta_j} & \text{TM} \end{cases}. \quad (1.53)$$

To handle the propagation from the  $j^{\text{th}}$  to the  $j + 1^{\text{st}}$  interface, we multiply by the transfer matrix,

$$\underline{\underline{T}}_j = \begin{bmatrix} e^{-ik_{j+1}t_{j+1}} & 0 \\ 0 & e^{ik_{j+1}t_{j+1}} \end{bmatrix}. \quad (1.54)$$

Now we can handle multiple layers and propagation between layers just by mul-

tipling the necessary matrices together,

$$\underline{\underline{M}} = \begin{bmatrix} M_{11} & M_{12} \\ M_{21} & M_{22} \end{bmatrix} = \underline{\underline{R}}_1 \underline{\underline{T}}_1 \underline{\underline{R}}_2 \underline{\underline{T}}_2 \cdots \underline{\underline{R}}_j \underline{\underline{T}}_j \underline{\underline{R}}_{j+1}. \quad (1.55)$$

the Fresnel coefficients for reflection ( $r$ ) and transmission ( $t$ ) can then be calculated as,

$$r_{\text{TM}}^{\text{TE}} = \mp \frac{M_{21}}{M_{22}} \quad t = M_{11} + \frac{M_{12}M_{21}}{M_{22}}. \quad (1.56)$$

To calculate the reflected or transmitted *energy*, we can calculate the reflectivity ( $\mathcal{R}$ ) and transmissivity ( $\mathcal{T}$ ) as

$$\mathcal{R} = |r|^2 \quad \text{and} \quad \mathcal{T} = \frac{n_t \cos \theta_t}{n_i \cos \theta_i} |t|^2. \quad (1.57)$$

### 1.6.3 Rigorous Coupled Wave Analysis

The primary method of modeling structures for this thesis was rigorous coupled wave analysis (RCWA). RCWA is a method introduced by Moharam and Gaylord in 1981[52], for the purpose of modeling planar gratings, however they continued to evolve their theory over the next decade [53; 54; 55]. By 1986 they were able to simulate metallic surface relief gratings [56]. The bulk of the RCWA approach has not changed much since then; there have been some alterations for computational speed and stability however. The basic approach in RCWA is to treat the permittivity changes in the grating as a Fourier expansion. Writing the coupled-wave equations in matrix form allows for a solution to be determined with its eigenvalues and necessary boundary conditions [57]. In 1996 Lalanne and Morris implemented a method for fast, more stable TM convergence [58]. RCWA has been extended to 2-D geometries and is a common tool for modeling electromagnetic interactions in semiconductor reticles. Our RCWA software is implemented on a Matlab platform and includes code contributed by Song Peng,

Jason Neiser, Robert Fabrizio and Thomas Brown.

## 1.7 Thesis Chapter Breakdown

### **Chapter 2 - Optical Properties of Gallium Implanted Silicon**

In chapter 2, we cover a fairly new optical material, gallium implanted silicon (Si:Ga). Si:Ga is of interest due to its ease of deterministic implantation, and interesting optical properties.

### **Chapter 3 - Fabrication, Measurement, and Analysis of Gallium Implanted Silicon Nanostructures**

In chapter 3, we cover how to use Si:Ga to make nanowire arrays. The polarimetric properties of these nanostructures are measured and compared with the RCWA theory.

### **Chapter 4 - Spectral Phase Effects in Guided Mode Resonances**

The second half of my thesis covers phase effects in different guided mode resonances. Chapter 4 covers *spectral* phase for guided mode resonances fabricated on a SOI platform.

### **Chapter 5 - Angular Phase Effects in Guided Mode Resonances**

Chapter 5 covers the theory and experiment of *angular* phase effects of a guided mode in a surface plasmon geometry. It also includes a theoretical look the angular

phase effects of the SOI guided mode structure used in chapter 4.

## **Chapter 6 - The Parametric Plot: A New Way of Looking at Guided Mode Resonances**

Lastly, chapter 6 looks at a new way to visualize a guided mode resonance in a parametric plot of the complex Fresnel coefficients. It also covers ideal and generalized Fano resonances. We present a fit to a generalized Fano resonance using data presented in chapter 4.

## Chapter 2

# Optical Properties of Gallium Implanted Silicon

### 2.1 Introduction

Nanostructures are ubiquitous in nature and technology. A variety of scientific fields use devices that contain nanostructured materials beyond the obvious nanotechnology such as computer processors. Their applications include spectroscopy, biological and chemical sensors, and photonic devices. The means of fabricating nanostructures are almost as numerous as the applications that use them. One method that is used heavily in the first half of this thesis is focused ion beam (FIB) writing. FIB uses a focused beam of ions to ablate, or sputter off parts of a sample; it is a direct write method, which makes it a serial fabrication process. One of the primary ion sources for FIB machines is gallium. A standard means of gallium emission is to use a liquid metal ion source, which is covered in great detail by Orloff, Utlaut and Swanson [59]. In a FIB, the gallium ions are accelerated with an electric potential toward the sample, and focused through a series of electro-magnetic lenses. The beam will ablate or sputter off atoms from the surface of the sample at a rate that depends on the intensity of the beam. This

intensity is typically controlled via adjusting the size of an aperture in the lens column, but can also be adjusted with the size of the focal spot, which is adjusted with the electro-magnetic lenses in the ion column. As the ions hit the surface and sputter off the substrate, some of the ions will penetrate into the substrate. This results in a layer of ion doping that can be spatially controlled by scanning the beam around. If the beam is focused to a spot, it can be traced around the sample to dope ions into the substrate in a specific pattern. The depth of the ion implantation is determined by the mass of the incident ion, electric potential applied for ion acceleration, and the mass and arrangement of the atoms that make up the substrate. There are levels of ion dose (#of ions/area) that will sputter a negligible amount of the surface, but dope the substrate with enough ions to alter its optical characteristics.

The system that will be explored in this thesis is that of using gallium ions to deterministically dope silicon. Results shown in this thesis have been done using  $\langle 100 \rangle$  silicon wafers. Calculating the depth of ion implantation for a crystal is often more difficult than for an amorphous material, due to the ion channelling properties of crystals. That means that the depth of ion implantation in a crystal will depend on the orientation of the crystal with respect to the ion implantation [60]. The first order reason for this is fairly obvious when viewing a model of the crystallographic structure. The three dimensional periodic structure can be rotated to specific angles such that a lot of free space can be seen; ion implantation at these angle will cause ions to tunnel farther. For angles where a lot of atoms are seen in the cross section, the ion implantation range will be much shallower. For this chapter we will be treating our silicon as amorphous, due to the fact that the high energy gallium ions destroy the silicon crystal lattice at extremely small doses, as will be seen later in the chapter.

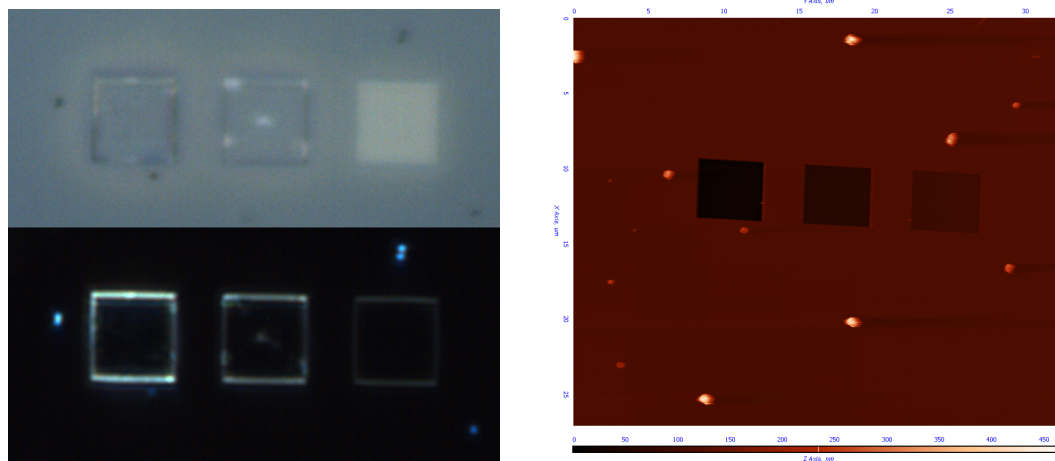
## 2.2 Implantation - Sample Fabrication

Sample fabrication was done with the URnano Zeiss Auriga crossbeam SEM/FIB system that is controlled via the NanoPatterning Visualization Engine (NPVE) created by Fibics Incorporated. Starting with a polished  $\langle 100 \rangle$  silicon wafer, a series of uniformly doped pads were implanted into the surface with the gallium ion beam. The FIB emitter was set to an accelerating voltage of 30kV (standard operating voltage), and an aperture was used to limit the specimen current to 1nA.

Two separate samples were fabricated: the first was implanted with three uniformly doped square pads of 0.1, 0.2 and 0.3 nC/ $\mu\text{m}^2$ . A bright field light microscope image of this sample can be seen in figure 2.1(a). The second pattern was written with a specimen current of 20nA. The pattern was chosen to be an array of  $250\mu\text{m} \times 420\mu\text{m}$  rectangles to compromise between writing time and size of pattern necessary for accurate measurement of optical properties in the setup detailed in section 2.4. This sample was fabricated with five rectangular patterns with doses that varied from 0.01 - 0.9nC/ $\mu\text{m}^2$ , and can be seen if figure 2.2(a).

The FIB writes a pattern by dwelling at points in a Cartesian grid. Four parameters are required to tell the beam how to write any given pattern. To write a given dose, one can constrain two of the following parameters and the third will be determined: dwell time, dwell point spacing, and the number of passes the beam rasters over the pattern.

One note of caution to future users of the NPVE system: The software treats the number of passes as a normal continuous variable. For example, a choice of a dose, dwell time, and dwell point spacing that yields a number of passes of 1.5 will direct the system to raster your pattern once and stop halfway through the second time. This results in a pattern that has the correct *average* dose but with different doses on the top and bottom.



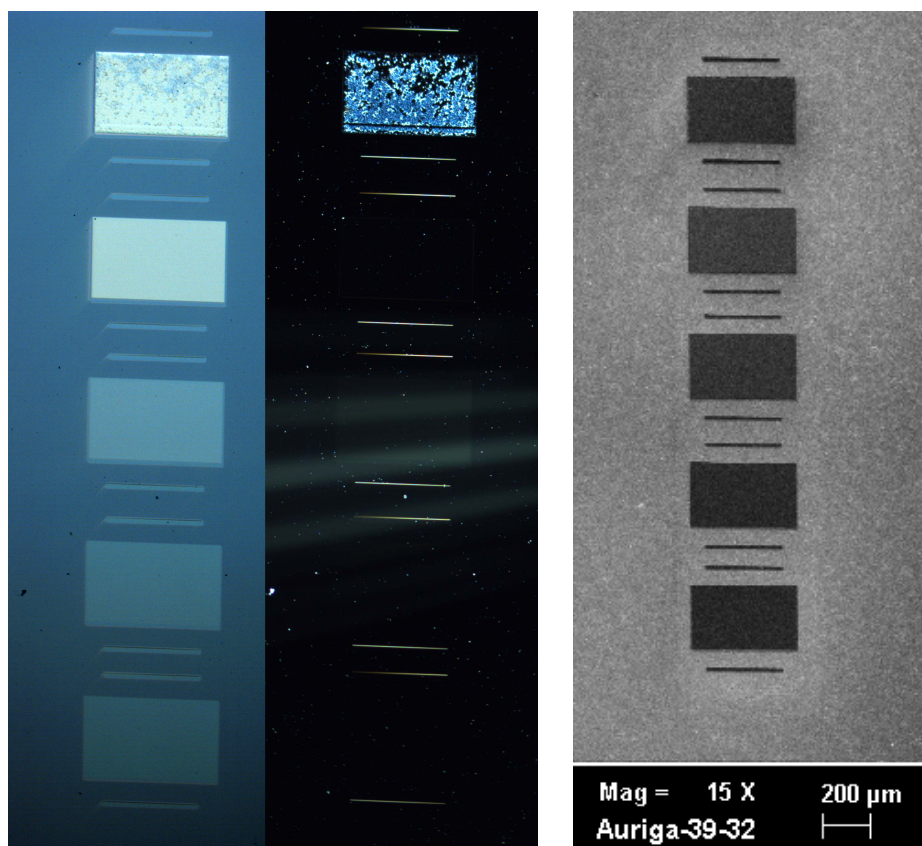
(a) Top: Bright field Bottom: Dark field light microscope images of sample 1.

(b) AFM micrograph of sample 1.

Figure 2.1: Light microscope and AFM images of sample 1.

The ion beam shape at focus is Gaussian in nature; for this reason, we chose our dwell spacing to be 10% of the beam diameter. To avoid the issue noted above, we chose a reasonable dwell time ( $1 - 2 \mu s$ ) and let the software calculate the number of passes needed for the chosen parameters. We then released the dwell time constraint, rounded the previously calculated number of passes to nearest whole number, and let it calculate the necessary dwell time. To create a uniformly doped region, it is useful to design the write process to employ multiple passes of the beam. This is because, as the beam implants gallium ions, it does sputter some of the surface off.

The sputtered material must end up somewhere; a portion of it will end up depositing on the surface in close proximity to where its point of origination was. This means that when attempting an implantation in a single pass, the area where the implantation started will be covered by the sputtered material; this redeposition greatly reduces the uniformity of the surface. In contrast, increasing the number of passes will increase the uniformity.



(a) Left: Bright field Right: Dark field image of sample 2. Five  $250\mu\text{m} \times 420\mu\text{m}$  rectangles of dose 0.01, 0.03, 0.1, 0.3, and  $0.9 \text{ nC}/\mu\text{m}^2$ , increase from bottom to top.

(b) SEM micrograph of sample 2. Five  $250\mu\text{m} \times 420\mu\text{m}$  rectangles of dose 0.01, 0.03, 0.1, 0.3, and  $0.9 \text{ nC}/\mu\text{m}^2$ , increase from bottom to top.

Figure 2.2: Light microscope and SEM images of sample 2.

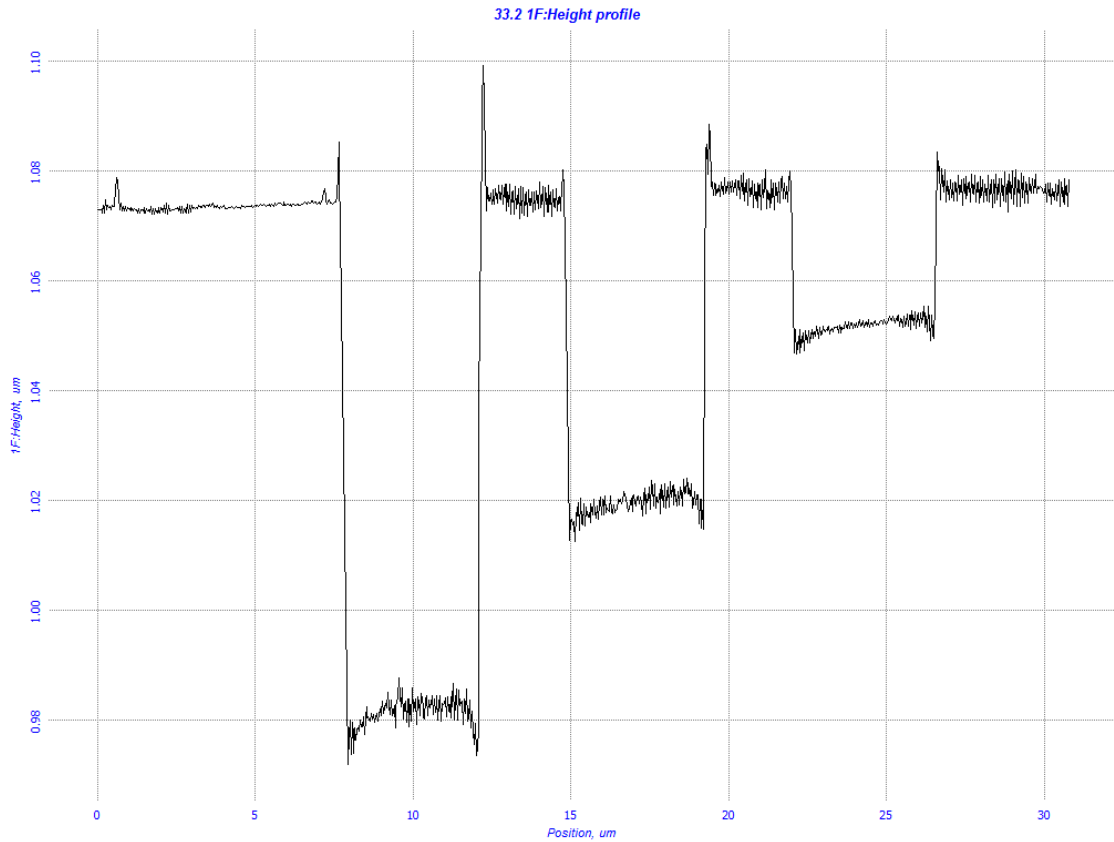


Figure 2.3: AFM slice through all three pads on sample 1 (figure 2.1(b)).

### 2.2.1 Determination of the Milling Rate at Standard Operating Parameters ( $30kV\text{Ga}^+$ )

The first sample (three  $100 \times 100 \mu\text{m}$  implanted squares) was used to determine the milling rate of the gallium ion beam vs dose. The sample was a bare silicon wafer that was implanted with three uniformly doped regions of 0.1, 0.2 and 0.3  $\text{nC}/\mu\text{m}^2$ , as seen in figure 2.1(a). Measurement of the milling depth was done with an NT-MDT Solver Next atomic force microscope (AFM); the results of a two dimensional scan across the three regions is shown in figure 2.1(b). A line scan through the center of all three pads is shown in figure 2.3.

As expected, the depth of milling increases with implantation dose. For a

dose of 0.1, 0.2 and 0.3  $\text{nC}/\mu\text{m}^2$ , the ion beam milled 35 nm, 58 nm, and 95 nm respectively.

## 2.3 Implantation Model - Ion Ranging Statistics

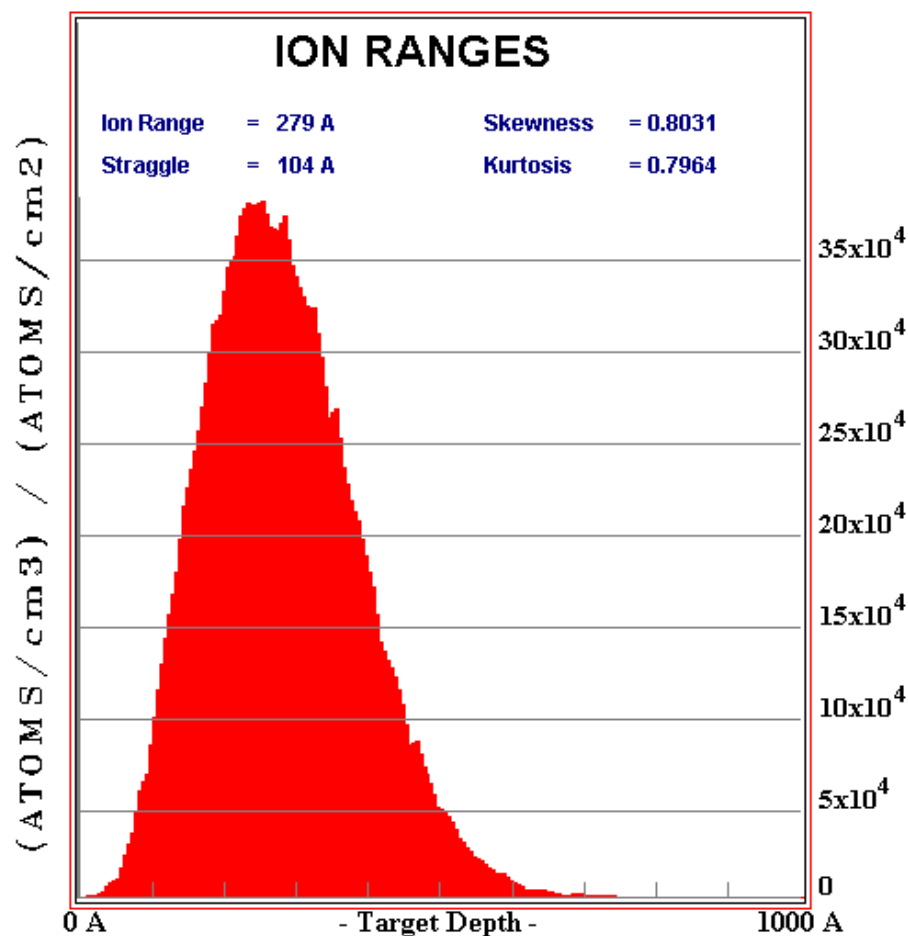


Figure 2.4: SRIM Monte Carlo simulation of 50,000  $\text{Ga}^+$  accelerated at 30kV implanted into silicon.

To better understand the gallium ion distribution in the silicon, we modeled the implantation process using ion range statistics. Ion range statistics are usually modeled using Monte-Carlo methods that sample the probability distribution and

numerically compute the trajectories of a large ensemble of ions. We used an open source program called: “SRIM - The Stopping and Range of Ions in Matter.” This program was created by J.F. Ziegler, and is based on the original paper of Biersack and Haggmark, ”A Monte Carlo computer program for the transport of energetic ions in amorphous targets.” Figure 2.4 shows a SRIM simulation of 50,000 gallium ions implanted in bare silicon that were accelerated with a  $30kV$  electric potential.

The gallium ion distribution has a slightly skewed distribution, with a maximum concentration occurring around 25 nm into the silicon substrate. It is important to note however, that this is the distribution of ions implanted into the substrate without sputtering taken into account. We know from practice that as ions are being implanted, the surface of the silicon is being sputtered off. As we saw in figure 2.3, we can expect at least 30 nm of milling to occur with a nominal dose of  $0.1nC/\mu m^2$ . This means that the final distribution of ions for any sample that has a reasonable dose will be more skewed toward the surface than we see in figure 2.4. Once an implantation has milled 25 nm into the surface, the

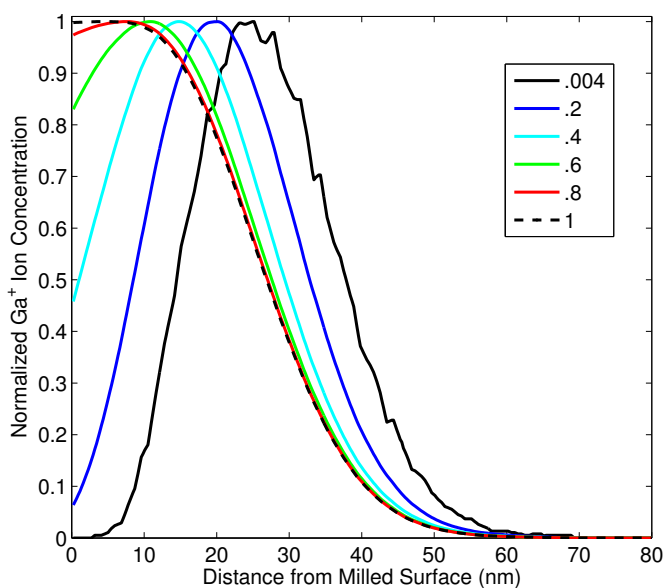


Figure 2.5: Simplistic normalized gallium profile (figure 2.4) taking milling into account. Dashed curve shows the equilibrium case.

ion concentration profile will stabilize to something closer to figure 2.5, where we show how the normalized implantation profile varies from very low doses (black = .4% of equilibrium dose) to the dose necessary to reach an equilibrium profile (red curve).

## 2.4 Si:Ga Ellipsometry - Experimental Results

To experimentally measure the optical properties of the gallium implanted silicon we employed a fairly simple ellipsometric setup. Standard FIB systems tend to have a small writing field, which makes it difficult to fabricate a sample large enough to accurately measure the optical constants using conventional ellipsometers. The Zeiss Auriga system used to fabricate the sample has a  $420 \times 420 \mu\text{m}$  maximum writing field size. For this measurement, we used the second sample mentioned in section 2.2, five gallium implanted pads of 0.01, 0.03, 0.1, 0.3, and  $0.9\text{nC}/\mu\text{m}^2$ , which were  $250 \times 420 \mu\text{m}$  as seen in figure 2.7. To measure the opti-

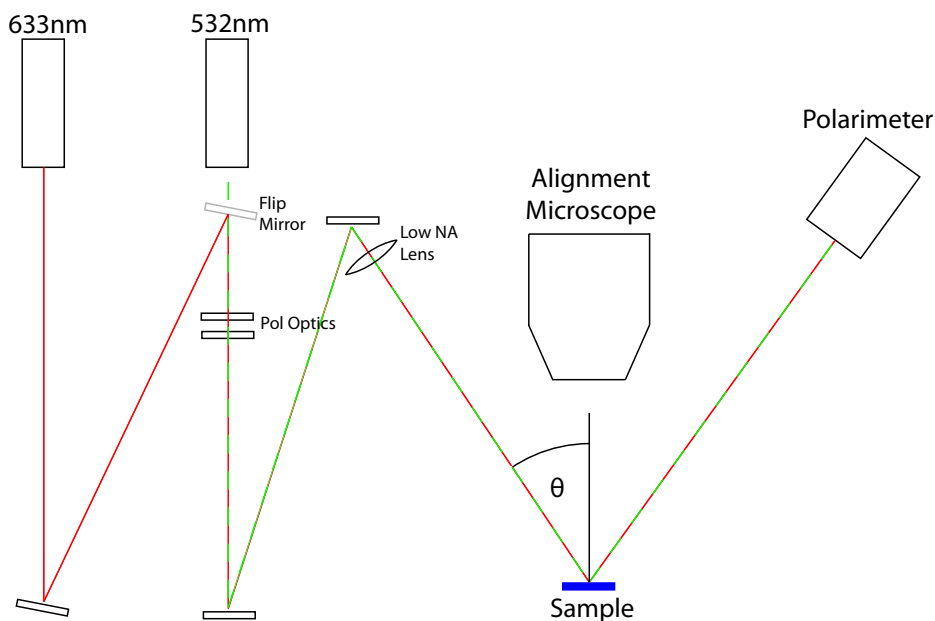


Figure 2.6: Diagram of the ellipsometric experimental setup.

cal constants of the implanted regions, we constructed a bench-top two-wavelength ellipsometry system as follows: Each Si:Ga pad was illuminated using laser light (532nm and 632.8nm) which came to a low numerical aperture focus (with spot diameter less than the pad dimension); the reflected stokes parameters were then measured versus the angle  $\theta$  using a commercial polarimeter (Thorlabs) as seen in figure 2.6. Given an incident beam with a known Stokes vector, the measured reflected Stokes parameters and normal incidence reflectivity, the optical constants  $n$  and  $k$  were fit to a thin film model.

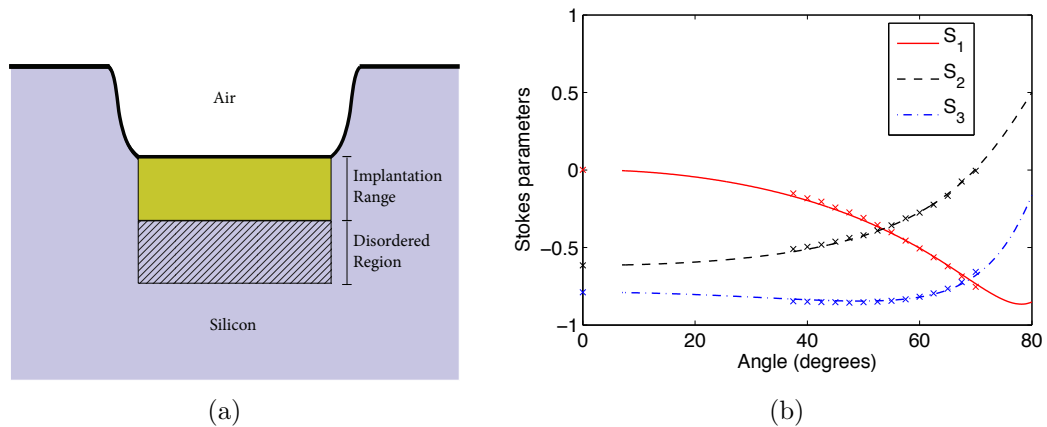


Figure 2.7: Left: Geometry used for thin film model consisting of a 40 nm implanted region with unknown refractive indices  $n$  and  $k$  on top of a 40 nm region of disordered (amorphous) silicon. Right: Example set of Stokes parameters ( $S_1, S_2, S_3$ ) vs angle on reflection off a  $0.3 \text{ nC}/\mu\text{m}^2$  Si:Ga pad on silicon at 632.8 nm. Lines shown are plotted from the thin film model fit to the data.

An implanted sample will typically consist of a high concentration region near the surface and a sub-surface combination of implanted ions and disordered silicon, as seen in figure 2.7(a). The usual projected range for 30keV Ga ions predicts a high concentration depth of about 40nm. This was confirmed by etching and inspecting the layer using electron microscopy. To model the sub-surface region, we assume a 40nm region of disordered material in which the optical constants are

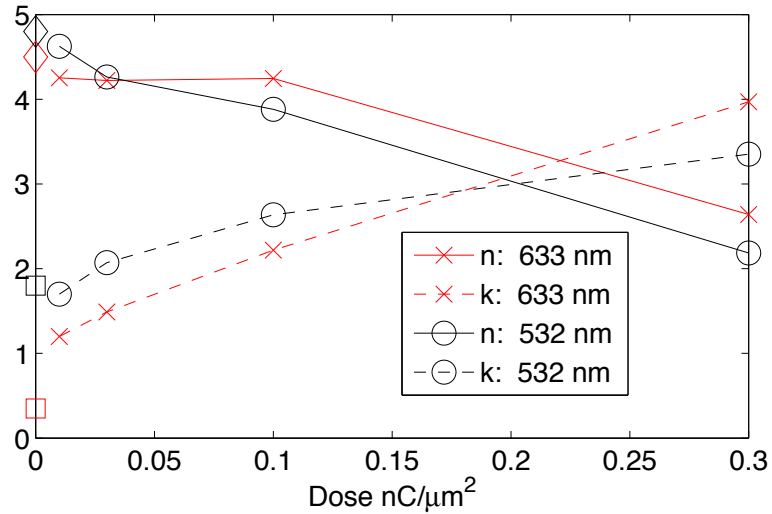


Figure 2.8: Refractive index ( $n$  and  $k$ ) vs dose for four Si:Ga pads at 532nm and 632.8nm. Lines shown are a guide to the eye. The diamonds and squares represent the measurements of Fried et. al. for amorphous silicon.

those of amorphous silicon[61]. Using these assumptions, we were able to apply a two-parameter fit ( $n$  and  $k$ ) and obtain a good fit to the data, an example of which is shown in figure 2.7(b) for a dose of  $0.3 \text{ nC}/\mu\text{m}^2$ .

The fit was constructed assuming two uniform layers on an air-silicon interface. The top layer was the unknown Si:Ga layer; it was calculated that the layer was 40 nm thick due to the fact that the gallium was implanted at 30KV. The bottom layer was a thin layer of amorphous silicon, which had been disordered by stray gallium ions but its refractive index would not be the same as the upper layer due to the fact that there far fewer gallium ions implanted at that depth. In reality the refractive index will vary smoothly from the interface to the substrate but for fitting purposes the film was split. Using this two film stack, we were able to fit the data with good accuracy as seen in figure 2.7(b).

The results for the four pads tested are summarized in figure 2.8.

## 2.5 Broadband Measurement of Si:Ga Optical Properties

To determine the optical constants over a broad spectrum, reflectance data was taken in the visible to near infra-red. A fiber based reflectometer (Audiodev) was used to take reflectance data of differently dosed Si:Ga pads from 500 to 1100nm. The instrument is constructed in a confocal arrangement in which a low numerical aperture focused beam is incident on the sample at 7 degrees with the reflected light collected in the spectrometer. The reflection from the sample is measured relative to a high reflectance standard (Semrock Maxmirror<sup>TM</sup>). Because the size of the focused beam is comparable to, but not much smaller than, the pad, a portion of the reflected light interacts with the surrounding silicon rather than the implanted region. To account for this, we took precise reflectance measurements at 532 nm using a laser source and a separate reflectance measurement from the bare silicon in order to compute the fraction of the beam reflecting off the pad for each measurement. Figure 2.9 shows the reflectance of a 0.1nC/ $\mu\text{m}^2$  dose Si:Ga pad. For additional accuracy, a second reflectance measurement was taken by placing a transparent window of a glass material with known optical constants (BK7) over the pad. The air gap (inferred from the reflectance measurement) was 1480 nm. The combination of the two reflectance measurements were combined with the ellipsometric measurements to infer n and k over a spectral region from 500 to 1000 nm in wavelength.

A fit was constructed that makes use of simplex optimization using 10 free parameters (4<sup>th</sup> order polynomial in both n and k) to minimize a merit function consisting of a weighted combination of rms reflectance error and the mean-square deviation from the ellipsometric data. Since polynomial fits can be unstable at the end points, a penalty was added to the merit function for large slopes in the

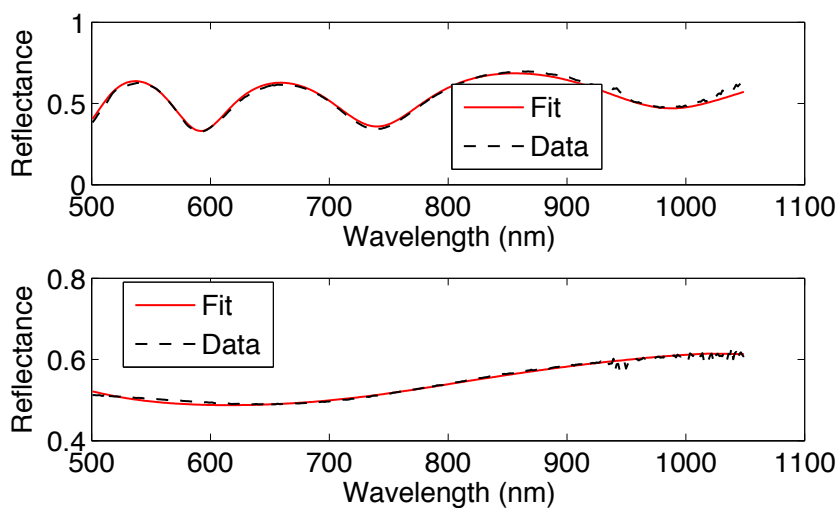


Figure 2.9: Broadband reflectance data from a  $0.1\text{nC}/\mu\text{m}^2$  dose Si:Ga pad. Upper: Reflectance from a BK7/Air/Si:Ga structure; Lower: Reflectance from a bare Si:Ga pad.

real part of the refractive index. Figure 2.10 shows representative spectral fits for two doses.

It is well known that the first effect of such an implantation is a disordering of the silicon host material, a process that, in the visible region, significantly changes the refractive index of the silicon to optical constants closer to liquid silicon than crystalline silicon (the optical properties change further with annealing and/or other means of thermal relaxation). This is seen in the refractive index at low doses; indeed, the refractive index at 633 nm stays close to that of amorphous silicon up to a value of about  $0.1\text{ nC}/\mu\text{m}^2$  and then appears to steadily decrease as the fraction of Gallium increases in the silicon. We therefore suggest that the implanted region is characteristic of a mixture of miscible liquids in which both the silicon and gallium are disordered enough to destroy any long range order or crystalline phase.

The spectral dependence of  $n$  and  $k$  (Fig. 2.10) suggests that the  $k$  value of Si:Ga is dominated by the gallium [62] in the red and infrared spectral regions,

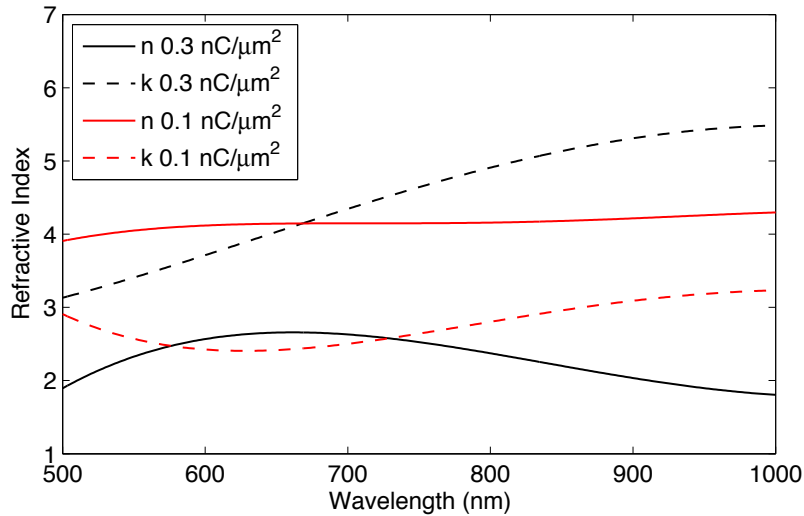


Figure 2.10: Thin film fit of optical constants  $n$  and  $k$  versus wavelength for pads with gallium implantation doses of 0.1 and 0.3  $\text{nC}/\mu\text{m}^2$ .

especially for the higher doses. The suppression of  $n$  at long wavelengths and high doses achieves a condition necessary for plasmonic materials, that the real part of the dielectric constant  $n^2 - k^2$  be negative. Indeed, the trends in the near infrared region suggest that for sufficiently high  $\text{Ga}^+$  doses, Si:Ga could have some uses as a plasmonic material in the 1-2  $\mu\text{m}$  spectral range.

The broadband reflectance measurements concentrated on the high dose material for two reasons: 1) For potential plasmonic applications, cases in which  $k$  approaches and exceeds the value of  $n$  are most interesting; 2) We have found that the best etch resistance occurs for structures fabricated with doses exceeding 0.1  $\text{nC}/\mu\text{m}^2$ .

As a preliminary evaluation of Si:Ga as a potential plasmonic material, we can also compare the material figures of merit associated with the surface plasmon polariton ( $Q_{\text{SPP}}$ ) and the localized surface plasmon resonance ( $Q_{\text{LSP}}$ ) for the

wavelength range used for the fitting of  $n$  and  $k$ [62]:

$$Q_{\text{LSP}} = \frac{k^2 - n^2}{2nk} ; Q_{\text{SPP}} = \frac{(n^2 - k^2)^2}{2nk}.$$

While considerably lower than the noble metals (Au and Ag, in particular), they are sufficient to warrant further investigation if only because of the ease with which Si:Ga can be fabricated by the FIB process.

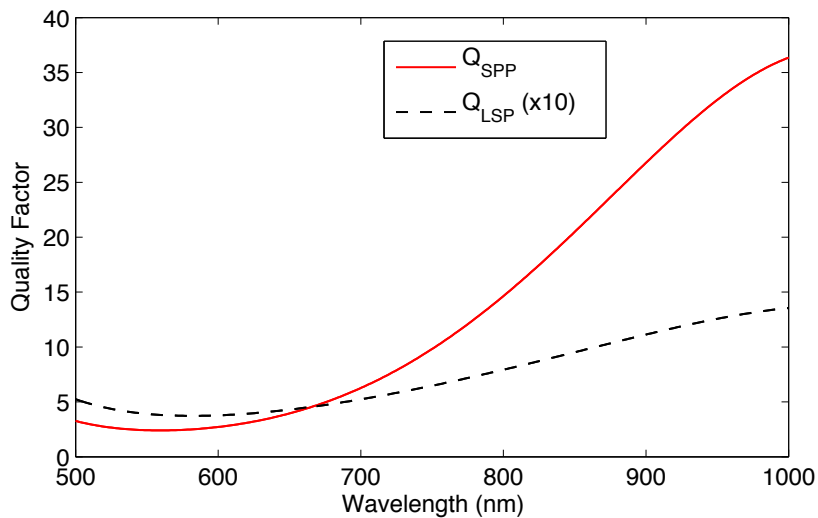


Figure 2.11: Plasmonic quality factor ( $Q_{\text{SPP}}$  and  $Q_{\text{LSP}}$ ) of  $0.3 \text{ nC}/\mu\text{m}^2$  Si:Ga.

## 2.6 Drude Model

When looking at the optical properties of a material, it is often useful to compare it to a physical model. The Drude model, is often used when looking at the optical properties of metals and sometimes semiconductors. The Drude model is centered around how the electric field oscillations of light interact with the electrons in a

material, and contains three terms,

$$m^*\ddot{\mathbf{r}} + m^*\gamma\dot{\mathbf{r}} + e\mathbf{E} = 0 \quad (2.1)$$

the mass times acceleration term, a damping term, and the force of the light's electric field on the electrons respectively; where  $m^*$  is the effective mass of the electron,  $\gamma$  is the damping constant,  $e$  is the electron charge,  $\mathbf{r}$  is the time-dependent electron position, and  $\mathbf{E}$  is the incident light's electric field. The Drude model, can be solved for  $\mathbf{r}(t)$ , and from that it is possible to solve for the dielectric constant given knowledge of the density of electrons. Doing so, you can obtain,

$$\varepsilon(\omega) = \varepsilon_\infty - \frac{\omega_p^2}{\omega^2 + i\gamma\omega} = \varepsilon_{\text{Re}}(\omega) + i\varepsilon_{\text{Im}}(\omega), \quad (2.2)$$

where  $\varepsilon_\infty$  is the value of  $\varepsilon$  in the limit as  $\omega$  approaches  $\infty$ , and  $\omega_p = \sqrt{\frac{ne^2}{\varepsilon_\infty\varepsilon_0m^*}}$  is the plasma frequency. This can be rewritten in terms of the real and imaginary parts of  $\varepsilon(\omega)$ ,

$$\varepsilon_{\text{Re}}(\omega) = \varepsilon_\infty - \frac{\omega_p^2}{\omega^2 + \gamma^2} \quad \text{and} \quad \varepsilon_{\text{Im}}(\omega) = \frac{\gamma\omega_p^2}{\omega^3 + \gamma^2\omega}. \quad (2.3)$$

Using the Drude model, we can look at Si:Ga compared to a few noble metals: gold and silver. Figure 2.12 shows the real and imaginary parts of the dielectric function as a function of angular frequency,  $\omega$ .

In order to obtain the Drude fits, we optimized the real and imaginary parts of the dielectric function with a least squares fit. The model fits silver very well in for both the real and imaginary part. Gold can be represented fairly well with it too, but the fit breaks down a bit for the imaginary part at high frequency. The model does a good job fitting to the real part of the dielectric function of  $0.3\text{nC}/\mu\text{m}^2\text{Si:Ga}$  but does not fit the imaginary part very well. The parameters used for the Drude fit for Si:Ga shown in figure 2.12 are:  $\varepsilon_\infty = 12.1$ ,

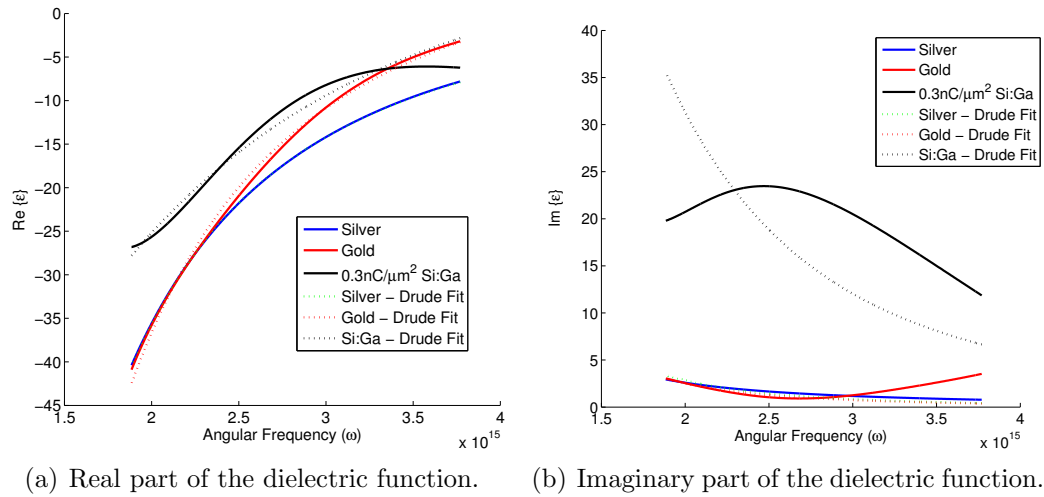


Figure 2.12: Real and imaginary parts of the dielectric function plotted vs.  $\omega$  for silver, gold and  $0.3\text{nC}/\mu\text{m}^2$  Si:Ga. Drude model shown with dotted lines for the materials.

$\omega_p = 1.595 \times 10^{16} \frac{1}{\text{s}}$ , and  $\gamma = 1.68 \times 10^{15} \frac{1}{\text{s}}$ . If the Drude model were an accurate fit, we can obtain an estimate of the free electron density. We know based on the fact that  $\epsilon_\infty = 12.1$  that the material is acting similar to a semiconductor; we can therefore use an effective electron mass similar to other semiconductors of  $m^* = 0.05m_0$ . This means that the Drude model predicts a free electron density in the  $10^{22} - 10^{23} \text{ cm}^{-3}$  range.

## 2.7 Implantation Masks

It is often beneficial when designing guided mode resonators to be able to control the strength of the perturbation a grating layer has on the light in a waveguide. Physically corrugated structures tend to have a large perturbation, due to the large disparity in dielectric functions of the grating and air. This can be partially alleviated by filling the trenches with some dissimilar dielectric material; this can cause issues for further fabrication steps since the corrugated grating shape tends

to make a clone of itself on the top layer of the coated dielectric. This effect is visible in figure 4.1(b) in a fabricated grating example. One method to overcome this is to use a grating that is planar in physical dimension, but has a periodic index variation spatially.

To make FIB assisted gallium implanted silicon a feasible means of creating an index only grating, we investigated a few different materials to act as an implantation mask. An implantation mask would work as a sacrificial dummy layer, allowing some ions to be implanted through it and some to be implanted into it. Instead of milling into our substrate we would be milling into the mask layer. The mask would need to be thick enough to finish implantation before the substrate would start to be milled, but it can't be too thick, since the ions will only travel a certain distance into the material. For this reason, we typically chose our masks to be only a few nanometers thicker than necessary for the given dose we plan on implanting. Once the implantation has been done, the mask is removed, typically via a chemical wet etch, but depending on the mask material, reactive ion etching or simple oxygen plasma cleaning may suffice.

### 2.7.1 Aluminum Oxide Masks

The uniformity of the implantation mask was one of the first major requirements we set on an implantation mask. For this reason we thought that choosing a material that can be deposited via atomic layer deposition (ALD) was a good idea. One of the easiest materials to deposit in an ALD system is Aluminum Oxide ( $\text{Al}_2\text{O}_3$ ) since it has fairly simple process and is deposited *relatively* quickly. The  $\text{Al}_2\text{O}_3$  ALD process is a simple four step cycle: pulse water ( $\text{H}_2\text{O}$ ), wait, pulse Trimethyl Aluminum (TMA), wait, repeat. Each cycle of the process builds 0.11 nm of  $\text{Al}_2\text{O}_3$ , and takes about 10 seconds.

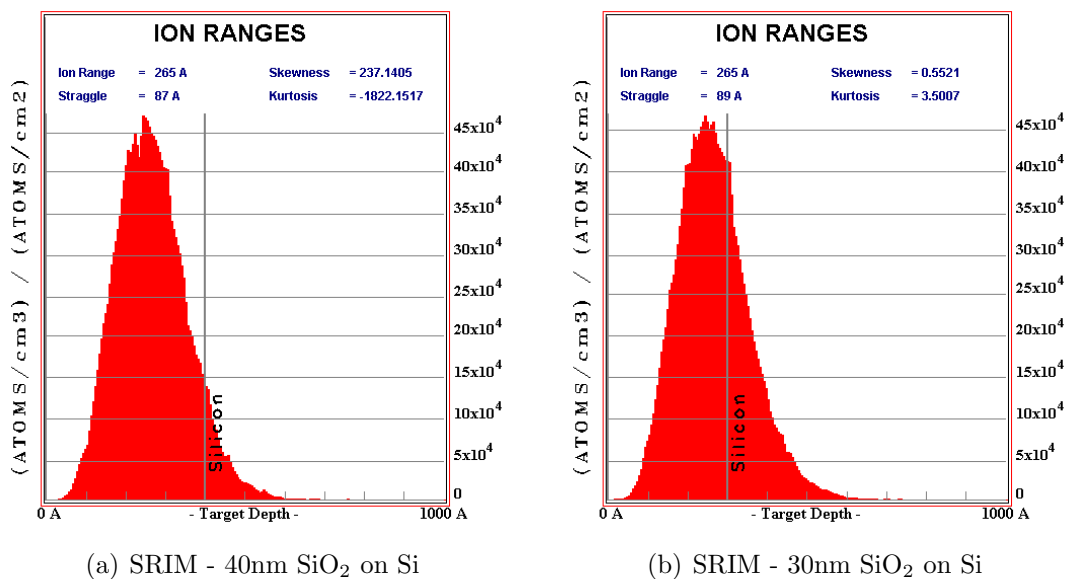


Figure 2.13: SRIM - 30kV Ga<sup>+</sup> implanted into SiO<sub>2</sub> mask on silicon.

## 2.7.2 Silicon Dioxide Masks

The implantation mask that we decided on using for most experiments was silicon dioxide (SiO<sub>2</sub>). The main issue with using the Al<sub>2</sub>O<sub>3</sub> mask, is that we were worried that implanting through the mask, we could be contaminating the substrate some with ballistically implanted aluminum atoms from the mask. Switching to SiO<sub>2</sub> alleviates this issue some. Deposition of SiO<sub>2</sub> was done with both sputtered and evaporated films, and there was no discernible difference in mask performance between the two for our purposes. Figures 2.13 and 2.14 show the gallium ion implantation distribution in silicon for 30kV Ga<sup>+</sup> implanted through varying mask thickness of SiO<sub>2</sub> as calculated with SRIM; this is modeled for varying thicknesses to simulate how the implantation will evolve with thinning mask thickness as it gets milled away. Both alumina and silica mask milled at about the same rate as the bulk silicon.

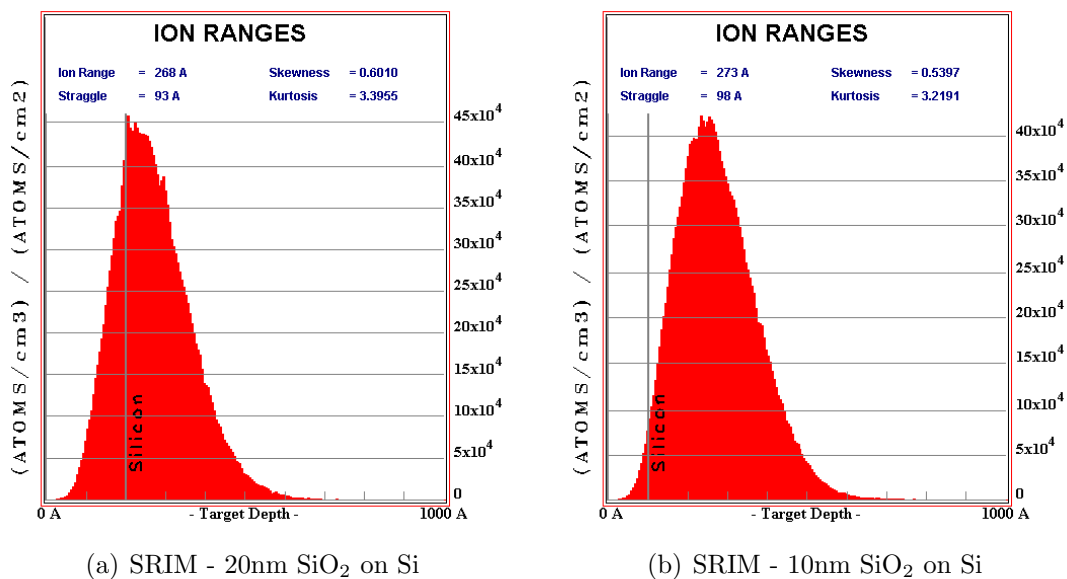
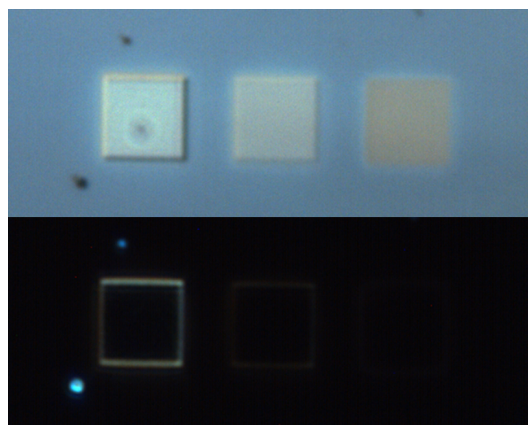
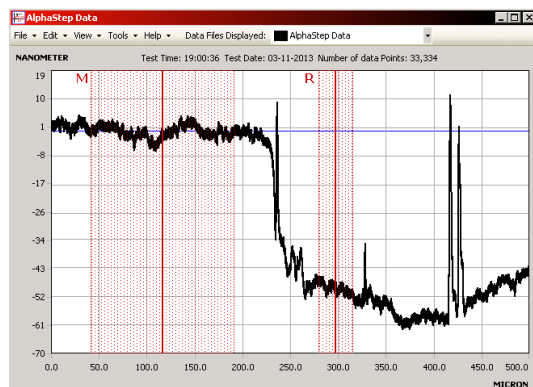


Figure 2.14: SRIM - 30kV Ga<sup>+</sup> implanted into SiO<sub>2</sub> mask on silicon.

### 2.7.3 Carbon Masks

The final mask material we considered using was carbon. The primary reason for this was that carbon is easy to deposit via a thermal evaporator, and it is easy to remove via an oxygen plasma ash. Figure 2.15(b) shows a sample that was coated with 50 nm of carbon prior to gallium implantation. The carbon coated sample looks almost identical to that of the uncoated Si:Ga sample shown in figure 2.1(a). To test the effectiveness of the carbon mask, an identical dose array was implanted to that used in figure 2.1(a), three pads of 0.1, 0.2, and 0.3nC/μm<sup>2</sup>. An AFM slice of the sample is shown in figure 2.16.

For the highest dose, 0.3nC/μm<sup>2</sup>, the implantation only milled about 30 nm into the silicon, and only milled about 7-8 nm for a dose of 0.2nC/μm<sup>2</sup>. Thus the carbon mask is more robust to ion milling than the alumina and silica masks. The most interesting result however is that for the lowest dose, 0.1nC/μm<sup>2</sup>, the carbon mask remained after the oxygen plasma clean. This resistance to ashing,



(a) Measurement of the carbon on silicon step using an AlphaStep surface profilometer. The difference in height between the measured region and reference region (labeled M and R respectively) is 49 nm.

(b) Light microscope images of gallium implantation through a carbon mask post plasma ash. Top: Differential interference contrast (DIC) mode. Bottom: Dark field mode.

Figure 2.15: Si:Ga: carbon mask

could have profound uses, such as drawing intricate contacts on nanostructures provided that gallium implanted carbon has appropriate conductive properties.

## 2.8 Discussion of Applications

The implantation properties of Si:Ga make it an attractive material for use in a variety of applications that require nanostructured materials.

One major limitation of Si:Ga is that once the ion implantation is above a certain dose, the material becomes thermally unstable. To test how the thermal instability of the gallium correlates with the implantation dose, we made an array of  $5\mu\text{m}$  squares of uniform dose ranging from  $0.01$  to  $0.25\text{ nC}/\mu\text{m}^2$ . This sample was placed in an oven at  $250^\circ\text{C}$  for half an hour, and pads above a certain dose, start to show gallium leaching from the surface, seen in figure 2.17. It can be seen that for doses above about  $0.06\text{ nC}/\mu\text{m}^2$  the implanted gallium starts to leach to the surface. Above that the gallium tends to make the surface incredibly rough.

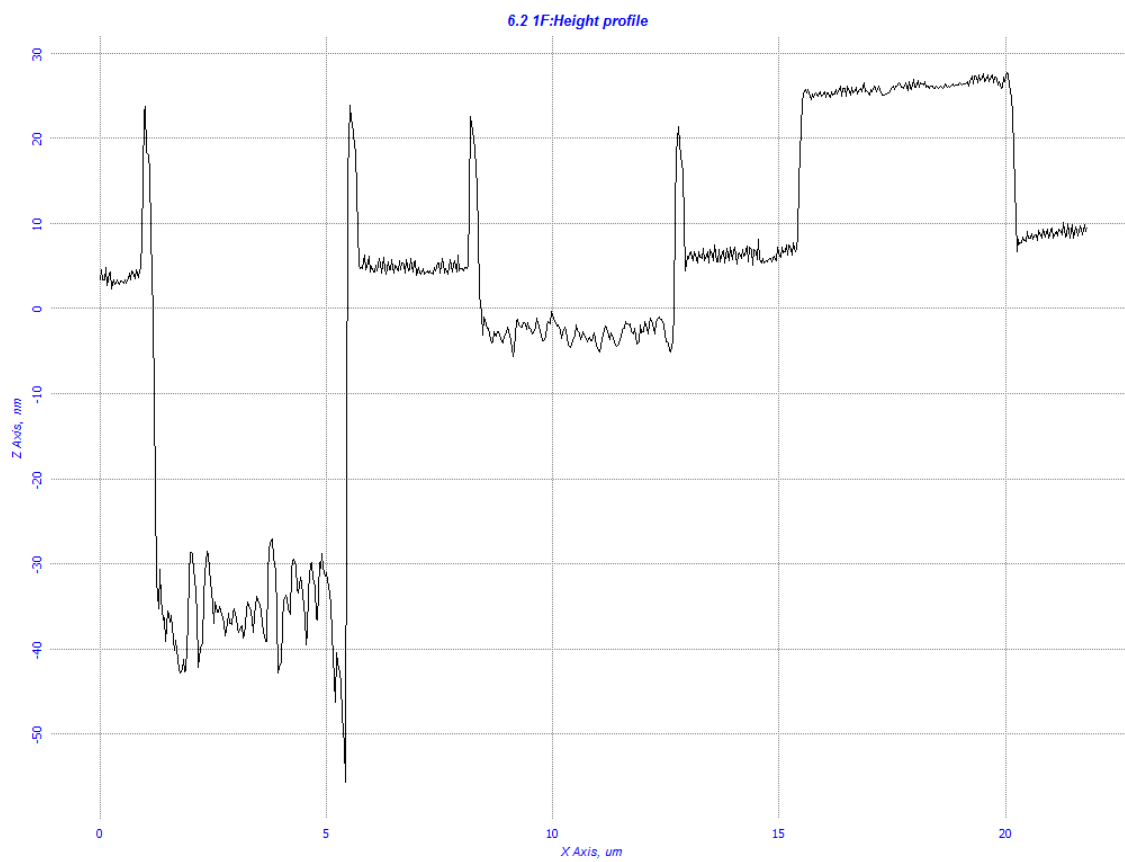


Figure 2.16: AFM slice through all three pads of the Si:Ga: carbon mask sample.

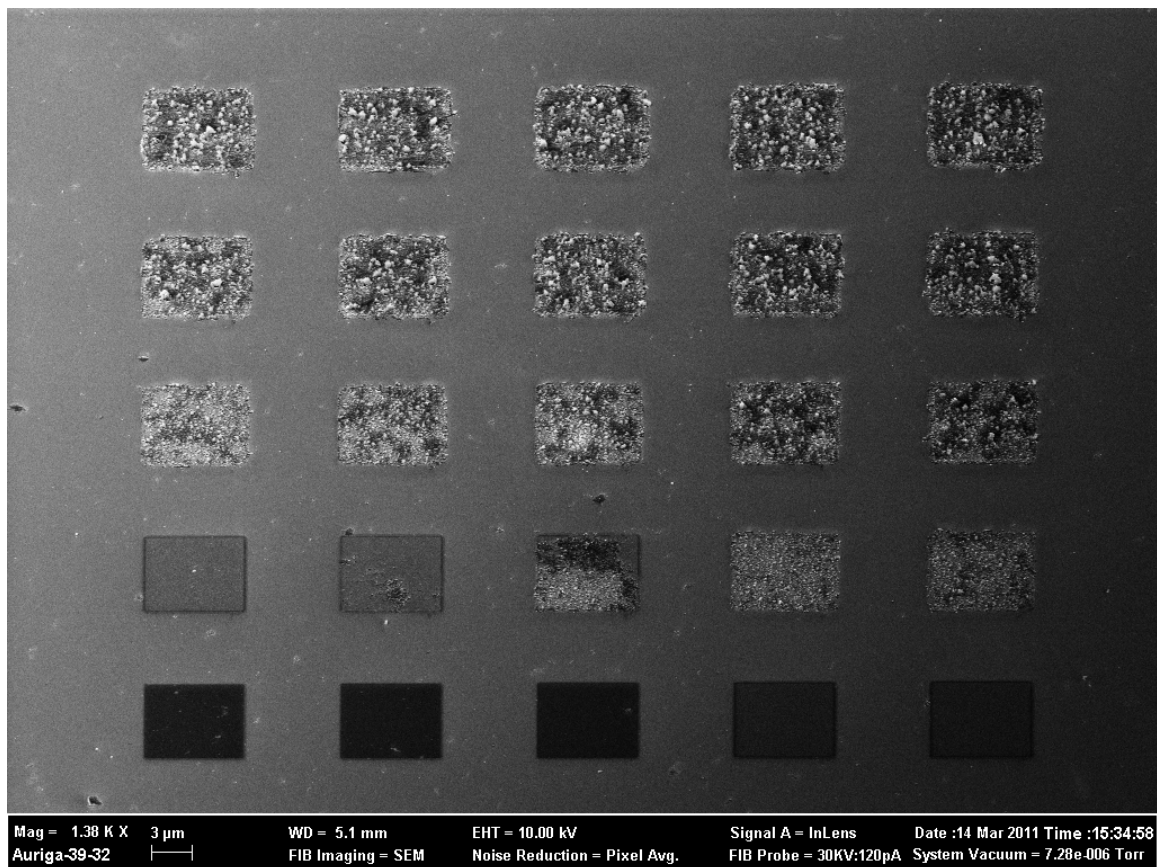


Figure 2.17: SEM micrograph of a Si:Ga sample dose array ( $0.01 - 0.25\text{nC}/\mu\text{m}^2$ ) following a 30 minute bake at  $250^\circ\text{C}$ .

## 2.9 Conclusion

In summary, we have reported measurements of the optical constants of gallium implanted silicon and found that doses exceeding  $0.1\text{nC}/\mu\text{m}^2$  may support surface plasmon resonances in the near infrared. We have also investigated the use of using mask for ion implantation to result in a non-corrugated surface. Carbon masks have been shown to have low milling rate, and interesting properties when lightly doped. The thermal stability of Si:Ga has been investigated, and we have shown that the stability of the material decreases with increasing ion dose. The measured optical constants of Si:Ga will allow us to model the structures we fabricate in the next chapter.

## Chapter 3

# Fabrication, Measurement, and Analysis of Gallium Implanted Silicon Nanostructures

### 3.1 Introduction

The optical properties of assemblies of nanowires are of great recent interest for applications ranging from optical antennae to solar energy. Nanowires are, by nature, sensitive to the local polarization of the illuminating field. Gallium doped silicon wires were first reported by La Marche et al. in 1983 [63]. They discovered that doping silicon with gallium can make it resistant to certain forms of chemical etching; since Gallium is used extensively in focused ion beam systems, it was then natural to explore the potential uses of Si:Ga nanowires. For polarimetric microscopy, it is also useful to create sample targets that have retardance or diattenuation that can be engineered over a wavelength or sub wavelength scale.

The most common nanowires for polarimetric application are wire grid polarizers that, for optical frequencies, comprise subwavelength arrays of a noble metal on a glass substrate. As polarizing elements, they can exhibit high extinction

over a broad bandwidth when used in transmission, with a similarly high diattenuation in reflection. They are also important element in various optical antenna designs, especially when used near a plasmonic resonance. So far, the polarization properties of Si:Ga wires remain unexplored; in this chapter, we will look into the fabrication and properties suspended Si:Ga nanowire arrays.

## 3.2 Sample Fabrication

### 3.2.1 Gallium Implantation

As mentioned previously, a FIB is capable of writing out intricate patterns, unlike the uniformly doped pad we investigated in the previous chapter. In this chapter we make use of this capability, and investigate the implantations of gallium lines that will eventually be etched to form Si:Ga nanowires. To do so, we first deduce the dose necessary for Si:Ga to become resistant to chemical etches. To do this a sample was created with a  $0.01$  to  $0.25\text{nC}/\mu\text{m}^2$  array of  $7 \times 7 \mu\text{m}$  squares, and processed using a reactive ion etch.

Figure 3.1 shows the results; even for the lowest dose of  $0.01\text{nC}/\mu\text{m}^2$ , there is evidence of Ga implantation. It is clear that as the dose increases, the thin gallium implanted layer is becoming a better mask for the RIE. At a threshold of about  $0.04\text{nC}/\mu\text{m}^2$ , the layer becomes an effective mask, allowing a pillar to form below it, but with some pinholes punched into it. By  $0.05\text{nC}/\mu\text{m}^2$ , the film is robust enough to stand up to a ten minute RIE.

It is interesting to note that there are small islands on the pads that look brighter in the SEM (more secondary electrons created by the electrons). These islands start to become larger and more numerous until a dose of  $0.16\text{nC}/\mu\text{m}^2$  where the surface looks mottled. From a dose of  $0.17\text{nC}/\mu\text{m}^2$  to the maximum dose applied of  $0.25\text{nC}/\mu\text{m}^2$  there is little change in appearance under SEM inspection.

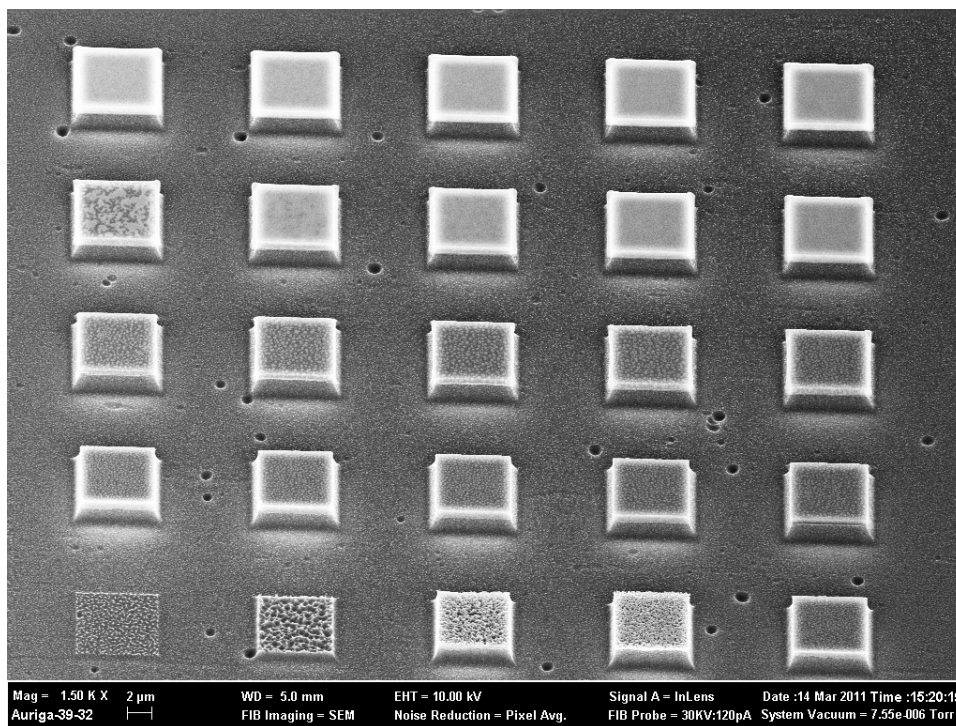


Figure 3.1: SEM micrograph of Si:Ga dose array following a ten minute RIE etch in 30:1 Ar:SF<sub>6</sub> taken at 54° and a tilt compensation of 36°.

However, the optical appearance does change - this will be discussed later, when we examine its optical properties.

With the etch threshold established, we now turn to the fabrication of Si:Ga nanowires. Implanting wires and implanting pads differ in the FIB writing parameters. When implanting a broad area, the beam size is relatively unimportant. The main concern is the size of the beam relative to the desired pattern. Narrow wires require a smaller beam, but reducing the beam size in a FIB requires a smaller aperture size. This in turn reduces your specimen current by the change in the area of the aperture. It therefore often takes longer to write a small set of wires than to write a large pad. As a result, specimen currents for nanowires are typically in the range of 1-2 pA, compared to 1-20 nA for a pad.

In order to keep the nanowires freestanding and suspended above the surface,

the wires were surrounded by a scaffold structure for support following an undercutting etch. In the case of concentric circle structures, perpendicular nanowires running through the circle center functioned as support. Support wires are anchored to a square pad (also doped into the substrate) surrounding the structure, allowing the nanowire to be suspended off the substrate once the etch process is completed. In order to control the pattern and dose of the gallium implantation, third party software was used to drive the FIB scan coils (Fibics' Nanopattern Visualization Engine 3) and beam blanker (Raith).

Figure 3.2 shows a silicon wafer after it has been doped with a dose of  $0.1 \frac{nC}{\mu m^2}$  from a focused beam of gallium ions accelerated at the standard 30kV. Any wire structure that can be drawn in two-dimensions can be doped into the silicon, provided an unobtrusive support structure can be devised.

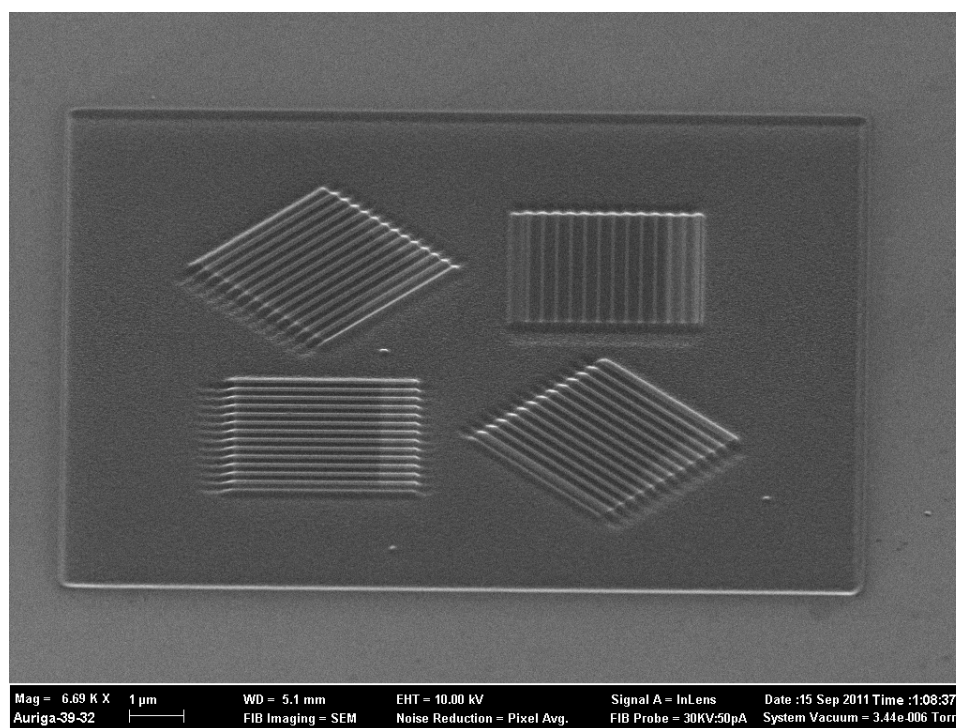


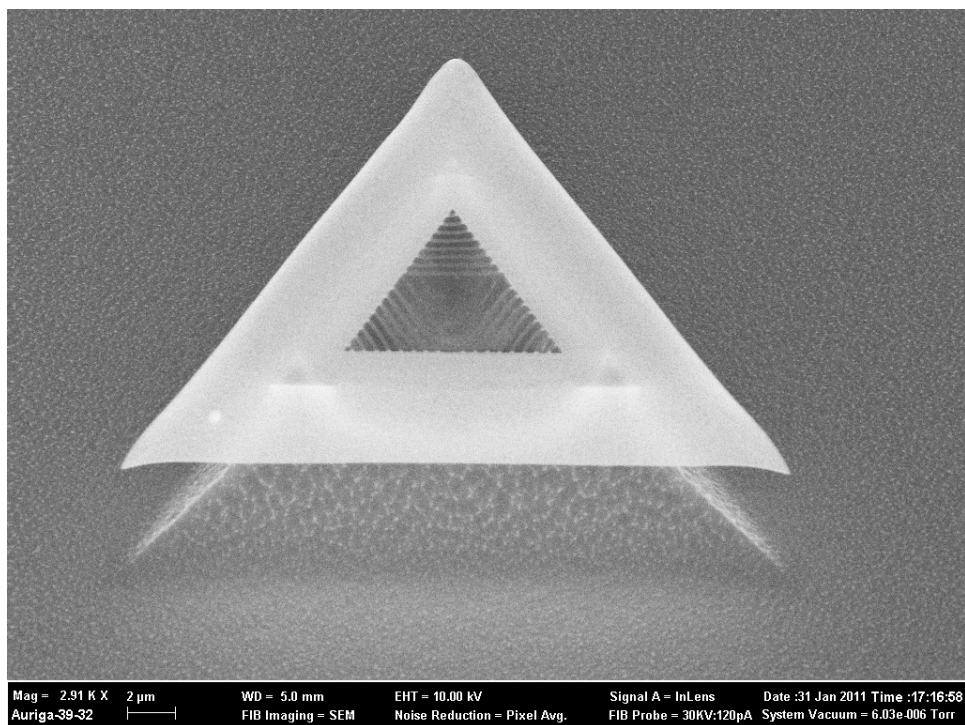
Figure 3.2: SEM micrograph of gallium implantation taken at  $54^\circ$  and a tilt compensation of  $36^\circ$ .

### 3.2.2 Sample Processing

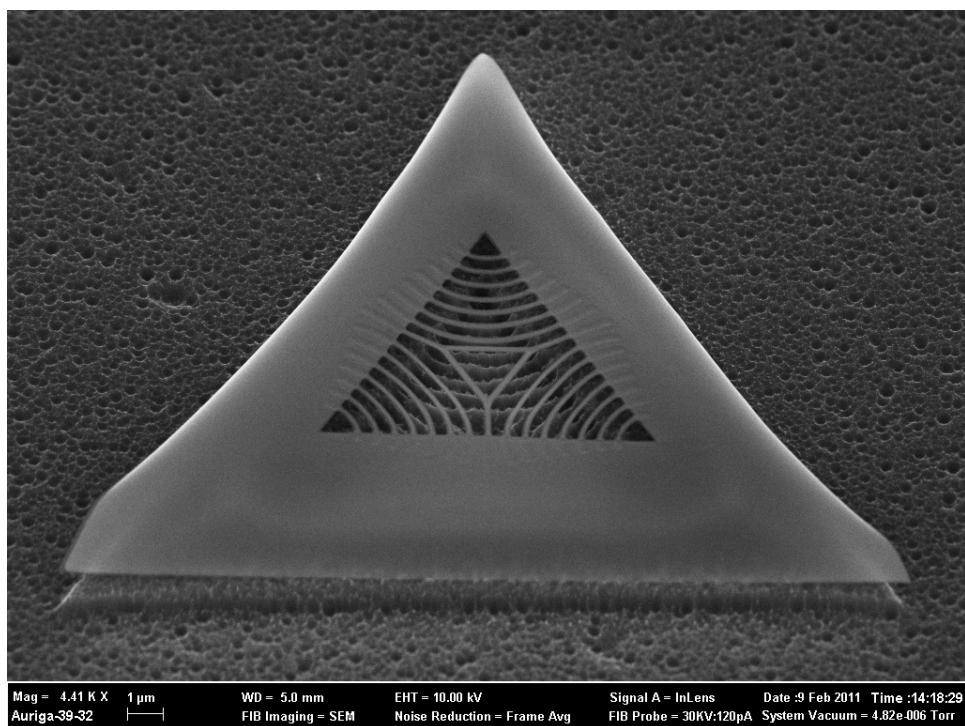
Once the gallium lines have been implanted, the next step in the fabrication process is to use a dopant-selective etch to free the Si:Ga nanowires from the surrounding silicon. A good etch should leave the wires well defined, and leave both wires and surface with low roughness. A dry etch (RIE) can be done with sulfur hexafluoride ( $\text{SF}_6$ ) and argon gases in a reactive ion etch system. The gallium doped regions are less affected by the etch, thus leaving the Si:Ga nanowires suspended in air. The etch process is extremely dependent on the ratio of Ar to  $\text{SF}_6$ , as well as the absolute process pressure in the chamber. Figure 3.3 shows two structures with identical gallium implantation but different gas proportions and pressures.

Both samples had  $0.1\text{nC}/\mu\text{m}^2$  nanowires implanted with a supporting triangle that had a dose of  $0.2\text{nC}/\mu\text{m}^2$ . The gallium lines were 150 nm wide, and had a 300 nm period. Figure 3.11(a) shows the results of an etch that used 10:1 Ar: $\text{SF}_6$ , at a base pressure of  $76\text{mTorr}$  for 10 minutes. This etch seems to have followed the silicon crystal planes, and it left the surface quality high, but the wire definition is quite poor. Figure 3.9(b) shows the results of a 40min 1:10 Ar: $\text{SF}_6$  etch. Even though this etch was four times as long, the delicate nanowires appear to have very good definition. The downside of this etch however is that the surface of the surrounding silicon is extremely rough and pitted.

Instead of using a dry etch, a wet etch can be done in either sodium hydroxide (NaOH) or potassium hydroxide (KOH)[63]. We found that wet etching tends to leave a good surface quality, and wires that have good definition. Circular nanowires have been straightforward to etch but linear nanowires tend to become malformed when the substrate dries after the etch. Critical point drying (CPD) can be done to minimize the effect of surface tension during drying, by bypassing the liquid to gas phase transition. Figure 3.4 shows a comparison of identically

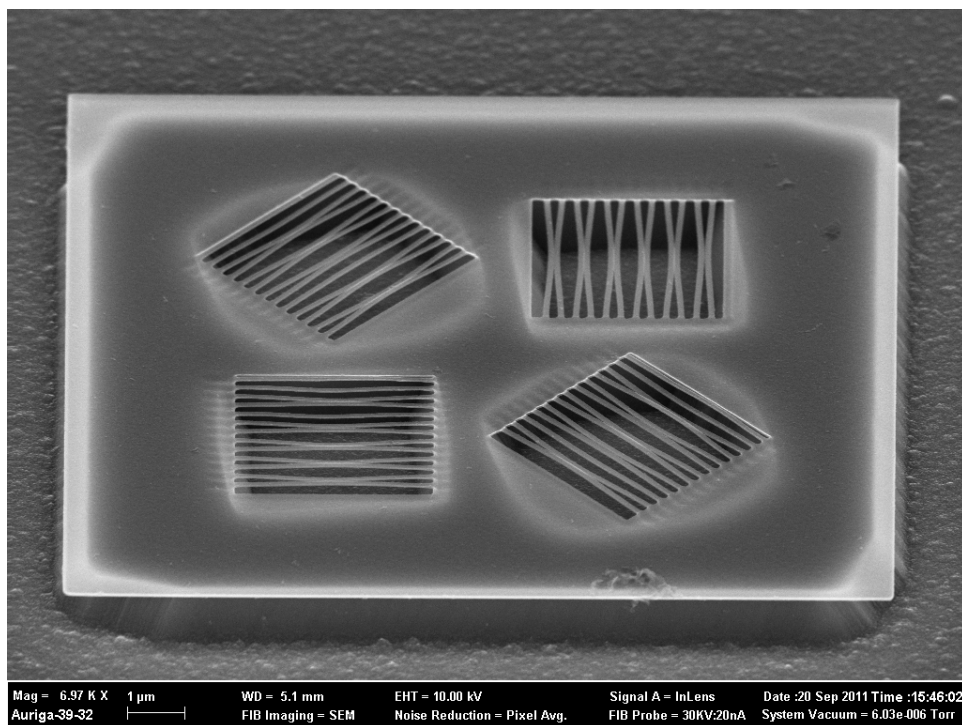


(a) Ten minute RIE done with 10:1 Ar:SF<sub>6</sub>.

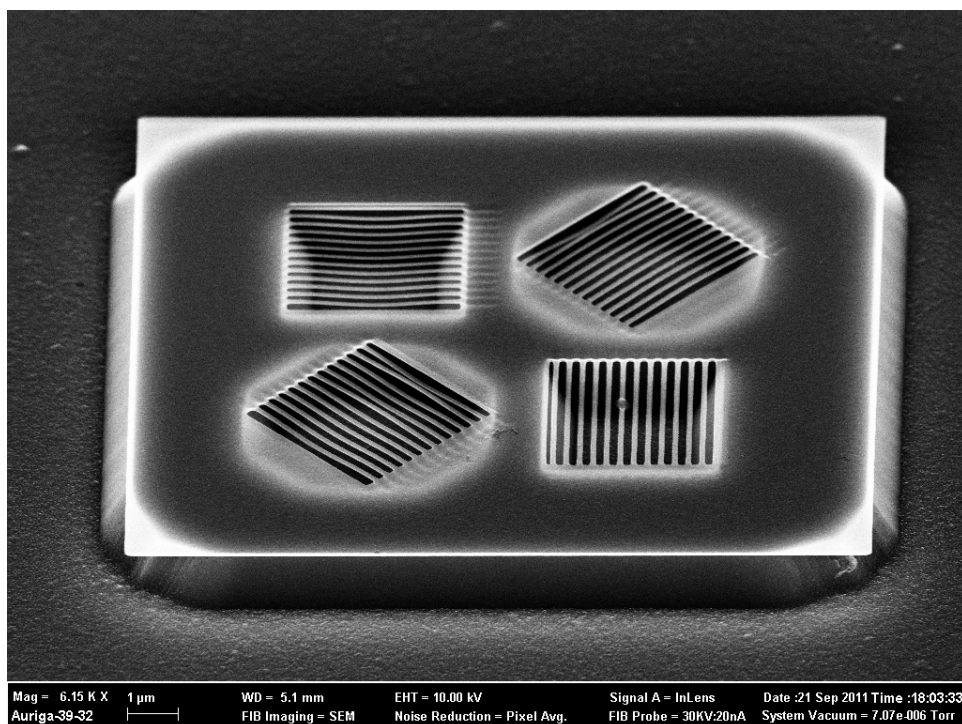


(b) Forty minute RIE done with 1:10 Ar:SF<sub>6</sub>.

Figure 3.3: Comparison of different reactive ion etch recipes.



(a) NaOH etch done for 150s at 50C air dried.



(b) NaOH etch done for 150s at 50C critical point dried.

Figure 3.4: Comparison of air dried and critical point dried wet etched nanowire arrays.

implanted and etched samples with and without CPD. One interesting note about writing nanowires is that the post-etch wire definition seems to be better if the gallium line was implanted in a single pass, as opposed to multiple pass as we used in chapter 2.

The final recipe used to create Si:Ga nanowires is to implant 125 nm gallium lines (connected to a support structure) with a dose of  $0.15\text{nC}/\mu\text{m}^2$  using a 2pA ion beam, followed by a combination RIE/liquid etch sequence. The etch begins with a 2 minute 30:1 Ar:SF<sub>6</sub> etch at 30 watts and  $\sim 75\text{mTorr}$  base pressure followed by a 2.5 minute wet etch in 50°C saturated NaOH solution. The sample is moved from the NaOH to ethanol, carefully not allowing it to dry. After soaking in ethanol for a few minutes, it can be dried using CPD.

### 3.3 Polarimetric Microscope

In order to measure the polarization properties of the Si:Ga nanowires, we built a polarimetric microscope, with an operational wavelength of 532nm. A diagram of the full system is shown in figure 3.5. The illumination system consists of a doubled Nd:YAG laser, rotating diffuser, condenser lens, infrared filter, and a polarization state generator consisting of a quarter wave plate and linear analyzer. The microscope has the usual selection of objectives for variable magnification and field of view. (Our imaging was typically done at 5x and 50x.) The imaging arm of the microscope has independent polarization control by means of another quarter wave plate and linear analyzer pair.

The first step to configuring the microscope was to calibrate the polarization optics in the illumination system. To do this we removed the sample stage and replaced it with a commercial polarimeter (Thorlabs). With the polarimeter in place we were able to determine the orientation of the quarter wave plate and linear polarizer necessary to get known polarization states in the sample plane.

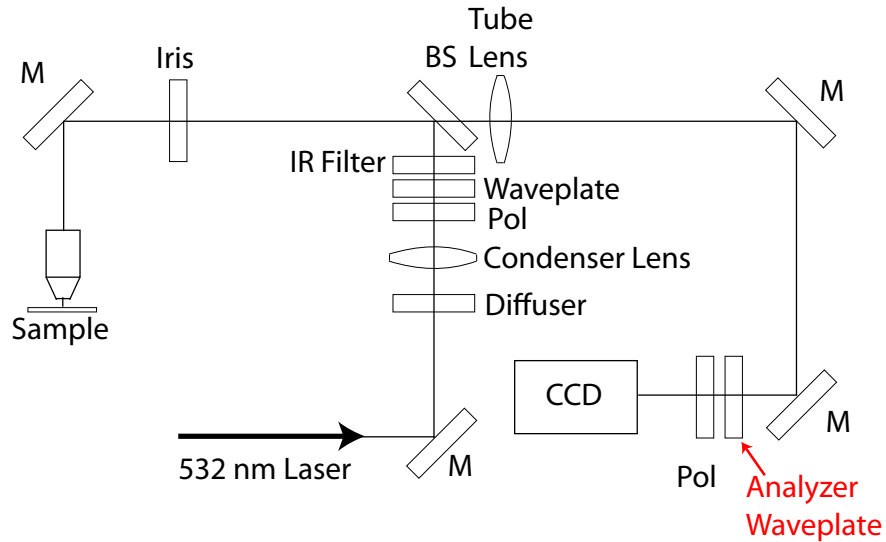


Figure 3.5: Schematic design of the polarimetric microscope.

The illumination states of interest for our retrieval algorithm are linear: horizontal, vertical,  $+45$ ,  $-45$  and circular: right and left handed. Once the illumination optics were calibrated, the next step was to measure the system Jones matrix. The system Jones matrix quantifies how the return path of the microscope (three mirrors, a tube lens and beamsplitter) affects the polarization of light between the sample and the waveplate. To find this we replaced the sample stage and placed a mirror at the focus of our objective. The CCD camera and imaging arm polarization elements were replaced by the polarimeter, and the Stokes parameters were measured in the image plane for each of the six different polarizations in the sample plane. The input (output) Jones vectors,  $\hat{\mathbf{e}}_{in}$  ( $\hat{\mathbf{e}}_{out}$ ) can be put into one matrix  $\mathbf{E}_{in}$  ( $\mathbf{E}_{out}$ ) as a collection of column vectors [13]. Then the system Jones matrix can be calculated with the following equation:

$$\mathbf{J}_{sys} = \mathbf{E}_{out} \cdot \mathbf{E}_{in}^{-1}, \quad (3.1)$$

where  $\mathbf{J}_{sys}$  is the system Jones matrix,  $\mathbf{E}_{out}$  is a collection of column Jones vectors measured in the image plane, and  $\mathbf{E}_{in}^{-1}$  is the pseudo-inverse of the collection of column input Jones vectors.

### 3.4 Sample Jones Matrix Retrieval Algorithm

To measure the sample Jones matrix, the sample is epi-illuminated with a known polarization state, and multiple images are taken at varying orientations of the analyzer quarter wave plate. Our algorithm uses six different illumination states, with five images taken for each input state; the thirty images were individually registered to a reference image in preparation for image analysis.

Once the registration is done, the next step is to use the images for each input polarization state to determine what the Stokes parameters were in the image plane. The Stokes parameters after the quarter wave plate can be calculated as follows,

$$\mathbf{S}_{out} = \mathbf{M}_{ret} \mathbf{S}_{in}, \quad (3.2)$$

$$\mathbf{M}_{ret} = \begin{bmatrix} 1 & 0 & 0 & 0 \\ 0 & \cos^2 2\theta & \sin 2\theta \cos 2\theta & -\sin 2\theta \\ 0 & \sin 2\theta \cos 2\theta & \sin^2 2\theta & \cos 2\theta \\ 0 & \sin 2\theta & -\cos 2\theta & 0 \end{bmatrix}, \quad (3.3)$$

where  $\mathbf{S}_{out}$  ( $\mathbf{S}_{in}$ ) is the output (input) Stokes vector and  $\mathbf{M}_{ret}$  is the standard Mueller matrix of a quarter wave retarder[64]. Equation 3.2 takes the form,

$$\mathbf{S}_{out} = \mathbf{M}_{ret} \cdot \begin{bmatrix} S_0 \\ S_1 \\ S_2 \\ S_3 \end{bmatrix} = \begin{bmatrix} S_0 \\ S_1 \cos^2 2\theta + S_2 \sin 2\theta \cos 2\theta - S_3 \sin 2\theta \\ S_1 \sin 2\theta \cos 2\theta + S_2 \sin^2 2\theta + S_3 \cos 2\theta \\ S_1 \sin 2\theta - S_2 \cos 2\theta \end{bmatrix}. \quad (3.4)$$

The output irradiance for any pixel may be then related to the input Stokes parameters as follows. By definition,  $S_0 = I_H + I_V$  and  $S_1 = I_H - I_V$ . Since we have a fixed horizontal analyzer following the wave plate, it follows that:

$$I_H = \frac{1}{2}(S_{0out} + S_{1out}) = \frac{1}{2} \left( S_0 + S_1 \cos^2 2\theta + \frac{1}{2} S_2 \sin 4\theta - S_3 \sin 2\theta \right). \quad (3.5)$$

For multiple measurements at a range of retarder angles  $\theta_i$ , the irradiance may be expressed as a column vector,

$$\mathbf{I} = \mathbf{W} \cdot \mathbf{S}, \quad (3.6)$$

in which  $\mathbf{W}$  is now a matrix that relates the stokes parameters to the irradiance at each angle theta:

$$\mathbf{W} = \begin{bmatrix} 1 & \cos^2 2\theta_1 & \frac{1}{2} \sin 4\theta_1 & -\sin 2\theta_1 \\ 1 & \cos^2 2\theta_2 & \frac{1}{2} \sin 4\theta_2 & -\sin 2\theta_2 \\ \vdots & \vdots & \vdots & \vdots \\ 1 & \cos^2 2\theta_N & \frac{1}{2} \sin 4\theta_N & -\sin 2\theta_N \end{bmatrix}. \quad (3.7)$$

Typically,  $\mathbf{W}$  is a rectangular matrix (in our case, we used 5 measurements), the solution (in a least-square sense) can be expressed using a psuedo-inverse of  $\mathbf{W}$ :

$$\begin{bmatrix} S_0 \\ S_1 \\ S_2 \\ S_3 \end{bmatrix} = \mathbf{W}^{-1} \cdot \begin{bmatrix} I(\theta_1) \\ I(\theta_2) \\ \vdots \\ I(\theta_N) \end{bmatrix} \quad (3.8)$$

Using equation 3.8 on each input polarization we are able to obtain the Stokes parameters at each pixel in the image plane. Once we have the Stokes parameters it is easy to convert back to Jones vectors with,

$$\hat{\mathbf{g}}_j = \begin{bmatrix} E_x \\ E_y \end{bmatrix} = \begin{bmatrix} \cos(\psi) \\ \sin(\psi)e^{-i\delta} \end{bmatrix}, \quad (3.9)$$

where  $\psi = \frac{1}{2}\tan^{-1}\left(\frac{\sqrt{S_2^2+S_3^2}}{S_1}\right)$  and  $\delta = \tan^{-1}\left(\frac{S_3}{S_2}\right)$ .

Since each Jones vector has an unknown amplitude and phase, a reconstruction algorithm was constructed as follows: If  $\mathbf{J}$  represents the unknown Jones matrix,  $\hat{\mathbf{e}}_j$  the input vectors,  $\hat{\mathbf{g}}_j$  the output vectors, and if  $\kappa_j$  represents the unknown (complex) amplitudes, then:

$$\kappa_j \hat{\mathbf{g}}_j = \mathbf{J} \hat{\mathbf{e}}_j. \quad (3.10)$$

If the value of  $\kappa_1$  is fixed (this corresponds to the global complex amplitude), the four components of  $\mathbf{J}$  and the remaining  $\kappa_j (j > 1)$  can be solved provided the number of inputs is three or more. The final form can then be represented as,

$$\begin{bmatrix} e_{x1} & e_{y1} & 0 & 0 & 0 & 0 \\ 0 & 0 & e_{x1} & e_{y1} & 0 & 0 \\ e_{x2} & e_{y2} & 0 & 0 & g_{x2} & 0 \\ 0 & 0 & e_{x2} & e_{y2} & g_{y2} & 0 \\ e_{x3} & e_{y3} & 0 & 0 & 0 & g_{x3} \\ 0 & 0 & e_{x3} & e_{y3} & 0 & g_{y3} \end{bmatrix} \cdot \begin{bmatrix} J_{11} \\ J_{12} \\ J_{21} \\ J_{22} \\ \kappa_2 \\ \kappa_3 \end{bmatrix} = \begin{bmatrix} \kappa_1 g_{x1} \\ \kappa_1 g_{y1} \\ 0 \\ 0 \\ 0 \\ 0 \end{bmatrix}, \quad (3.11)$$

where  $e_{xj}(g_{xj})$  is the  $x$  component of the  $j^{\text{th}}$  input (output) vector, and  $J_{kl}$  are the components of  $\mathbf{J}$ . Note that here  $\mathbf{J}$  is the total Jones matrix of the system and the sample. To get the system Jones matrix we simply use,

$$\mathbf{J}_{\text{samp}} = \mathbf{J}_{\text{sys}}^{-1} \cdot \begin{bmatrix} J_{11} & J_{12} \\ J_{21} & J_{22} \end{bmatrix}_{\text{total}}. \quad (3.12)$$

### 3.5 Polarization Properties of Si:Ga Nanowires

Using the sample Jones matrix, we can extract the retardance, orientation of the retardance, and diattenuation of the structure. The retardance,  $\Delta$ , can be calculated by finding the phase difference between the complex eigenvalues of the sample Jones matrix,

$$\Delta = \tan^{-1} \left( \frac{\text{Im}\{\lambda_1 \lambda_2^*\}}{\text{Re}\{\lambda_1 \lambda_2^*\}} \right), \quad (3.13)$$

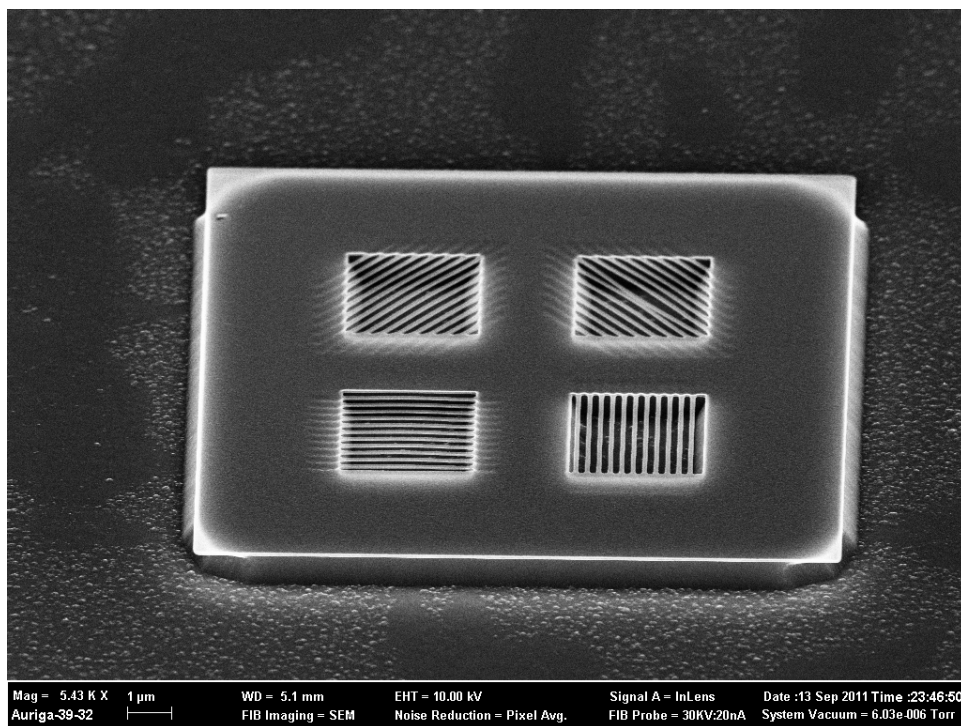
where  $\lambda_1$  and  $\lambda_2$  are the eigenvalues of the sample Jones matrix. The orientation of the retardance can be calculated as described in Born and Wolf[16],

$$\text{orientation} = \begin{cases} \tan^{-1} \left( \frac{v_{1x}}{v_{1y}} \right) & \text{for } \Delta < 0 \\ \tan^{-1} \left( \frac{v_{2x}}{v_{2y}} \right) & \text{for } \Delta > 0 \end{cases} \quad (3.14)$$

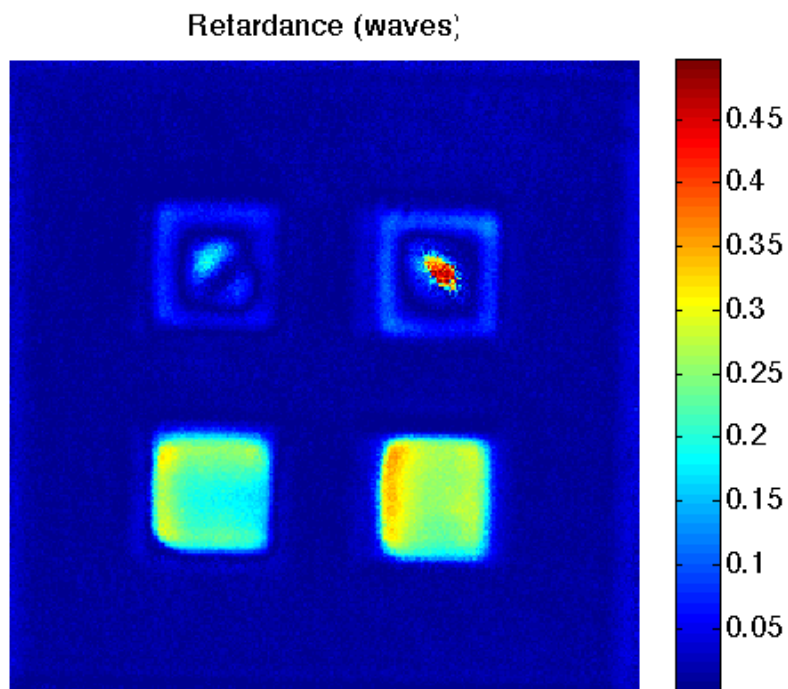
where  $v_1$  and  $v_2$  are eigenvectors of the Jones matrix, and  $x$  and  $y$  subscripts denote the x and y components of the vector. The diattenuation is plotted as a visibility as described by Chipman[65],

$$\text{diattenuation} = \frac{|\lambda_1| - |\lambda_2|}{|\lambda_1| + |\lambda_2|}. \quad (3.15)$$

Figure 3.6 shows a set of nanowires that have a period of 250nm and a thickness of  $\sim 42$ nm. This set of wires has been doped with  $0.1 \frac{\text{nC}}{\mu\text{m}^2}$  of gallium ions. The etch was done with a 60s RIE of 91%Ar and 9%SF<sub>6</sub> at a process pressure of 52mTorr. Following the RIE, a 150s wet etch was done in NaOH at 50C, and then critical point dried. The resulting wires are  $\approx 120$  nm wide, making the grating have just less than 50% duty cycle. The wire gratings are suspended approximately 600nm above the surface (measured with SEM and tilted sample) effectively forms an optical cavity consisting of a substrate reflection, air gap and nanowire array.



(a) SEM micrograph of Si:Ga nanowires tilted at 54 degrees.



(b) Reflective retardance in waves at 532nm.

Figure 3.6: SEM micrograph and retardance of linear nanowires.

The two lower gratings have a fairly uniform retardance of about a fifth to a quarter of a wave, with low (<15%) diattenuation.

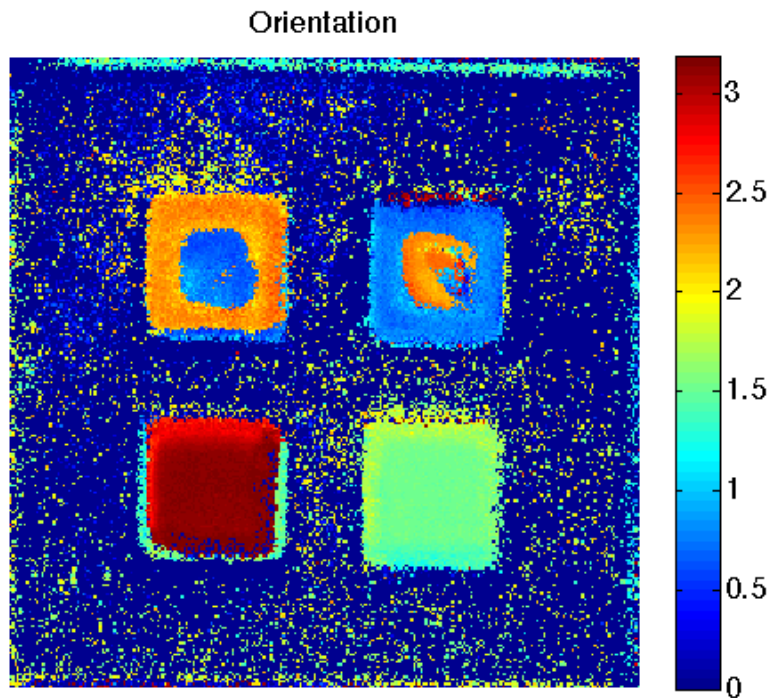
The next sample is a set of concentric circle nanowires. This sample was doped with the same dose, duty cycle and period; this sample went through the same 60s RIE as the previous sample, but the wet etch done on it was done in NaOH at 60C for 150s. This resulted in wires of the same dimension but they are suspended further from the substrate. An effect of a longer etch is that when the NaOH etches along the crystal planes, the angled side wall suppresses most of the substrate reflection. This structure had a much lower retardance (0.1 - 0.15 waves) and a much higher diattenuation (0.5-0.7).

### **3.6 Nanowire Thickness**

To model the nanowires effectively we need to accurately know their dimensions. The lateral dimensions are easy to measure, as they can be measured with an SEM just viewing from above. To measure the wire thickness however it is a little trickier. Looking at the wires at an angle will yield thickness information but it is often difficult to tell exactly where the sidewall ends and the top of the wire starts due to their geometry. To make the measurement easier, we fabricated a suspended ribbon with all of the same parameters we used for the nanowires, as seen in figure 3.10. This made the side of the ribbon much easier to see. From this image, we were able to measure the wire thickness to be about 42 nm.

### **3.7 Rigorous Coupled Wave Analysis**

Using the index of refraction calculated in the previous chapter, an accurate model of the Si:Ga structures can be made using rigorous coupled wave analysis (RCWA). RCWA was introduced in the late 1980's as a way of providing numerical solutions



(a) Orientation of retardance on reflection.

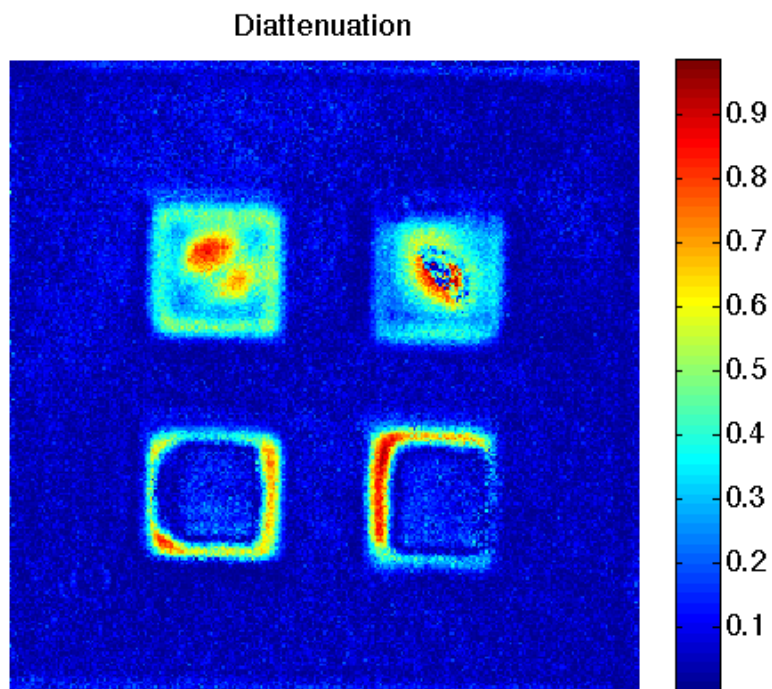
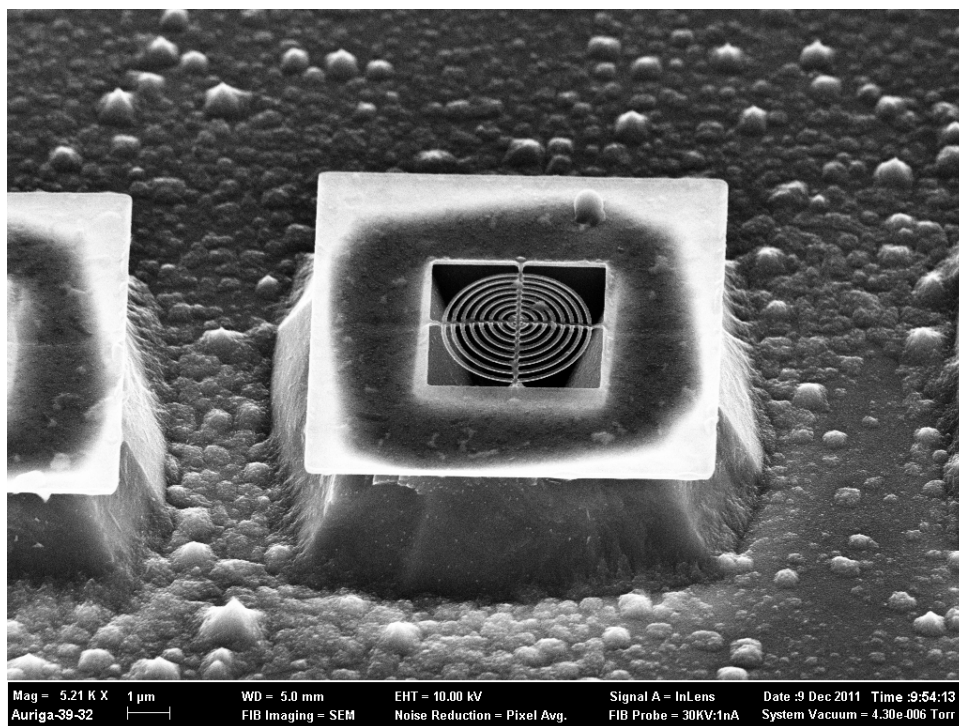
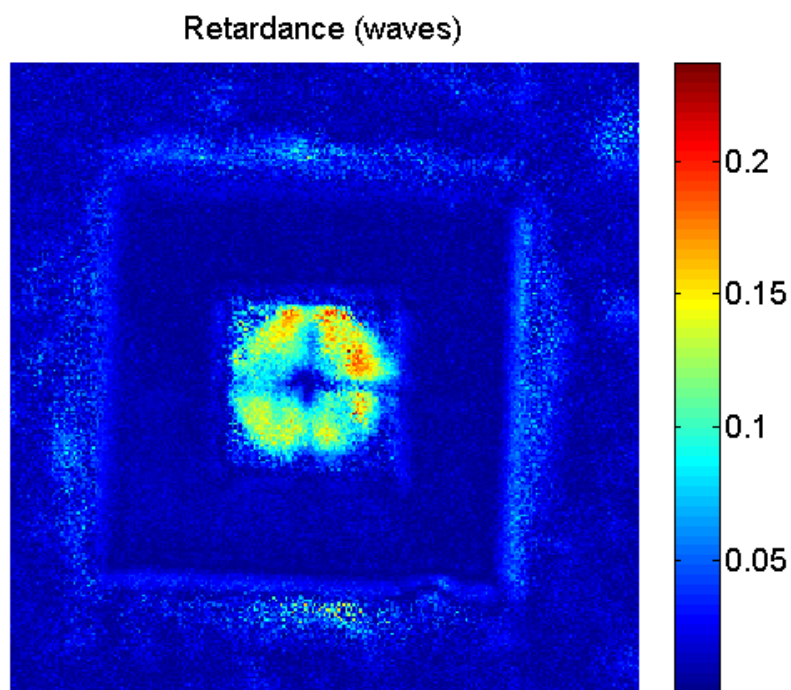
(b) Diattenuation plotted as a visibility,  $\frac{I_{\parallel} - I_{\perp}}{I_{\parallel} + I_{\perp}}$ .

Figure 3.7: Orientation of the retardance and diattenuation of linear nanowires.

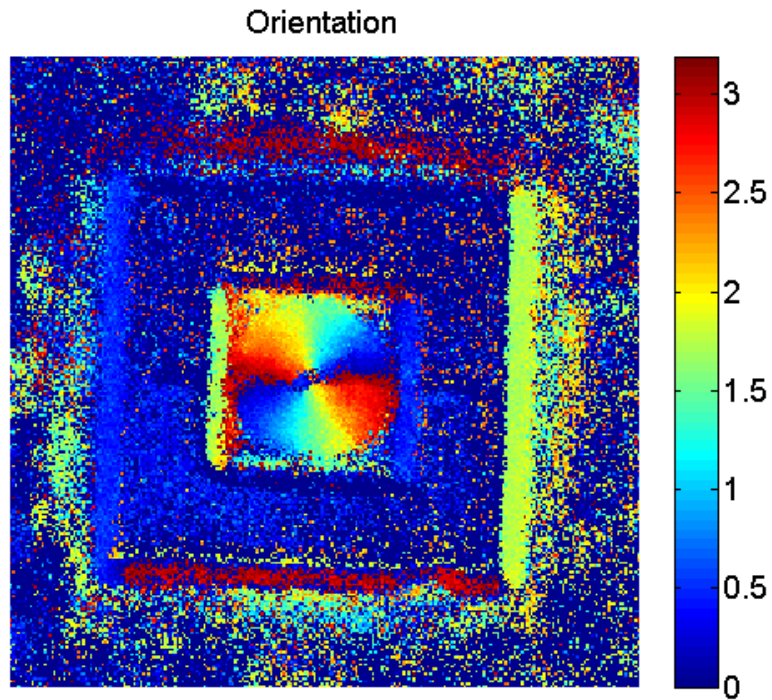


(a) SEM micrograph of Si:Ga nanowires tilted at 54 degrees.



(b) Reflective retardance in waves at 532nm.

Figure 3.8: SEM micrograph and retardance of concentric circle nanowires.



(a) Orientation of retardance on reflection.

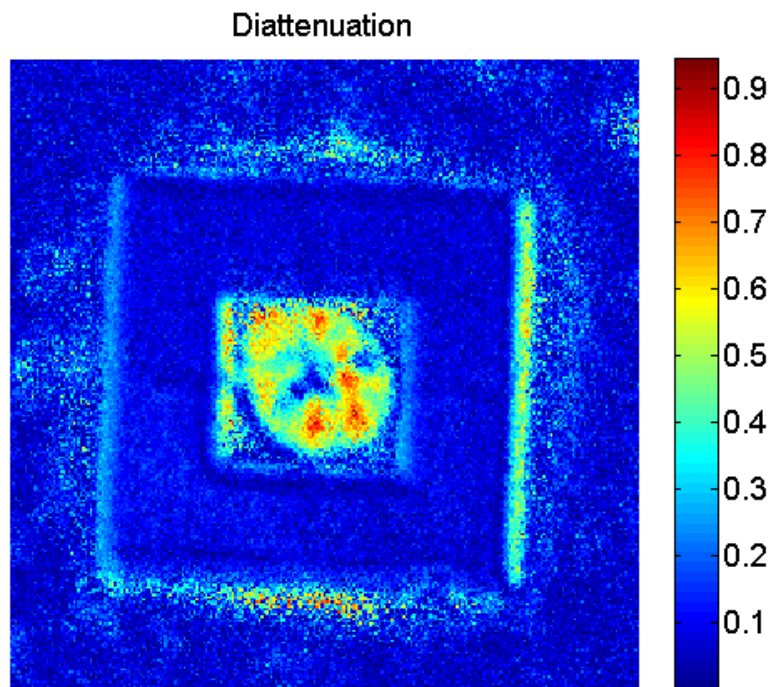
(b) Diattenuation plotted as a visibility,  $\frac{I_{\parallel} - I_{\perp}}{I_{\parallel} + I_{\perp}}$ .

Figure 3.9: Orientation of the retardance and diattenuation of concentric circle nanowires.

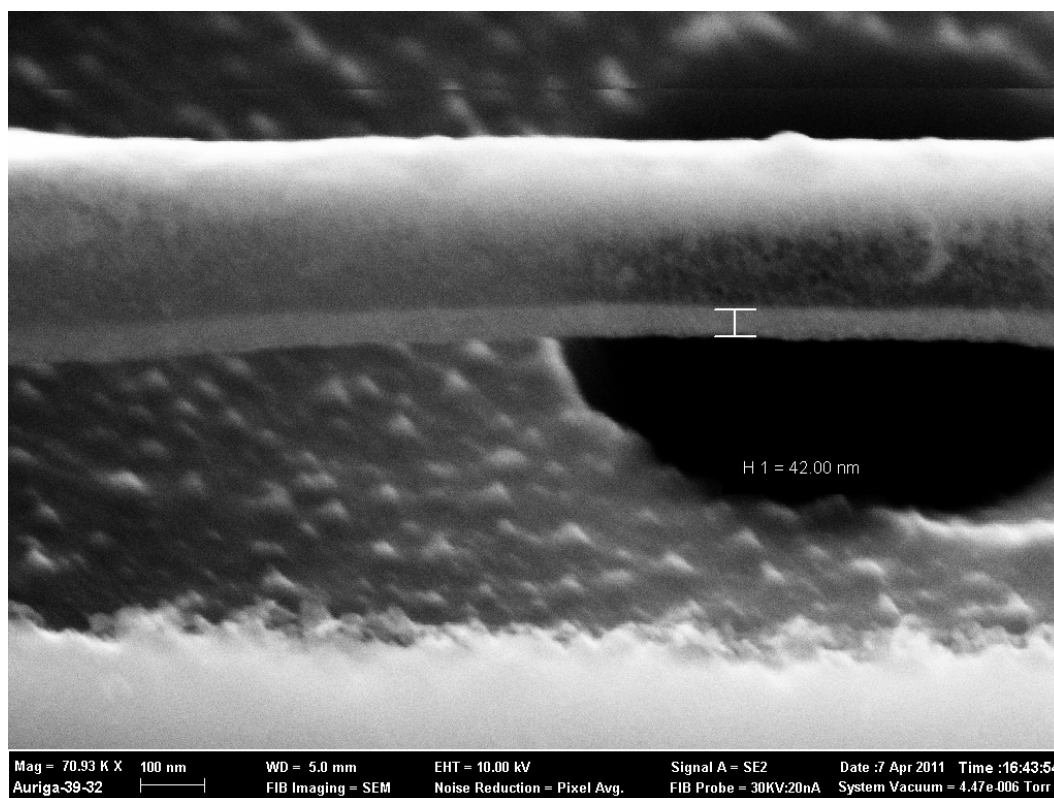


Figure 3.10: SEM micrograph of a Si:Ga nano-ribbon taken at  $54^\circ$  with tilt compensation of  $36^\circ$ .

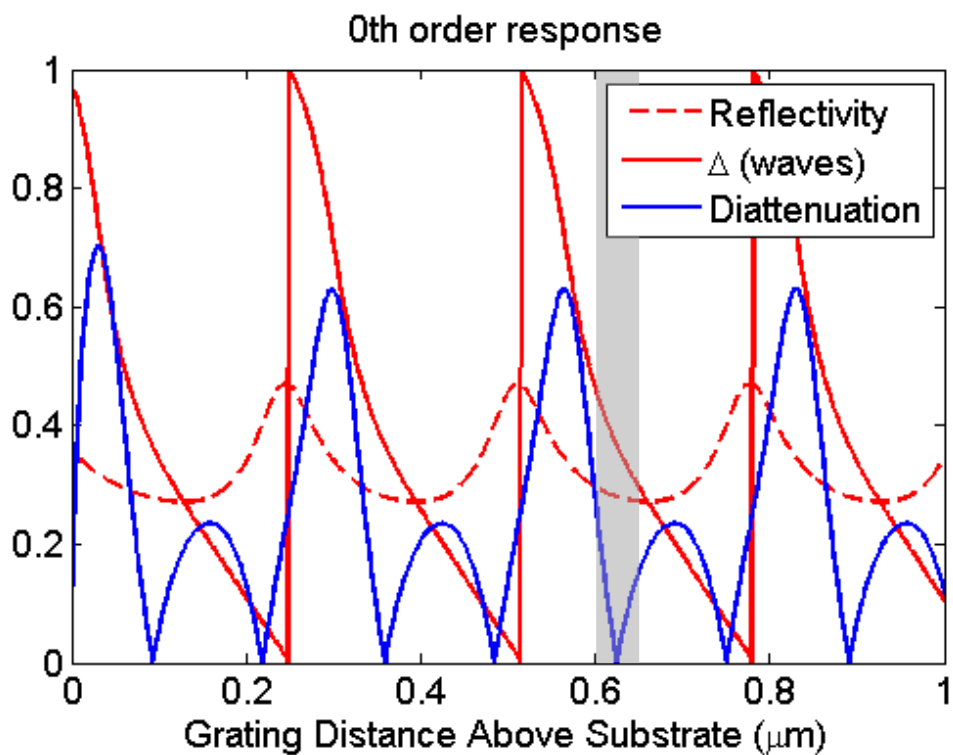
to structures that satisfy periodic boundary conditions in the plane of the layers. One-dimensional grating structures are well suited to this method; the algorithm requires describing the cross section of a grating structure as a series of periodic layers, computing the Fourier representation of the complex refractive index profile in each layer, solving the associated eigenvalue problem in each layer and matching the boundary conditions for either TE (electric field vector parallel to the grating lines) or TM (electric field vector perpendicular to the grating lines). While RCWA is typically used for energy computations (e.g. diffraction efficiency), it provides the complex amplitude reflection and transmission components (in reflection or transmission) necessary to compute the polarimetric response of a grating structure.

A rigorous comparison with theory would require a larger set of samples with varying period; in this discussion, we will limit ourselves to a discussion of the predicted behavior and discuss the implications for further investigations using polarimetric microscopy. Using the parameters of the structure shown in figure 3.6 we can compare the theory to experiment.

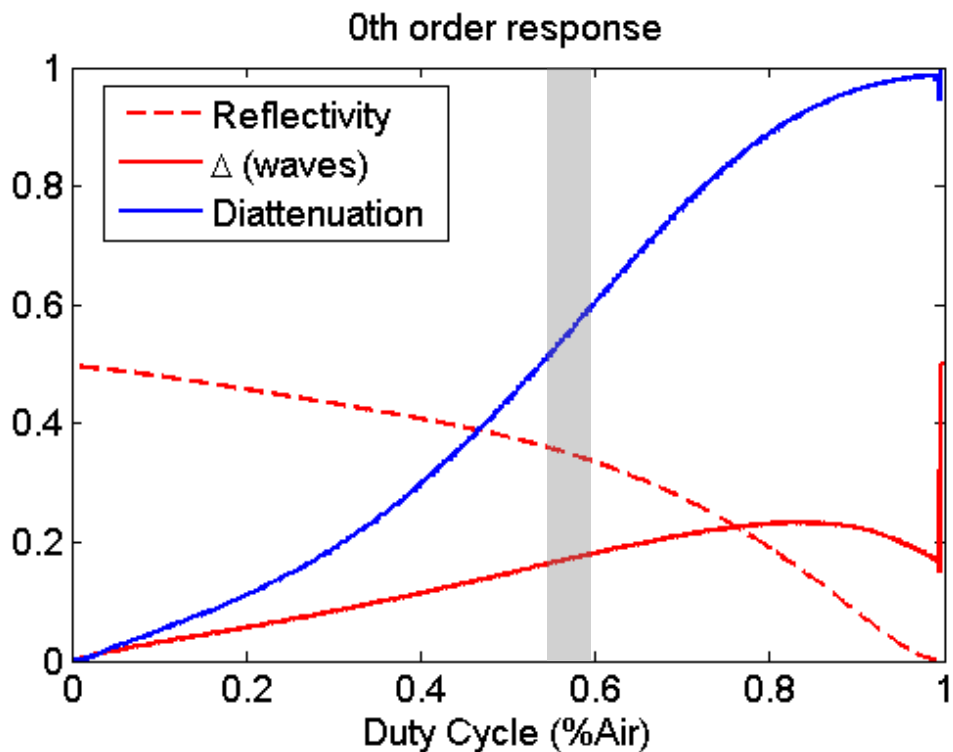
The key results are summary in figure 3.11. The top plot shows the predicted retardance ( $\Delta$ ) and diattenuation as a function of air gap thickness, using other parameters as shown in figure 3.6. The gray region indicates the approximate etch depth as inferred from the electron micrograph. While the diattenuation changes rapidly over the region of interest, the measured retardance of about  $\frac{\lambda}{4}$  is consistent with the measurement.

The sample from figure 3.8 shows little back reflection from the substrate; figure 3.11(b) shows, in this case, the estimated duty cycle of  $\sim 0.58$  is illustrated on the plot of polarimetric response vs. duty cycle for a period of 250nm. Again, the measured response is consistent with the that predicted by RCWA.

We further note that the response is relatively insensitive to the optical constants of the wires. Future work will explore other compositions and composite



(a) RCWA of 250nm period 62.5% duty cycle Si:Ga grating 42nm thick suspended  $x$  above the substrate.



(b) RCWA of 250nm period free standing Si:Ga grating (no substrate reflection). Width of the gray rectangle represents the estimated error.

Figure 3.11: Rigorous coupled wave analysis of Si:Ga nanowire array.

structures that could make use of Si:Ga as a starting structure.

### 3.8 Discussion and Conclusions

It is clear from the experimental images that Si:Ga nanowires are a potentially useful building block in creating sub wavelength structures with a well defined local polarimetric response. When incorporated with a reflective substrate, the structures can provide up to a half-wave retardance on reflection in a manner that is sensitive to the air gap. They can be fabricated in freestanding structures in a variety of shapes, and therefore offer the potential of being incorporated with, e.g. liquid crystal materials, in order to create devices with active polarization control. Since the local anisotropy of the wires produces a space-variant retardance over a very small region, they may be useful for nanoscale polarization control, particularly when integrated with other components on a silicon platform.

For general microscopy, having nanoscale calibration targets of known retardance on reflection is of great general use for polarimetric microscopes that rely on epi-illumination. For biological microscopy, it is intriguing to consider imaging modes in which a specimen is interrogated in double-pass epi-illumination in which the substrate modifies the polarization of the return light.

## Chapter 4

# Spectral Phase Effects in Guided Mode Resonances

### 4.1 Introduction

We now switch from the new gallium implanted silicon structures to structures that are composed of more typical, standard materials. The next three chapters cover the phase effects of guided mode resonances. In this chapter, we investigate the spectral phase properties of a guided mode resonance; this means that we are looking into how the phase of reflected or transmitted light behaves as a function of wavelength of the incident light.

Resonance phenomena are ubiquitous in optics, and are the basis for the design of multilayer filters, the engineering of fiber and waveguide devices, and a wide range of applications that incorporate optical sensing. When a suitably designed waveguide grating couples an external wave to a local wave, a well-known (and well studied) resonance anomaly can appear in the reflectance or transmittance spectrum. With the advent of rigorous electromagnetic approaches to the analysis of periodic and quasi periodic structures [52; 66; 58; 67], it became possible to consider the fabrication of gratings within or near a

slab waveguide such that the grating provides a resonant coupling between an external plane wave incident on the structure and a local (guided) wave. An incident plane wave phase matched to a guided mode will, after some propagation distance in the guide (the so-called coupling length), scatter back into the external wave and interfere. The interference of the coupled/guided mode with the external wave produces a resonance that, for sufficiently long coupling lengths, can produce a subnanometer spectral feature in the reflectance or transmittance of the structure.

The prospect of applying this phenomenon to the design of optical filters and sensors has produced many detailed studies over the last 25 years. Researchers such as Magnusson and coworkers [68; 69; 70], Morris and co-workers[34], and others carried out extensive design, and some experiments. Many of these applied to all-dielectric systems, with a few including semiconductor waveguides. The body of reported experimental work is much smaller, and has focused on the measurement of either reflectance or transmittance, with some attention given to sources of loss, material quality, etc.[39; 40; 71; 33; 72].

In the studies reported so far, little attention has been given to the phase response of guided mode resonances. The phase response can be tremendously important for sensor applications (where the goal is to detect a very small change in refractive index), and in the case of short pulses (for which the dispersion near the resonance can have a significant effect), or nonlinear optics (in which an intensity-dependent refractive index can shift the phase).

In this chapter, we will cover the fabrication, measurement and analysis of a guided mode resonator fabricated on silicon-on-insulator. This guided mode resonator will employ a waveguide, grating coupler, and reflector designed to be illuminated from the substrate. The substrate (silicon) has been designed with an alumina ( $\text{Al}_2\text{O}_3$ ) coating to reduce the native substrate reflectivity from  $\sim 35\%$  to just a few percent. This weak substrate reflection will act as a reference, and

when combined with our light coupled out of the waveguide will cause interference fringes to form. We then use a method similar to Walmsley and Dorrer [73] to recover phase information from this interference in the spectrum.

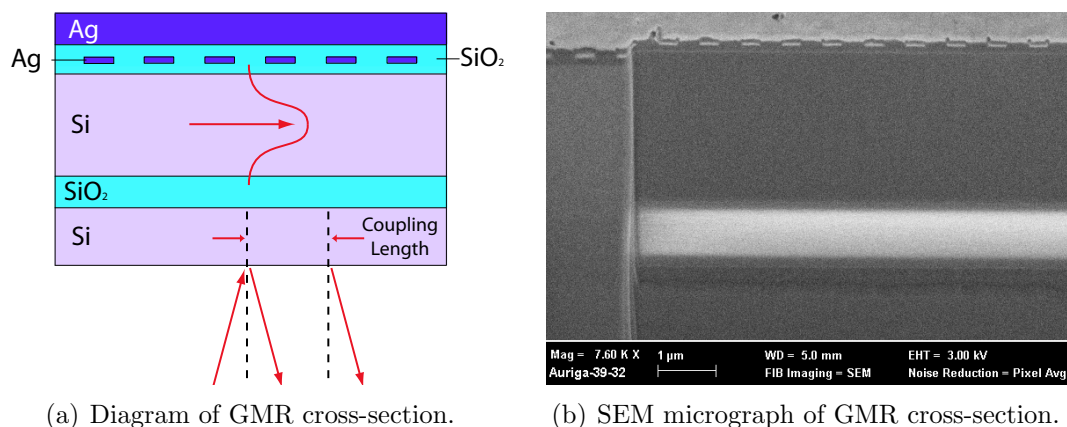
## 4.2 Waveguide Description and Fabrication

The waveguide grating design follows the cross-sectional plan of figure 4.1(a). Light having photon energy less than the band gap of silicon ( $\lambda > 1 \mu\text{m}$ ) is directed to the waveguide through the substrate. A grating layer is separated from the waveguide by a dielectric isolation layer; the isolation layer was placed between the waveguide and the grating to reduce the perturbation to light that propagates in the waveguide. Allowing the light to propagate longer in the waveguide before it couples out will narrow the resonance width [39]. A metal reflector is then separated from the grating by an oxide cap. For spectral regions in which the silicon is nearly transparent, the structure behaves as a high reflector; when the grating period ( $\Lambda$ ), wavelength ( $\lambda$ ) and angle of incidence ( $\theta$ ) satisfy the canonical equation for  $m^{\text{th}}$  order grating coupling

$$\sin \theta + \frac{m\lambda}{\Lambda} = N_{eff}, \quad (4.1)$$

a waveguide coupling resonance appears as a dip in the reflectance spectrum. (All-dielectric structures have typically been designed to have an anti-reflection condition with a reflectance peak at resonance [68].)

The waveguide was fabricated as follows: Beginning with a double side polished SOI wafer that had a buried oxide layer of about  $1.08 \mu\text{m}$  and a silicon device layer of about  $2.41 \mu\text{m}$ , a  $110 \text{ nm}$  silicon dioxide ( $\text{SiO}_2$ ) isolation layer was sputtered on the wafer. On top of the isolation layer, a silver (Ag) grating was fabricated to couple light into the device layer of our wafer. The gratings were  $18 \text{ nm}$  thick



(a) Diagram of GMR cross-section.

(b) SEM micrograph of GMR cross-section.

Figure 4.1: Cross-sectional view of silver GMR structure under test.

linear gratings with periods ranging from 675 nm to 715 nm and a line width of 300 nm. Each grating consisted of  $\sim 725$  lines, which made them  $500 \mu\text{m}$  long and  $30 \mu\text{m}$  in width. A thin (0.5 nm) chromium (Cr) layer was used as an adhesion layer for the silver grating due to problems during liftoff where occasionally the whole grating would lift off. On top of the silver grating, a 95 nm  $\text{SiO}_2$  cap layer was sputtered on, followed by a 125 nm evaporated silver reflecting layer. The native reflection from the substrate is  $\sim 35\%$ , but its impact on the experiment is much higher than that due to the round trip losses incurred because of near band edge absorption in the silicon. As stated earlier, an antireflection coating was put on the substrate, such that the substrate reflection is only a few percent. A cross section of the resulting structure can be seen in figure 4.1(b), and further fabrication details can be seen in appendix D.

### 4.3 Measuring the Optical Response

The rectangular shape of the grating required a line focus in order to maintain a highly collimated condition in the plane of the grating while confining the incident field to within the  $30 \mu\text{m}$  width of the grating. To investigate the amplitude and

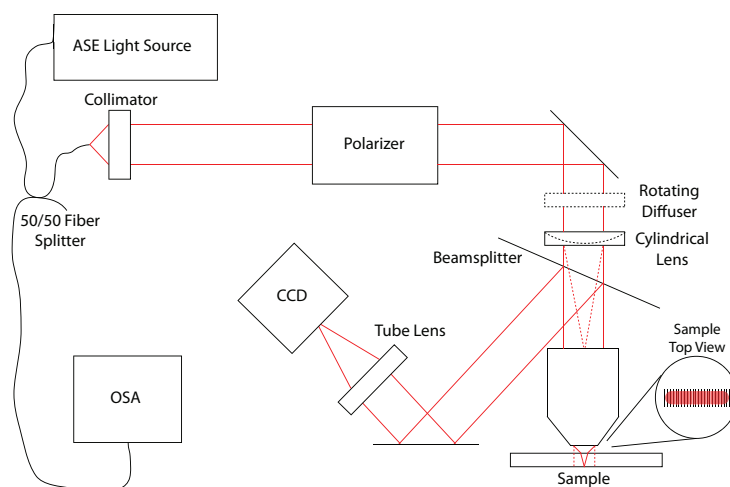


Figure 4.2: Experimental setup. The rotating diffuser is inserted for viewing and alignment. The dashed (solid) line shows the light path in the tangential (sagittal) plane of the cylindrical lens.

phase characteristics of the resonators as a function of wavelength, we set up an apparatus (figure 4.6) to produce a line focus on the sample and analyze the reflected light. The system starts with an amplified spontaneous emission (ASE) light source that is centered at 1050 nm and has a bandwidth of about 60 nm (Amonics ALS-1050). The light is fiber coupled from the source through a 50/50 fiber beam splitter and then collimated in free space, where it is polarized by a Glan-Thompson linear polarizer, which can be set for TE or TM illumination of the sample. To produce the line focus on the sample, the light is focused into the entrance pupil plane of a 5x microscope objective by an air spaced triplet cylindrical lens (used to reduce spherical aberration). To locate and align the resonators, a half-silvered mirror is placed between the cylindrical lens and the microscope objective, which allows the sample to be imaged by using a tube lens and CCD combination as seen in figure 4.6 (a rotating diffuser is inserted into the system only during imaging). Light transmitted through the mirror is then coupled back into the fiber, passes through the 50/50 fiber beam splitter, and is analyzed by our optical spectrum analyzer (OSA).

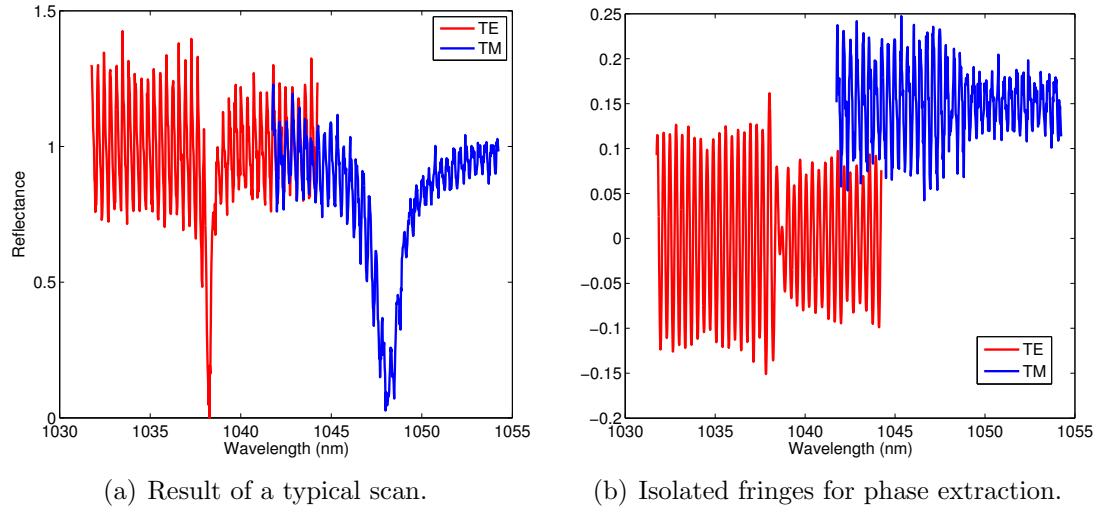


Figure 4.3: Spectrogram used for amplitude and phase analysis. (a) Interference between then normalized reflected signal and the substrate reflection. (b) Fringes after Fourier filtering.

To obtain the phase and amplitude of the reflected light, we take a series of three measurements with the OSA. The first measurement is taken with the line focus on the grating. The second measurement is taken with a block placed between our microscope objective and our sample. This will tell us the spectral response of our system sans device. Finally, a reference scan is taken with the line focus off the grating, on the substrate.

## 4.4 Amplitude and Phase Measurement

To obtain the amplitude information, we take the ratio of sample to substrate after subtracting the background scan from each. The result of a typical scan (corrected for background and normalized by substrate reflection) is shown in figure 4.3(a). It has the form of a spectral interferogram of the form

$$I(\omega) = I_{sample}(\omega) + I_B + 2\sqrt{I_{sample}(\omega)I_B} \cos(\omega\tau_0 + \phi(\omega)), \quad (4.2)$$

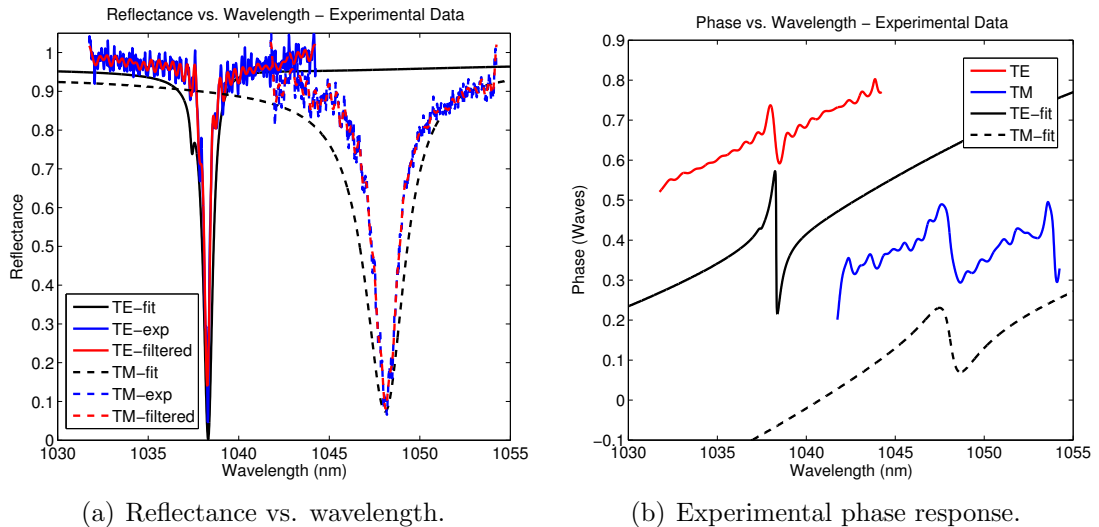


Figure 4.4: Experimental data compared with the RCWA fit for (a) reflection and (b) phase. An arbitrary offset has been added to the phase plots for display.

where  $I_B$  represents the contribution from the AR-coated substrate ( $\sim 1\%$ ),  $\tau_0$  is the round trip time delay through the substrate, and  $\phi(\omega)$  is the spectral phase. Figure 4.3(a) goes above 1 since it is normalized by the substrate reflection.

We deduce the sample reflectance and phase using a Fourier filtering technique similar to that described by Walmsley and Dorrer[73]: Since the high frequency fringe pattern produces a sideband in the Fourier transform, a sequence of FFT, single sideband filtering, inverse FFT and phase extraction are sufficient to deduce  $\phi(\omega)$ .

Figure 4.4(a) shows the reflectance as a function of wavelength of a silver GMR device that has a period of 713 nm, shown in blue. The red curve shows the data after it was Fourier filtered to remove the fringes caused by the interference with the substrate reflection; this filtering caused the minimum to appear shallower than that of the unfiltered data for the TE case. The TE resonance has a baseline reflectance near 96% and has a minimum reflectance of 4.7% at a resonance wavelength of 1038.26 nm. This resonance has a full width at half maximum (FWHM)

of about 0.33 nm. The TM resonance is a bit shallower and considerably wider, with a minimum reflectance of 8.2% at 1048.11 nm and a FWHM of 1.56 nm.

Figure 4.4(b) shows the phase response of the device for the same resonances, where the red and blue lines correspond to TE and TM experimental data respectively. The TE resonance goes through a  $0.15\lambda$  phase shift through resonance, and the TM resonance goes through a  $0.21\lambda$  phase shift.

## 4.5 Discussion

A proper analysis of the phase ideally involves a rigorous model of the complex reflectivity. Rigorous coupled wave analysis (RCWA), a method that was introduced by Moharam and Gaylord[52] divides the structure into layers and employs a Fourier expansion of the dielectric function. With a sufficient number of terms in the Fourier series, the boundary conditions can be satisfied in a way that converges to a rigorous solution. Our numerical approach is that used by Peng and Morris [66], with improvements suggested by Lalanne and Morris[58]. The formulation of the boundary condition is the same as that outlined by Chateau and Hugonin[67].

We apply the theory as follows: The dimensions and refractive index of the materials in the nominal structure are measured independently using reflectance spectroscopy and scanning electron microscopy. However, there can be processing errors that are within the tolerances of either the measurements or the catalog refractive index values. These include small run to run differences in oxide layer, porosity of the deposited metal, and small writing errors that can shift the period of the grating. By measuring devices at several grating periods and adjusting the structure parameters to match the shape of both the TE and TM resonances, we obtain a numerical description of the structure (hereafter referred to as the RCWA fit). An example of the RCWA fit is shown using black (solid for TE,

dashed for TM) lines in figure 4.4. The TE measured reflectance matches well with the RCWA in both depth and resonance width. The TM resonance shows good agreement with the depth of the resonance but the width of the measured resonance is approximately 40% narrower than the theory predicts. The phase shift of the TM resonance agrees with the theory very well, but the TE resonance shows a smaller phase swing than predicted. One possible explanation for this is that the spectral width of the resonance is very close to the fundamental fringe period; as a result, Fourier filtering can have the effect of reducing the maximum measurable phase slope, as can be seen in figure 4.4(b).

For applications requiring a very narrow resonance and rapid phase swing, manufacturing tolerances can be very tight. When optimized, the TE resonance of this structure shows a large ( $\sim 1$  wave) phase swing (figure 4.5(a)) that coincides with a design constraint that drives the minimum reflectance as close as possible to zero at resonance. Any error that raises the minimum reflectance also reduces the phase swing. When an RCWA fit of our fabricated structure is compared to the target design, it is clear that the phase swing has been considerably reduced.

One of the primary sources of error in the fabricated structure is the liftoff process in the silver grating fabrication. Even with a brief sonication following the acetone bath, all of the extraneous silver could not be removed from the grating. This happens because during the evaporation process, some of the silver ends up depositing on the PMMA side walls. On occasion, this will cause some of the grating lines to look like an 'L' or a 'U' in cross-section depending if one or two side walls stuck to the grating line after lift off; this effect can be seen in figure 4.1(b). Even if the liftoff went perfectly and none of the silver from the sidewalls remained on the grating, the surface and edge roughness of the lines will invariably scatter some light in the structure. Both of these effects may cause some light to be reflected even when at resonance, thus pulling our reflection up above the ideal zero reflection.

One measure of a resonator that is useful to consider is to look at its quality factor,

$$Q = \frac{\lambda}{\Delta\lambda}, \quad (4.3)$$

where  $\lambda$  is the resonant wavelength and  $\Delta\lambda$  is the full width at half max of the resonance. The quality factor can also be view as the total energy stored in the resonator divided by the energy loss in one optical cycle. If we look at the experimental data of the TE resonance in figure 4.4(a), we get a quality factor of about 3,400, which compares favorably with other guided mode resonance filters.

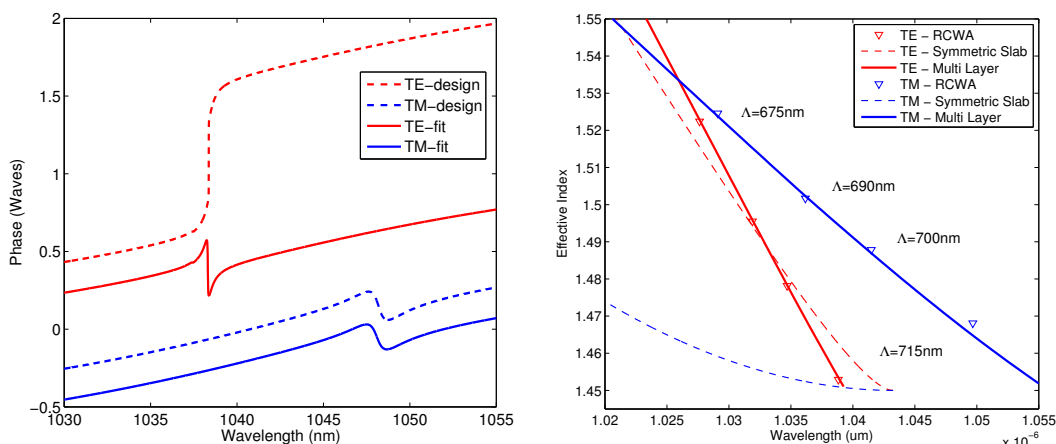
In 2006, Jason Neiser fabricated silicon based guided mode resonance filters for use at 1558 nm, which had a theoretical quality factor of  $\sim 1.4 \times 10^4$ , and fabricated devices had a maximum quality factor of 2,257 [40].

Matthew Borselli investigated silicon microdisk resonators fabricated from silicon-on-insulator wafers side coupled to a waveguide for use around 1500 nm, and demonstrated quality factors around  $3 \times 10^6$  [74], but only had a transmission minimum of  $\sim 88\%$ .

Dharanipathy, Minkov, Tonin, Savona and Houdré investigated high quality factor photonic crystal based resonators that had theoretical quality factors of  $1.7 \times 10^6$ , and demonstrated fabricated resonators that had quality factors up to  $4 \times 10^5$  [75].

All of these cases investigated resonators designed for use between 1500 and 1600 nm where silicon is very transparent. The resonators investigated in this thesis have all be designed for use near 1  $\mu\text{m}$ , which is near the band edge of silicon. This will increase the loss of the resonators considerably; even so we were able to fabricate very deep resonances with quality factors up to around 3000.

We can compare the RCWA calculation with a slab waveguide model in order to estimate the effective index and order of the modes being excited. To do this, we compared two slab models: 1) A simple symmetric slab, which neglects



(a) Phase as a function of wavelength for the RCWA fit (solid lines) of our fabricated structure vs. RCWA for perfect structure (dashed lines).

(b) Comparison of two slab models (dashed lines - simple symmetric slab waveguide and solid lines - multi layer mode solver) and RCWA (triangles - for a couple of grating periods) of the effective index of the waveguide mode vs. position of resonance.

Figure 4.5: Comparison of the RCWA fit with several models. Left: RCWA fit compared with the design target; Right: RCWA fit compared with two different slab waveguide models

the interaction of the evanescent waves with the grating and back reflector; 2) A metal/dielectric stack in which the waveguide modes can be located by computing the attenuated total reflection minima for plane waves incident inside the silicon substrate. For the latter, we employ an effective index model for the grating in order to approximate the difference in grating response between TE and TM modes. While the symmetric slab model is accurate for low order (highly confined) modes, those near cutoff are better modeled using the more complete metal/dielectric stack. Figure 4.5(b) shows how the two slab models (dashed and solid lines) compare to that of the RCWA (triangles) for a few periods. Using equation 4.1, we are able to solve for the effective index of the mode we couple into for both TE and TM illumination. The TE resonance has an effective index of 1.456, and the TM resonance is 1.47. This agrees very well with the values plotted in figure 4.5(b). A reconstruction of the field using the metal/dielectric stack

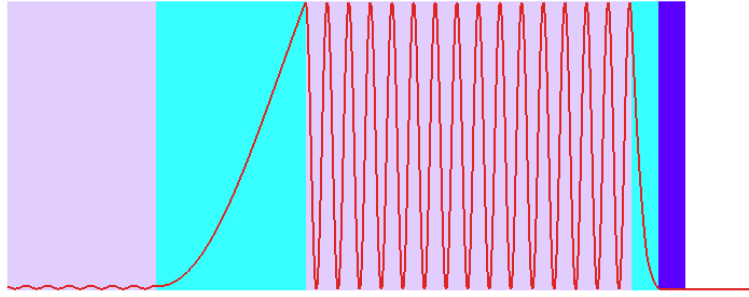


Figure 4.6: Electric field reconstruction of the TE mode of our sample using the multi-layer mode solver. The TE resonance of our structure uses first order grating coupling into the 15<sup>th</sup> order waveguide mode.

calculation allows us to display the approximate field profile for the TE mode, verifying that the resonance is tuned to a high order mode that is very close to a cutoff condition. Any mode with effective index lower than the refractive index of SiO<sub>2</sub> (1.449 for  $\lambda = 1064$  nm) would not be bound to the waveguide.

While this represents the first (to our knowledge) direct measurements of the phase response of guided mode resonances, it is also an innovative geometry in which to consider designing GMR based devices for sensing or other photonic applications. Schmid *et al.* [76] showed a GMR based sensor using a substrate illumination scheme similar to that presented here, albeit one having somewhat larger (and asymmetric) line width. We have found, in our exploration of various design approaches, that the high reflection configuration described here could have some advantages. While it may be surprising that the incorporation of metal near a waveguide does not heavily damp the resonance, the field profile shows that the guided mode field strength is comparatively weak at the metal grating.

## 4.6 Conclusion

In summary, we have presented and tested a method by which one may directly characterize the phase response of a guided mode resonance such as may be used

in a variety of different applications. By fitting the details of the device structure to an RCWA model, we are able to replicate the resonance positions and depth for both the TE and TM resonances. The phase of the TM resonance shows good comparison with theory, while the measured phase of the TE resonance appears to be limited by the resolution of the phase recovery algorithm we have used.

## Chapter 5

# Angular Phase Effects in Guided Mode Resonances

### 5.1 Introduction

In the previous chapter, we investigated the spectral phase response of guided mode resonances. This chapter, we'll look into the *angular* phase response. To do this, we will look at a slightly different style of guided mode resonator. The previous structure used the silicon device layer or a silicon-on-insulator wafer to guide light. In this chapter, we will investigate resonances created with the interaction of specularly reflected light, and light that has been grating coupled into a surface plasmon polariton.

The study of grating-mediated SPP excitation has a long and rich history in optics[22; 23; 24; 25; 26; 27; 28; 29] – many of these studies have devoted close attention (both in theory and experiment) to such details as coupling conditions, grating shape, and spectral response. A few papers have given special attention to the response of the SPP-grating combination over the angular spectrum. For example, a 1978 study published by Kretschman [77] showed clearly how the two dimensional angular response of a SPP excited by attenuated total reflection could

be photographed in the far field. (He further showed how, if such a film was corrugated, the shadowgram of a TM-illuminated sample would project the dispersion relation of the guided wave/grating combination.) Hooper and Sambles [78] and Hibbins, Sambles and Lawrence [79] studied the azimuthal dependence of grating coupled SPP excitations. Elston, Bryan-Brown and Sambles [80] showed how an SPP resonance could accomplish polarization conversion. When applied to more generalized nano-structured materials, these resonances can give rise to extreme anomalous dispersion and can be used as the basis for a variety of metamaterials. Of particular note is the study published by Constant *et al.* [81], which mapped the 2D reflectivity of a SPP resonance as a function of wavelength.

The grating-coupled surface plasmon polariton is among the most basic of the various SPP related interactions. In this paper, we describe an experimental study and analysis of the phase response over the (TM polarized) angular spectrum of a guided mode resonance such as occurs in SPP excitation. To do so, we employ a focused beam geometry similar to [81] but using the pupil fields of a microscope objective to create an incident angular spectrum that can then be resolved by imaging the reflected pupil fields. We then illuminate the sample with a mixture of TE and TM light using the TE reflected light as a reference beam, and combine a Wollaston prism with a calcite beam displacer and linear analyzer to create an interferogram that can be processed to extract the phase response over a two dimensional angular spectrum. In the following sections of this chapter, we describe the sample preparation, a two dimensional pupil analysis of the coupling using rigorous coupled wave analysis (RCWA), and a description and analysis of the experimental results for a silver grating having a rectangular profile.

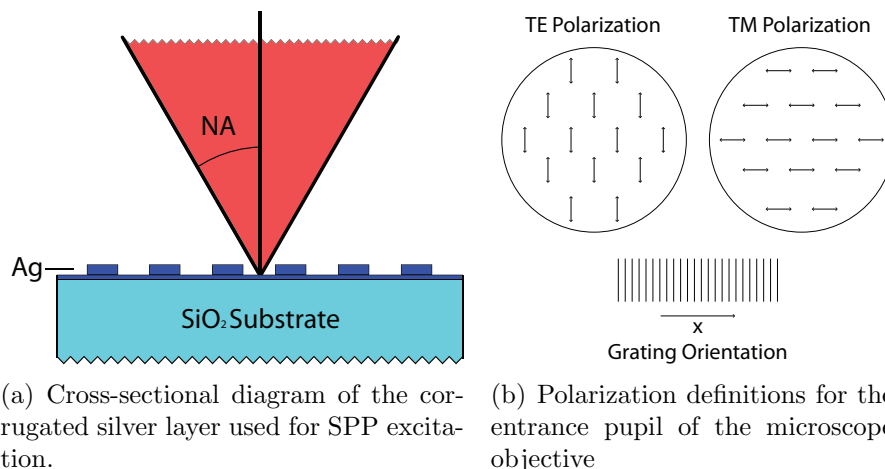


Figure 5.1: Illustrations showing the grating geometry and orientation with respect to the illumination of the microscope entrance pupil.

## 5.2 Sample Description and Fabrication

The test structure consists of a corrugated silver layer on a fused silica substrate as shown in figure 5.1(a). In order to independently control the silver thickness and the grating depth, the test structures were fabricated by first applying a blanket coat of silver and then using a lithography/lift-off procedure to create the corrugation. The fabrication proceeded as follows: A 22 nm silver layer was evaporated on a 500  $\mu\text{m}$  thick fused silica wafer. Electron beam lithography was then used to pattern a grating in a layer of polymethyl methacrylate (MicroChem 495K 4% PMMA in chlorobenzene) that was spin coated onto the wafer. Several  $30\mu\text{m} \times 500\mu\text{m}$  gratings were exposed in the PMMA, each with slightly different periods (950 – 1050 nm). Following the patterning, 58 nm of silver was evaporated onto the PMMA grating. The sample was then soaked in acetone to dissolve the PMMA grating to leave only the deposited silver grating. To clean up the edges and dislodge any remaining silver that was on the sidewall of the PMMA, the sample was sonicated in acetone briefly (<10 seconds), and then rinsed in alcohol.

### 5.3 Measuring the Optical Response

We consider the usual conical mounting arrangement, in which a monochromatic beam (wavelength  $\lambda$ ) is incident on a corrugated metal surface (grating period ( $\Lambda$ ), aligned to the  $y$  axis) from a direction  $\hat{\alpha}$ . If  $\hat{\alpha}_{sp}$  denotes the (in-plane) direction vector of the surface plasmon, the incident wave will phase match to an SPP provided that

$$\alpha_x + \frac{m\lambda}{\Lambda} = \text{Re}\{\beta\}\alpha_{spx}, \quad (5.1)$$

$$\alpha_y = \text{Re}\{\beta\}\alpha_{spx}, \quad (5.2)$$

where  $\beta$  represents the normalized (complex) propagation constant of the SPP and we assume  $m^{\text{th}}$  order grating coupling. We consider wavelengths well away from the plasma resonance of silver (in our case,  $\lambda = 1064$  nm) and excite the SPP on the air side of the silver film. Throughout this paper, when the terms TE or TM polarization are used, they are used in reference to the orientation of the grating, as seen in figure 5.1(b). TE illumination will always be vertically polarized in the entrance pupil of our objective, likewise TM light will be horizontally polarized throughout the pupil.

A well-corrected microscope objective has the effect of transforming a collimated incident beam to a converging spherical wave that may be represented as an ensemble of plane waves over the numerical aperture. When focused on a grating, the effect is to simultaneously illuminate the sample with the entire plane wave ensemble. To measure the amplitude and phase response we therefore set up an optical system to image the light reflected into the exit pupil plane of a microscope objective after focusing light onto our sample. The system begins with a fiber coupled Nd:YAG laser (Amoco Laser) at 1064 nm, that is then collimated in free space. The light is polarized with a Glan-Thompson linear polarizer that is typically set at  $45^\circ$ , passes through a beamsplitter, and is then focused on

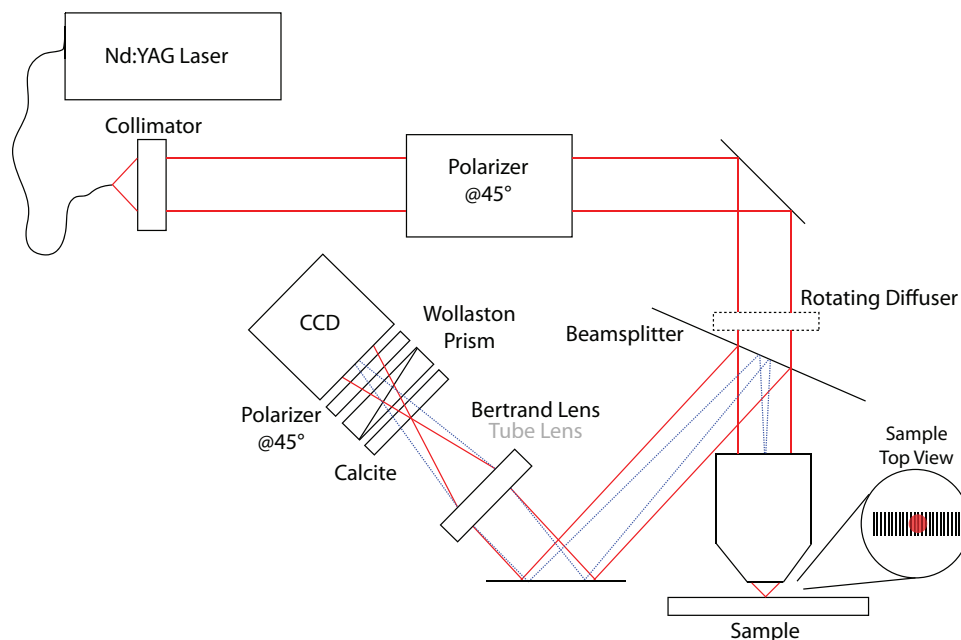


Figure 5.2: Experimental setup with lens set to the Bertrand configuration. The rotating diffuser is inserted for viewing and alignment.

our sample with a 20x (0.4NA) microscope objective. The light is reflected by the sample, collected by the microscope objective, reflected by the beamsplitter and passes through a lens that can be set either to image the sample (tube lens configuration) or the pupil plane of the objective (Bertrand lens configuration, as shown in figure 5.2). To get the phase information, a Wollaston prism was placed after the lens to shear TE polarization with respect to TM. This shear causes the two beams to walk off from each other; to accommodate this, a calcite crystal was inserted in the system before the prism. The calcite is oriented such that TE and TM light will be displaced from each other but are still parallel exiting the crystal. This displacement in combination with the prism induced shear will make the two beams overlap in the CCD plane, as seen in figure 5.3. A  $45^\circ$  linear analyzer is placed after the prism, just before the CCD, to create interference between the TE (reference) and TM (SPP) beams. One point of note is that the calcite imparts an optical path difference between the two polarizations that can

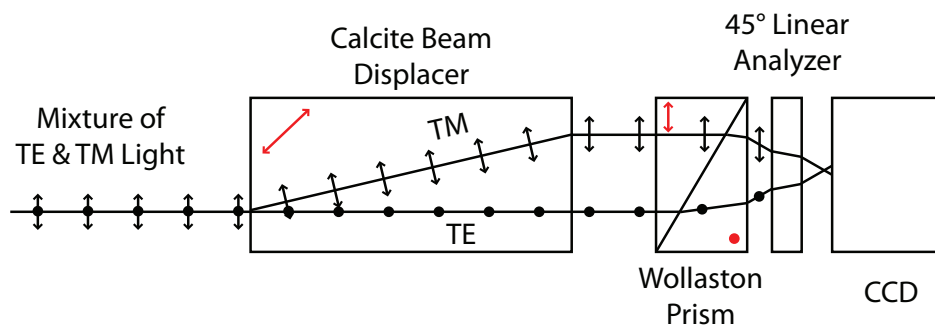
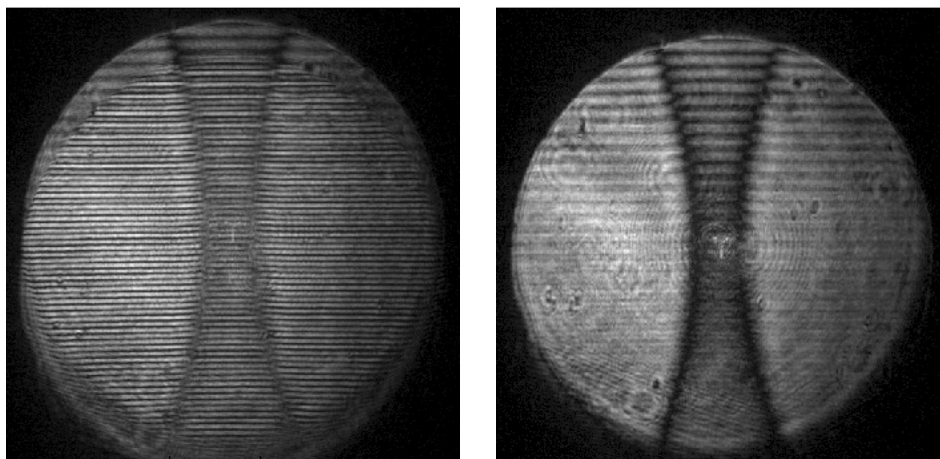


Figure 5.3: Calcite, Wollaston prism and analyzer combination used to interfere TE and TM polarization. Calcite optical axes are displayed in red. The incident beam is a mixture of TE and TM light and ends polarized at  $45^\circ$  due to the analyzer.

be close to a millimeter (depending on the thickness of calcite); this can cause a reduction in fringe visibility for sources that have low temporal coherence. For this reason, and also to accurately measure the sharpness of the phase response, we chose a monochromatic source.

Before data is taken, the imaging lens is placed in its tube lens configuration and the rotating diffuser is inserted in front of the beamsplitter. This allows the grating structure to be viewed directly to align the focal spot. To take data, the diffuser is removed, and the lens is placed in the Bertrand configuration. An image is then taken to record the interference between the TE and TM polarization. A second image is taken with the input polarizer and the analyzer set to allow TM polarization to pass; this image will give us the TM polarized reflectance of the sample. Background images were taken in both configurations with the focal spot placed away from the grating.

An example interference pattern generated by the system for a sample having a grating period of 981 nm is shown in figure 5.4(a). To fix the issue of non-uniform illumination seen in figure 5.4, the images were normalized using the background images that were taken. Figure 5.4(b) shows the raw non-normalized and unfiltered TM reflectance of the same structure.



(a) Square root of the intensity of the interference between TE (reference) and TM (SPP) beams. (b) Square root of the TM reflectance of structure. The horizontal fringes were induced by the beamsplitter.

Figure 5.4: Raw data taken of a structure with 981 nm corrugated silver grating. Multiple reflections off surfaces of the microscope objective can be seen in the center of the field, along with scatter from other contaminants throughout the field. The square root of the measured intensity is plotted to make the edge of the pupil more visible; it also reduces the appearance of the non uniform illumination.

To obtain the phase information from the interference fringes, a 2D Fourier transform is done and a window is applied to isolate the carrier fringe information. The phase of the inverse Fourier transform is then calculated, removing tilt and unwrapping  $2\pi$  phase jumps. Phase data taken with the setup for a corrugated silver film is shown in figures 5.5(a) and 5.6(a) for grating periods of 981 nm and 956 nm respectively. The almond shape to the figures occurs since we can only obtain phase information in the overlap region of the TE and TM circular pupils. Figures 5.7(a) and 5.8(a) show the measured reflectance of the structure with just TM light incident on the sample, after Fourier filtering out fringes that were induced by our beamsplitter.

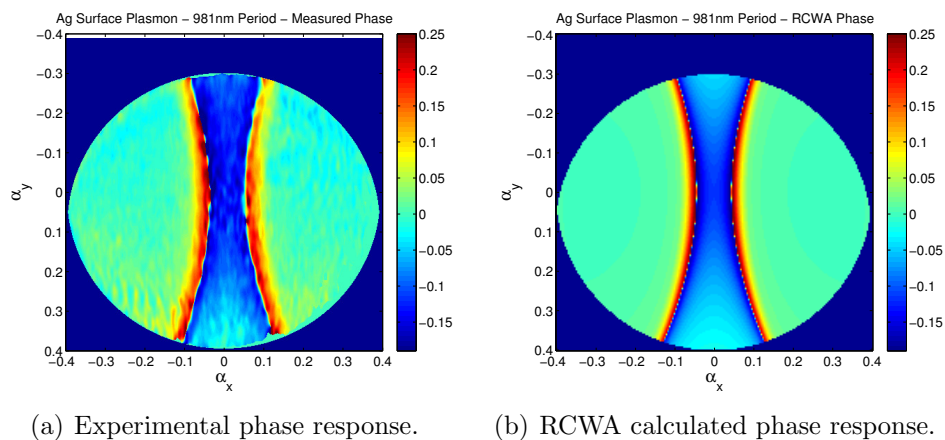


Figure 5.5: Experimental and theoretical phase response (in waves) of a 981 nm period corrugated silver layer on fused silica.

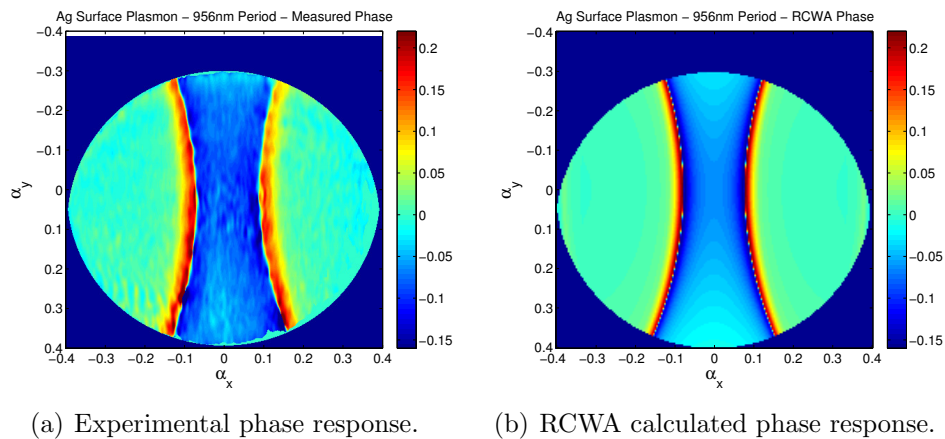


Figure 5.6: Experimental and theoretical phase response (in waves) of a 956 nm period corrugated silver layer on fused silica.

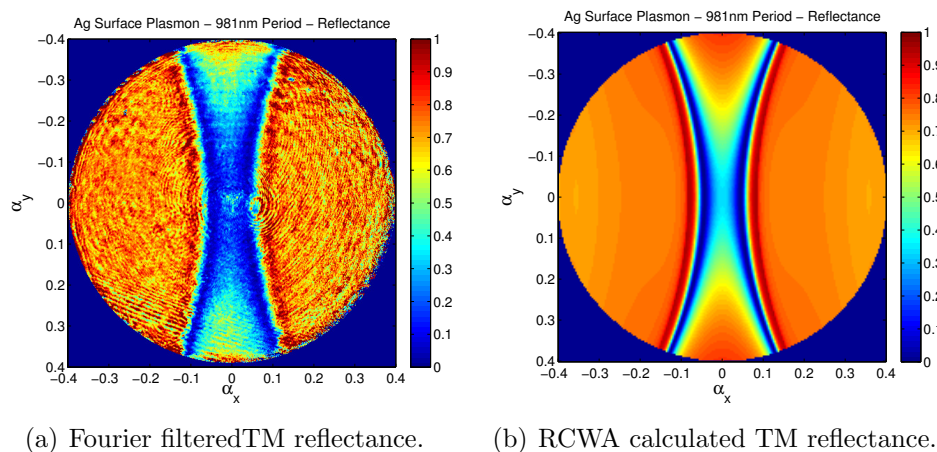


Figure 5.7: Experimental and theoretical reflectance of a 981 nm period corrugated silver layer on fused silica.

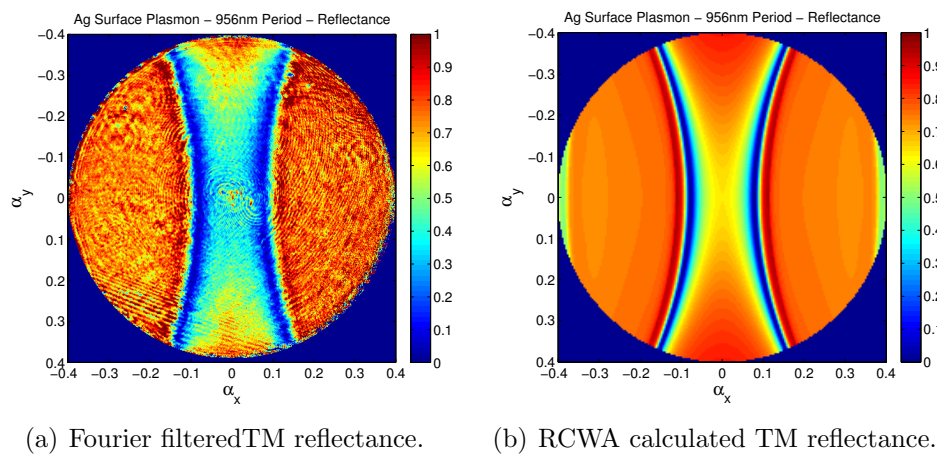


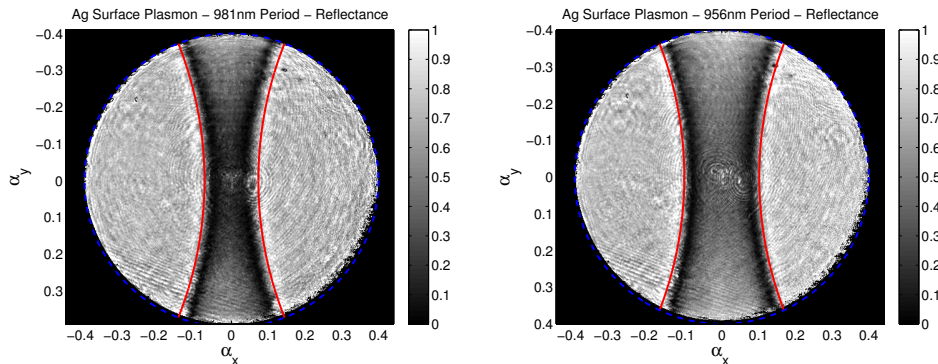
Figure 5.8: Experimental and theoretical reflectance of a 956 nm period corrugated silver layer on fused silica.

## 5.4 Discussion of Results

To verify that we are exciting a mode that closely corresponds to the single interface (Ag-Air) SPP, we can take a simplified slab model, in which the normalized complex propagation constant is given by  $\beta = \sqrt{\varepsilon_{Ag}/(1 + \varepsilon_{Ag})}$ [82]. Combining equations 5.1 and 5.2 by summing the squares gives the conical coupling condition

$$\left(\alpha_x + \frac{m\lambda}{\Lambda}\right)^2 + \alpha_y^2 = \text{Re}\{\beta\}^2. \quad (5.3)$$

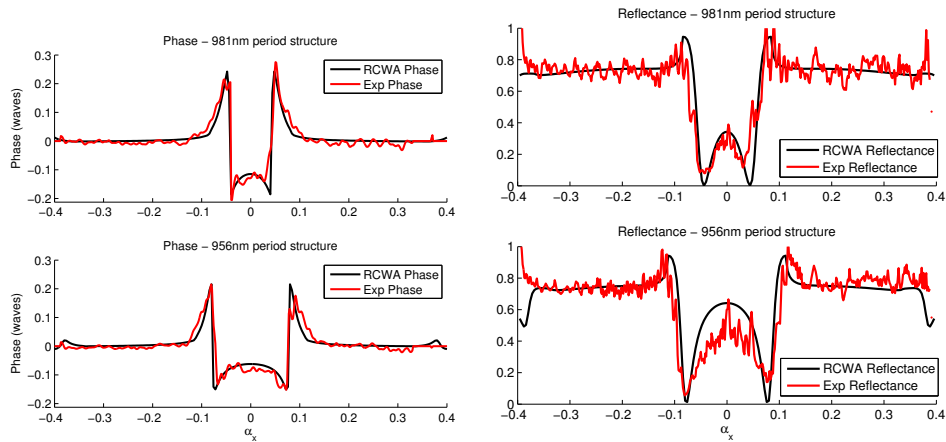
Figure 5.9 shows the map of pupil reflectance superimposed with contours representing the solutions of equation 5.3. The reflectance minima are shifted slightly with respect to the ideal slab, reflecting the usual shifts associated with the asymmetry in the spectrum of grating coupled SPPs. The shape and position of the coupling resonance confirms  $m = +1$  coupling into the backward propagating (left) SPP mode and  $m = -1$  coupling into the forward propagating (right) SPP mode.



(a) Figure 5.7(a) overlaid with the solutions for the backward and forward propagating SPP resonances for  $\Lambda = 981$  nm.

(b) Figure 5.8(a) overlaid with the solutions for the backward and forward propagating SPP resonances for  $\Lambda = 956$  nm.

Figure 5.9: Microscope pupil images overlaid with the solution to equation 5.3 given that  $\varepsilon_{Ag} = -46 - 3.36i$  for a wavelength of  $\lambda = 1064$  nm.



(a) Slice through the phase plots (top: figure 5.5; bottom: figure 5.6) for  $\alpha_y = 0$ .  
 (b) Slice through the reflectance plots for  $\alpha_y = 0$ . An average was calculated for slices with  $\alpha_y = 0 \pm 0.034$  for top: figure 5.7 and bottom: figure 5.8.

Figure 5.10: Slices through the phase and reflectance plots for both experiment and RCWA for analysis.

To provide a more rigorous model of both the reflectance and the phase response of the structures, we again employed RCWA. Care was taken to ensure that the RCWA calculation was converging; all of the RCWA simulations shown in this paper used 41 orders in the calculation. We model the focused beam as a superposition of plane waves that are incident on the sample at angles bounded by the numerical aperture of our microscope objective. Due to symmetry of the structure and the illumination, we were able to calculate the response of only one quadrant of the pupil ( $0 \leq \alpha_x, \alpha_y \leq 0.4$ ) and mirror the data to get the other three quadrants. We used  $101 \times 101$  plane waves (points in our pupil) to model the quadrant of our focused beam. A mask was applied to the plots, after mirroring, to only show the RCWA data that corresponded to the data that we were able to measure with the experiment. Figures 5.5(b) and 5.6(b) show the phase and figures 5.7(b) and 5.8(b) show the reflectance of the two structures as calculated using RCWA.

Figure 5.10 shows cross sections through  $\alpha_y = 0$  for figures 5.5-5.8. For  $\alpha_y = 0$ ,

the average measured phase swing of the forward and backward propagating SPP resonances is 0.42 waves for the 981 nm period and 0.34 waves for the 956 nm period structure. This compares extremely well with the phase swing calculated using RCWA, which is 0.43 waves and 0.37 waves respectively. While the diffraction edge (reflectance peak just beyond the SPP) is easily visible in reflectance, its impact on the phase appears negligible compared to that of the SPP. The RCWA model shows that the average of the absolute value of the maximum phase slope for the SPP is about 90 waves per radian for both structures.

Electron beam lithography produces gratings that tend toward a rectangular shape. The cross section of the grating is known to have a significant impact. Some studies have been made with rectangular gratings that have been reactive ion etched into a uniform metal film such as López-Rios *et al.* [83]. This technique tends to leave a sidewall that is undercut and that (for deep gratings) can sometimes lead to a scalloped sidewall. A lift off process provides a vertical sidewall at the risk of a larger amount of surface roughness. The sensitivity to shape and roughness can find useful applications in nanoscale metrology. For example, Hibbins *et al.* [79] were able to infer what their grating shape was by taking 2D reflectance data. A mixed polarization experiment that includes the phase could extend these capabilities and find applications in semiconductor metrology.

Guided mode resonances – especially those associated with SPP excitation – have received a great deal of attention in recent years due to anticipated applications in various types of optical sensing [84]. Such a sensor generally includes a mechanism by which a resonance will shift (or otherwise change) in response to a change in the optical environment (e.g. from pathogens placed in close proximity to the sensor). We believe that a better understanding of the details of the phase response of these resonances could improve the sensitivity of a sensor. In particular, the rapid phase changes observed in these measurements could open up opportunity for phase sensitive measurements in chemical or pathogen detection.

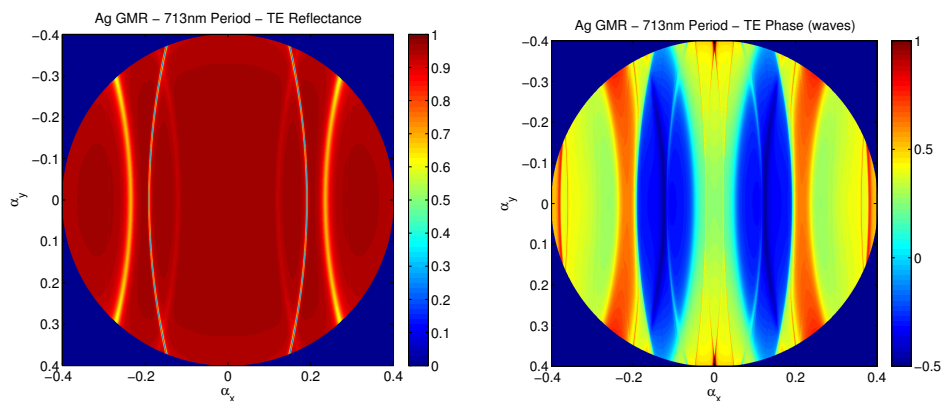
This investigation has been directed to the measurement of the simplest type of SPP excitation – a corrugation on a planar surface. However, localized plasmon resonances show similar characteristics, both in angular spectrum as well as in ordinary spectroscopy [85]; nano-engineered metal structures have been vigorously investigated for sensing applications as well[86]. We suspect that a closer investigation of the phase of localized resonances could yield fruitful and interesting results. The particular method described here makes use of orthogonal polarizations for test and reference beams. It is simplified by the fact that a one dimensional corrugated metal surface has a weak and slowly varying influence on the phase of the TE component, allowing a perfectly common path interferometric arrangement. For two dimensional plasmonic structures the method could be extended by displacing the two polarizations using a Nomarski prism. A nearby planar reflector could provide the reference beam for one polarization and the other polarization would be positioned on the 2d nanostructure. We believe this would be a helpful and logical extension of the present method while allowing the same image acquisition and signal processing methods.

If we use the same process, but now look at the silver guided mode structure that we investigated in the previous chapter, we can see a few interesting things. Figures 5.11 and 5.12 show RCWA simulations of how the reflectance and phase of TE and TM incident light respectively.

Initial measurements have been taken for the TE and TM reflectance; figure 5.13 shows the reflectance corrected for background. These measurements though rough, show promising agreement with the theory.

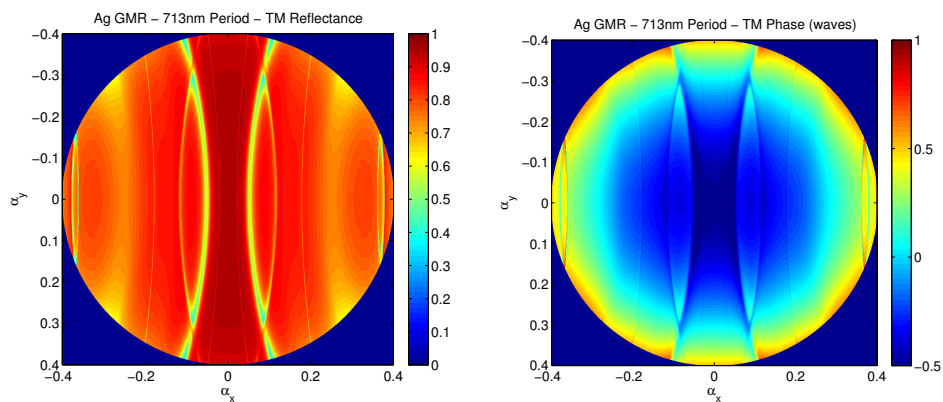
## 5.5 Conclusion

In summary, we have described an experimental study of the angular phase response of a grating-coupled guided mode resonance. Using the surface plasmon



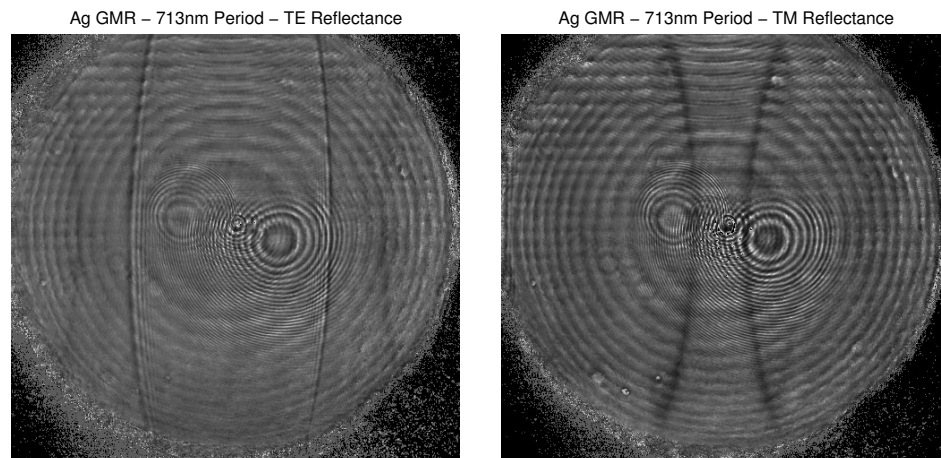
(a) RCWA calculation of 713 nm period silver guided mode resonator TE reflectance. (b) RCWA calculation of 713 nm period silver guided mode resonator TE phase.

Figure 5.11: Theoretical TE reflectance and phase of a 713 nm period silver guided mode resonator.



(a) RCWA calculation of 713 nm period silver guided mode resonator TM reflectance. (b) RCWA calculation of 713 nm period silver guided mode resonator TM phase.

Figure 5.12: Theoretical TM reflectance and phase of a 713 nm period silver guided mode resonator.



(a) Experimental results of 713 nm period silver guided mode resonator TE reflectance.

(b) Experimental results of 713 nm period silver guided mode resonator TM reflectance.

Figure 5.13: Experimental results of the reflectance vs angle of the grating-coupled silver guided mode resonator described in chapter 4.

as an example, we have shown how the phase response can be measured over the angular spectrum using the exit pupil fields of a microscope objective with the TE illumination functioning as the reference beam. We show a phase swing of  $\sim 0.4$  waves through resonance, in close agreement with RCWA models for our structure. We have also shown the theoretical angular response of a grating-coupled guided mode resonator, and some preliminary reflectance results that show agreement with the theory.

## Chapter 6

# The Parametric Plot: A New Way of Looking at Guided Mode Resonances

### 6.1 Introduction

A guided mode resonance usually refers to the coupling between an incident wave external to a structure and confined modes (strictly guided or leaky) whose energy is confined within an all-dielectric or metal-dielectric structure. They have a long and rich history, mainly for their potential in optical filtering and sensing. The tools used for understanding and designing structures that will support such resonances range from effective medium approximations, Kogelnik-style coupled wave analyses [87; 88], and rigorous coupled wave analysis (RCWA)[52; 66; 58; 67; 68; 69; 70]. Depending on the application, attention has been given to very narrow line widths, the details of the line shape, and beam size effects in the reflectance or transmission properties[34; 40]. The role of the *complex* reflectance or transmittance (e.g. including both amplitude and phase) has often not been of central importance in design; furthermore, while the amplitude and phase are always

coupled via the Kramers-Kronig relations [16], it is not always clear how they are related in particular designs. For example, Alonso-Gonzalez *et al.* [89] published an excellent experimental study of the spatial phase response of nanostructures and nano particle assemblies, but few studies have given special attention to the general phase behavior.

In the previous two chapters, we have investigated the experimental measurement of the phase response of guided mode resonance structures. We observed that both the spectral phase and the phase of the angular spectrum can, depending on the geometry, be extremely sensitive to the dimensions of the structure and the refractive index of the environment. This can be an advantage for applications that require optical sensing. In this chapter we will report a more complete examination of the phase response by making use of a parametric (phase space) plot of the complex reflectance or transmittance. We first show that Fano-type resonances (including guided mode resonances) follow a circular trajectory in the complex plane that allows one to easily visualize the amplitude and phase together. We further show, by illustration, that one can identify resonances that circumnavigate the origin (over coupled resonances), that pass through the origin (critically coupled), and that fall short of the origin (under coupled). We will also show that these resonances can be modeled by extending the Fano asymmetry factor into the complex plane. To illustrate these principles, we'll first show a numerical example of a structure whose trajectory can be controlled with a small change in process parameters. To do this, we will use data obtained in the guided mode resonance experiment from chapter 4, fitting the results to the model of a generalized Fano resonance.

## 6.2 The Phase of the Fano Resonance

It has been observed in several excellent review articles [90; 85] that the physical behavior of guided mode resonances quite often fits the mathematical description of the interaction between a continuous spectrum and a discrete state that was analyzed in detail by Ugo Fano [20; 91]. Because Fano addressed systems in which the phase of the wave is rarely measured directly, the strongest attention was naturally given to the *strength* of the interaction (e.g. a transition probability in quantum mechanics or an optical reflectance in the case of a grating) rather than the phase evolution through resonance. To explicitly include the phase, it is therefore necessary to present the complex form of the Fano resonance. While the information here is contained implicitly in the treatment of Fano and others, it will be helpful for us to define a normalized complex form for the Fano resonance:

$$p(\delta) = \frac{1}{(1+iq)} - \frac{1}{(1+i\delta)} = \frac{i(\delta-q)}{(1+i\delta)(1+iq)}, \quad (6.1)$$

in which  $p(\delta)$  represents the complex response (normalized to unity at  $\delta_+ = -1/q$ ),  $\delta = (\omega - \omega_0)/\Delta\omega$  is the detuning of the optical frequency  $\omega$  from resonance ( $\omega = \omega_0$ ) normalized to the resonance half-width  $\Delta\omega$ , and  $q$  represents Fano's asymmetry parameter. Using the complex form, we can find the phase  $\phi$  (For a detailed derivation, see appendix E.):

$$\cos \phi(q) = \frac{(\delta+q) \operatorname{sgn}(\delta-q)}{\sqrt{1+\delta^2}}, \quad (6.2)$$

$$\sin \phi(q) = \frac{(1-q\delta) \operatorname{sgn}(\delta-q)}{\sqrt{1+\delta^2}}.$$

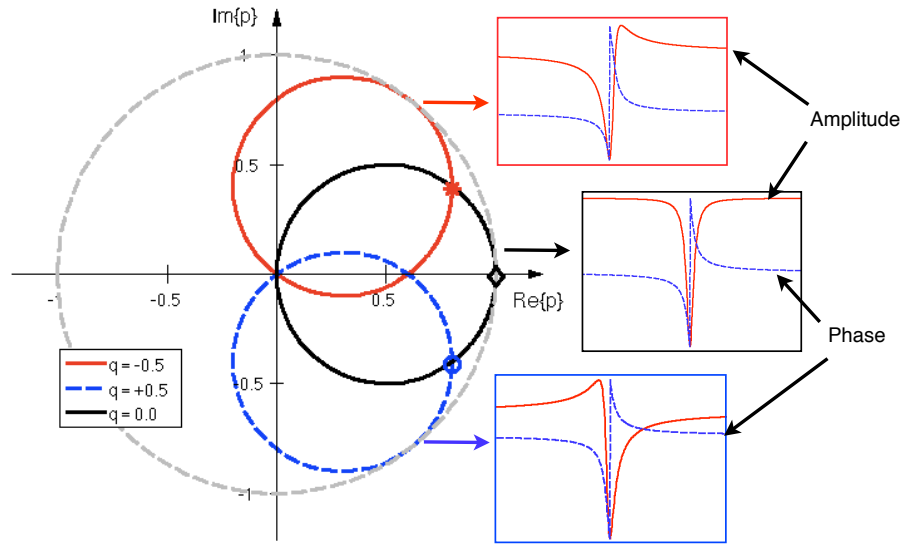


Figure 6.1: Parametric plot showing the amplitude and phase of the Fano resonance for various values of the asymmetry parameter  $q$ . The circles indicate the endpoints of the spectrum.

While equation 6.2 is suitable to track the phase in the complex plane, it is instructive to visualize the amplitude and phase evolution of the resonance together in the complex plane, using the detuning  $\delta$  as a parameter. Figure 6.1 shows the results for a family of values of  $q$ . Each Fano resonance traces a circle in the complex plane of radius 0.5 that passes through the origin and has a center oriented at an angle  $\psi(q)$  with respect to the real axis. We can deduce this by evaluating the phase argument of  $p(\delta_+)$ :

$$\cos \psi(q) = \frac{1 - q^2}{1 + q^2}, \quad (6.3)$$

$$\sin \psi(q) = \frac{-2q}{1 + q^2}.$$

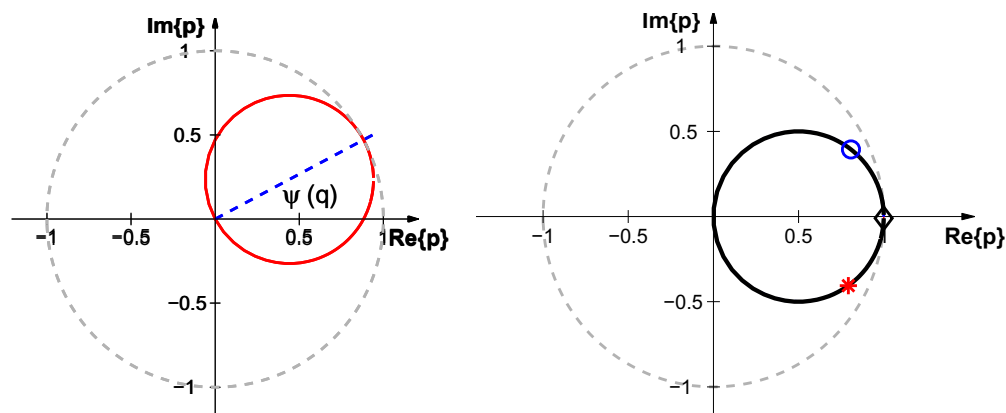


Figure 6.2: The Fano resonance for all values of  $q$  when each is rotated by the phase  $\psi(q)$ . Left: Geometry of the rotation. Right: Three values of  $q$  rotated to the real axis. The symbols indicate the end points for the trajectories: asterisk:  $q = +0.5$ ; diamond:  $q = 0$ ; circle:  $q = -0.5$ .

The starting ( $\delta \rightarrow -\infty$ ) and ending ( $\delta \rightarrow +\infty$ ) point of each spectrum (shown by the markers in figure 6.1) coincide and lie on the intersection with the  $q = 0$  trajectory. Each trajectory approaches the origin in a clockwise fashion as  $\delta$  increases from  $-\infty$ .

Since the center of each circle differs from  $q = 0$  by a global phase, it is easy to apply a rotation such that all Fano resonances of this form trace out the same trajectory, only differing according to the starting/ending point on the circle:

$$p(\delta) = \frac{i(\delta - q)}{(1 + i\delta)(1 + iq)} e^{i\psi}. \quad (6.4)$$

Figure 6.2 illustrates this, as the  $q = \pm 0.5$  resonances shown in figure 6.1 have been rotated to lie on the  $q = 0$  resonance. In this representation, different values of  $q$  are distinguished only by the position of the endpoints on a unit diameter circle centered at  $x = 0.5$ . (This formulation is strictly true only for real values of  $q$ ; we will consider complex values of  $q$  presently.)

Since, for an ideal resonance, all of the trajectories intersect the origin, there always exists exactly one point of complete extinction and one maximum, nor-

malized to unity. We will refer to such a resonance as *critically coupled*.

### 6.3 The Generalized Fano Resonance

Many resonances, including optical resonances of the types studied here, do not reach complete extinction yet still show the functional form of a Fano resonance. Zhang and Govorov [92] are among a number of authors that have examined systems that can be described using a Fano asymmetry parameter that is extended into the complex plane. (We will call this the *complex Fano factor*, using the terminology of Zhang and Govorov.) For complex Fano factors  $q = q_R + iq_I$ , the maximum and minimum values of  $\delta$  no longer occur at  $\delta_+ = -1/q$  and  $\delta_- = q$ . By maximizing the amplitude of  $p(\delta)$  for complex  $q$ , it is straightforward to show that  $\delta_{\pm}$  are solutions to the quadratic equation:

$$\delta_{\pm}^2 + \left( \frac{|q|^2 - 1}{q_R} \right) \delta_{\pm} - 1 = 0. \quad (6.5)$$

We will use this to define a normalized form of equation 6.1 that will represent a complex reflection or transmission coefficient  $\eta(\delta)$ , depending on the specific optical geometry:

$$\eta(\delta) = \eta_0 \frac{i(\delta - q)}{(1 + i\delta)(1 + iq)}, \quad (6.6)$$

in which the complex normalization factor  $\eta_0$  is given by  $1/p(\delta_+)$ . This has the effect of normalizing the reflection or transmission spectrum to a maximum value of unity and rotating the phase so that the maximum lies on the real axis of the complex plane.

The impact of a complex valued  $q$  on the phase of the resonance can be readily understood using the parametric plot of figure 6.3. In the complex plane, a failure to reach extinction simply means that the trajectory no longer passes through the origin. Evidently, a value of  $q$  that lies above the real axis ( $q_I > 0$ ) in the complex

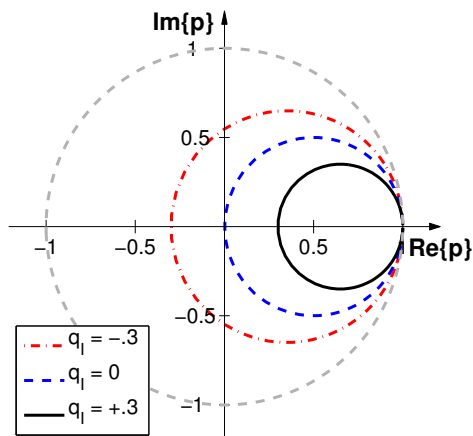


Figure 6.3: The Fano resonance for three values of  $q$  in which the imaginary part varies while the real part is 0.

plane will stay in the two right quadrants, while a value of  $q$  that lies below the real axis  $q_I < 0$  will circumnavigate the origin, passing through all four quadrants and thus accomplishing a full  $2\pi$  phase swing through resonance. Thus, one can in principle have two resonances with similar extinction but whose phase evolution over the resonance differs substantially. If  $q_I = 0$  represents a critically coupled resonance, we will refer to  $q_I > 0$  as an *under coupled* resonance and  $q_I < 0$  as an *over coupled* resonance.

## 6.4 Parametric Analysis in the Design of Guided Mode Resonances

We now turn to a numerical example of a critically coupled resonance using the example guided mode resonance described in chapter 4 and address the question of whether it is possible, in principle, to have an over coupled resonance. To do so, we will again make use of rigorous coupled wave theory. The structure is a

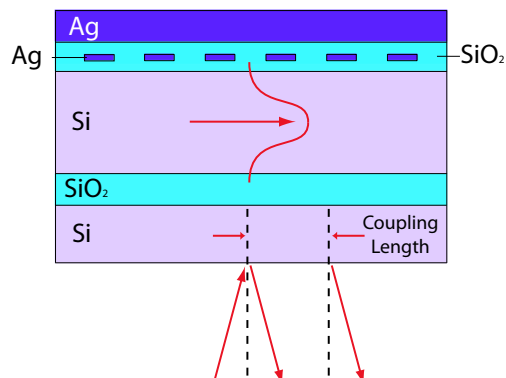
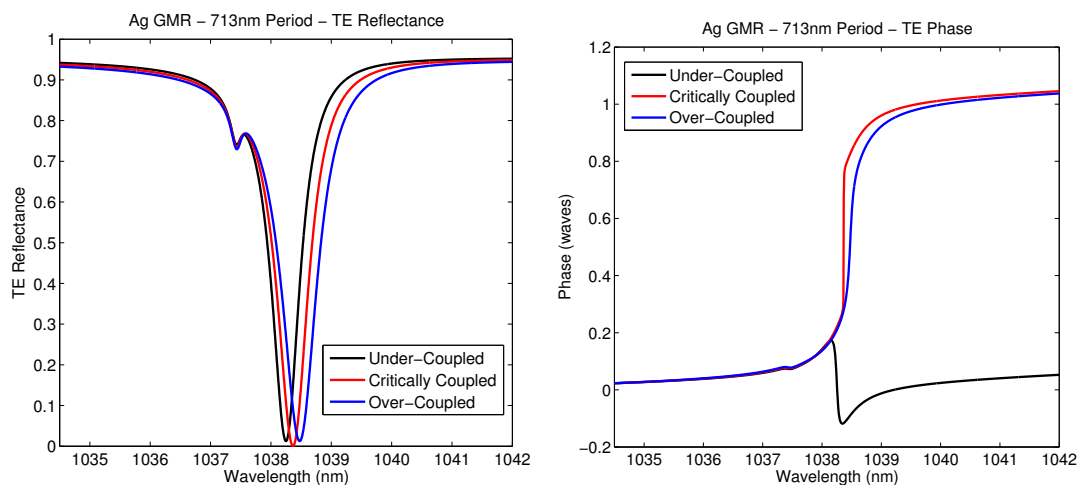


Figure 6.4: Diagram of example structure. The thicknesses are as follows: silicon waveguide layer,  $2.411 \mu\text{m}$ ; buried oxide,  $1.080 \mu\text{m}$ ;  $\text{SiO}_2$  isolation layer,  $110 \text{ nm}$ ; grating layer,  $18 \text{ nm}$ ; the oxide cap layer is varied to control the coupling conditions ( $80 - 106 \text{ nm}$ ).



(a) Reflectance of the three cases.

(b) Phase anomaly for three designs.

Figure 6.5: Examples of critically coupled, under coupled and over coupled resonances modeled using rigorous coupled wave analysis. Each structure is based on the structure shown in figure 6.4, each differing by  $13 \text{ nm}$  in the  $\text{SiO}_2$  cap layer thickness.

silicon on insulator waveguide that is equipped with a grating layer separated from the waveguide by an oxide isolation layer. The structure is then completed using a metal (silver) reflector separated from the grating by an oxide cap. Figure 6.5 shows the RCWA model for the reflectance and phase data. We now take the same RCWA computation and display it in a parametric plot of the complex reflection coefficient over the complex plane (figure 6.6). The sample as modeled is clearly under coupled; while the resonance looks relatively deep in reflectance, the complex amplitude plot (proportional to the square root of the reflectance) shows the under coupling clearly. The other two plots show the effect of progressively increasing the silicon dioxide cap layer (first by 13 nm and then 26 nm); doing so we obtain the red and blue curves for figures 6.5 - 6.6 respectively. Evidently a relatively minor change in the cladding region (inducing only a 0.1 nm shift in position and an increase in the minimum by about .01) has a tremendous influence on the phase swing. To summarize: while over- and under coupled resonances have similar maximum phase slopes, the full phase swing through resonance for the over coupled case is over three times that of the under coupled case. These cases can be distinguished from each other on the parametric plot as well; for the over coupled case the trajectory encompasses the origin, and the under coupled case does not.

## 6.5 Experimental Example

Next, we will make use of the Fano resonance model to re-examine the *experimental* data described in chapter 4. The guided mode resonance structure is shown in figure 6.4 in which a high reflectance multilayer is illuminated through the substrate. The grating (samples were fabricated with periods ranging from 675 nm to 715 nm) provides the resonant interaction between a continuum (external propagating waves) and the discrete spectrum of the guided modes.

In our case, the bottom of the substrate is equipped with an  $\text{Al}_2\text{O}_3$  coating

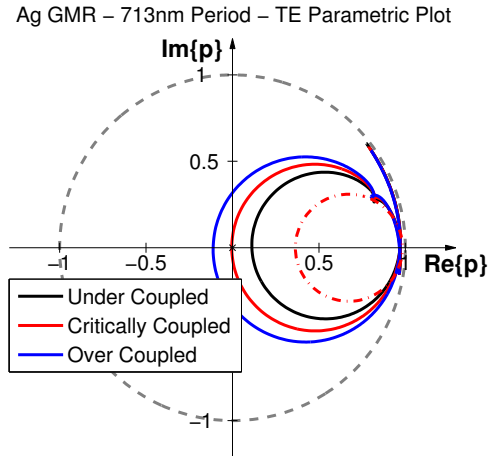


Figure 6.6: Parametric representation of three designs. The experiment is shown in the dashed (red) circle

to reduce the reflectivity. A reflection from the bottom of the weakly reflecting substrate ( $470 \mu\text{m}$  thickness) produces spectral fringes of good visibility having a period of about  $0.34 \text{ nm}$ . In chapter 4, we made use of Fourier analysis to extract the phase and found a phase slope close to the bandwidth limitation of our analysis. Here we apply an analysis based on the generalized Fano resonance as follows: We synthesize a set of spectral fringes using the interference of a background signal with that of a generalized Fano resonance:

$$I_s(\delta) = \left| p_0 \frac{i(\delta - q)}{(1 + i\delta)(1 + iq)} + \sqrt{I_B} e^{i(k_0\delta + \phi_0)} \right|^2, \quad (6.7)$$

where  $k_0$  is the frequency of the spectral interference fringes and  $\phi_0$  is a slowly varying phase. In practice, we fit to the experimental data by optimizing for the parameters of the generalized Fano function: resonance width; resonance center; and the real and imaginary parts of  $q$ . We use an objective function that is the mean square difference between the experimental fringes and the theory. The final uncertainty in the fit is the quadratic coefficient of the spectral phase  $\phi_0$  that

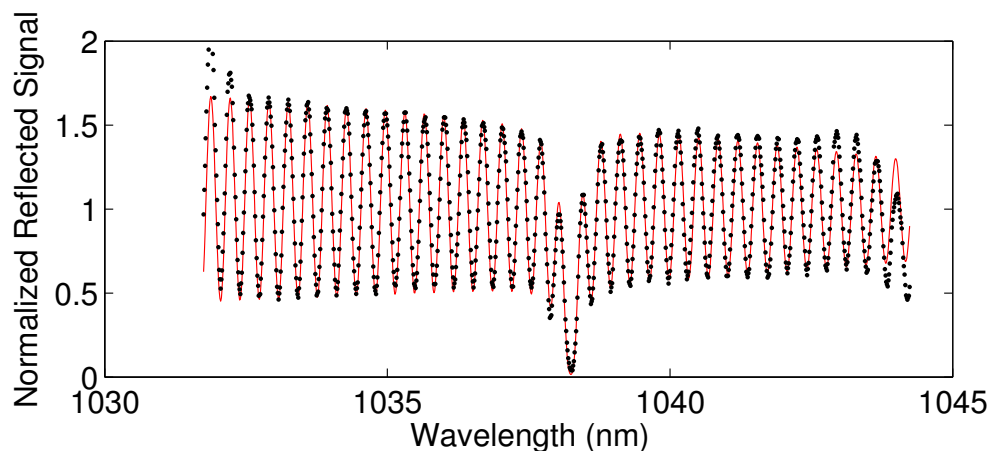


Figure 6.7: Reconstruction of the fringe pattern using a Fano resonance model (solid line) compared with the normalized spectrum from the OSA (data points). The spectral width FWHM of the Fano resonance is 0.34 nm;  $q = .022 + 0.37i$ ; the quadratic phase correction was  $-1.71 \times 10^4 \text{ rad}/\text{nm}^2$ .

results from the material dispersion of the silicon substrate; while it has a minor influence on the resonance itself, the dispersion does influence the phase on the edges of the spectrum and improves the overall fit. Our procedure here is first to estimate the quadratic phase from a reference measurement taken from a region of the sample without the grating and make small adjustments to the quadratic phase during the optimization.

The results of the example experiment, including a fit to the experimental fringes, are shown in figure 6.7. The trace was taken at the highest resolution possible with the optical spectrum analyzer (Ando Model AQ-6315A at 0.1 nm resolution) in order to minimize the effects of the instrument on the phase response, and normalized to the reflectance from a region of the sample without grating, yielding a mean value of 1 at the very edges of the spectrum. The observed fringe visibility arises from a normalized background signal of about 5 % of the peak reflectance from the sample. Figure 6.8 shows the results presented in the conventional way, displaying the reflectance and phase evolution of the

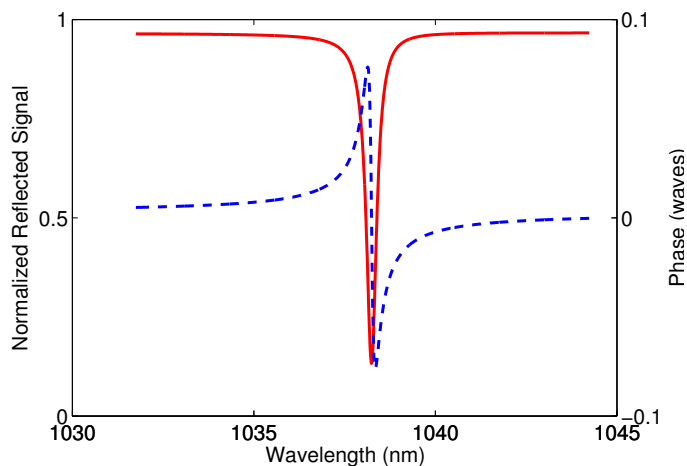


Figure 6.8: Amplitude and Phase of the resonance extracted from the experimental fit of figure 6.7.

resonance inferred from the experimental data of figure 6.7.

We have also included the parametric version of the best-fit Fano resonance on the parametric plot of figure 6.6. While one can infer, from the small phase swing of figure 6.8 that the resonance is under coupled, it becomes very clear in the parametric plot.

## 6.6 Discussion

We have investigated the phase of the ideal Fano resonance and compared it to that of a particular example structure in numerical simulation and experiment. The parametric (phase space) representation is a useful tool both for understanding the influence of the asymmetry factor on the resonance and to visualize the maximum phase swing that can occur through resonance. We now turn to a more general discussion of the phase of guided mode resonances in light of the parametric analysis. In addition to the specific case cited here, we have applied RCWA

to a variety of other guided mode resonances that have been reported in the literature. The following discussion represents a qualitative description of our findings, the details of which will be published at a later date. We will also distinguish between positive resonances (signals having a narrow peak and a low baseline) and negative resonances (signals that exhibit a narrow dip against a high baseline). For example, conservation of energy requires that a dielectric structure having a negative resonance in reflection will have a positive resonance in transmission.

In examining the reflection and transmission resonances of both all-dielectric as well as structures incorporating metal, we have found both positive and negative resonances. We have seen reflectance resonances of both all-dielectric and lossy guided mode resonators with both positive and negative resonances that can be under, critically, or over coupled. For transmission resonances we have observed under coupled resonances, that can approach a critically coupled condition; however, no combination of parameters has yielded a truly critically coupled or over coupled transmission resonance. This appears to be true for both lossless dielectric and metal-dielectric structures.

We believe that the reason a reflection resonance is able to be over coupled, is fundamental to how a guided mode resonance is produced. Light that is specularly reflected (Fresnel reflection) interferes with light that has been grating out-coupled from the waveguide after it has propagated some distance in the waveguide. The relative amplitude and phase between these two reflections will determine the characteristics of the resonance. If we then consider how light interacts with a structure in transmission, time reversal symmetry must hold: light passing through from one direction must behave the same, in both amplitude and phase, as light passing from the opposite direction. A reflective resonance is not bound by this; light reflecting from one side of the structure will often scatter differently than light reflecting off the opposite side. In our case, the phase of the specular

reflection is dependent on the multilayer, and if configured correctly, can produce a  $\pi$  phase shift upon reflection. In our case we were able to change the phase of the specularly reflected light by adjusting the distance between the grating and the mirror, which provides a means of adjusting the phase of the specular light independent of the grating coupled light. For structures that work in transmission, this independent adjustment is not possible since changing the multilayer stack will always affect the phase of both the specular and grating coupled light. For the Fano resonance description, extending the Fano factor  $q$  into the complex plane can describe an under coupled or over coupled resonance. Zhang and Govorov [92] found this to be a consequence of time reversal symmetry (or lack thereof) in quantum mechanical systems.

While the parametric picture is useful in visualizing the character of the resonance, it obscures information about the rate of change of the complex amplitude with frequency; in the parametric plot, a large number of points away from resonance are clustered near the end points of the trajectory. And because the distance from the origin is proportional to the field (rather than the reflected energy), incomplete extinction (as is the case for over coupled and under coupled systems) is magnified.

It is clear from the rigorous coupled wave results shown in figures 6.5 and 6.6 that there is a second resonance present near the dominant one. While its influence on the phase appears weak, the interference of the two resonances appears as a cusp in the parametric plot. We have so far limited our analysis and experimental fit to a single-resonance Fano model, but we believe it could be fruitful to reexamine the treatment in light of the many examples in the literature of overlapping and interfering resonances. We hope to address this in a future publication.

Finally, we consider the use of the complex Fano resonance in extracting the amplitude and phase from the experimental spectra. Our earlier treatment made use of a Fourier analysis technique whose spectral resolution was approximately

limited to one fringe period of the interferogram. Since the Fano reconstruction is model based, it is not band limited in the same way. However, being a model-based extraction method, it can miss small phase fluctuations that might be detected using other methods. It is possible that the class of functions studied here could be usefully applied in, for example, a singular value decomposition in order to analyze systems with multiple resonances (or, in the case of quantum systems, degenerate states).

## 6.7 Conclusion

In conclusion, we have presented a parametric (phase space) analysis of guided mode resonances using a generalized Fano resonance, and compared that picture to the numerical results from a simulated guided mode resonance. We have also used the generalized Fano resonance as a way of extracting the amplitude and phase response in an experiment and find this to be a useful way of representing the measured amplitude and phase.

## Chapter 7

# Conclusions and Future Work

This thesis presents the optical properties of a relatively new material, gallium implanted silicon (Si:Ga). Using a dual-beam SEM/FIB we were able to fabricate test samples of Si:Ga of varying ion dose. Ellipsometry was done on pads ranging from a dose of 0.01 to  $0.3\text{nC}/\mu\text{m}^2$ , and the optical constants were fit using a simplex algorithm. This ellipsometry when combined with broadband reflectance spectra allowed us to determine the optical constants over the visible and near-infrared wavelength ranges. We found that a dose as small as  $0.01\text{nC}/\mu\text{m}^2$  changed the optical properties of single crystal silicon to that of amorphous silicon in a thin ( $\sim 40$  nm) surface layer. We also found that doses greater than  $0.1\text{nC}/\mu\text{m}^2$ , exhibit optical properties that should, in theory, be able to support surface plasmons, especially in the near-infrared. In addition to the optical properties we have explored some of the thermal characteristics of the material, noting that as the temperature increases, gallium starts to leach out of the implanted pads and accumulates on the surface.

Aluminum oxide, silicon dioxide and carbon implantation masks have been investigated, and have been shown to act as an acceptable dummy layer for implantation. We have presented initial results on a new gallium implanted carbon material that is resistant to oxygen plasma ashing. This material could possibly

be useful for writing intricate electrical contacts relatively easily.

Following up on the work of La Marche, Levi-Setti and Wang [63], we used this new Si:Ga material to create free standing arrays of nanowires in a variety of configurations. These nanowires, when combined with the substrate reflection, can yield substantial amounts of retardance with relatively low diattenuation. The combination of substrate reflection with the polarization dependent reflection of the nanowires creates a nanoscale Fabry-Perot cavity, allowing the structures to be tuned to different diattenuation and retardance by changing the distance between the two by altering the etch. Since implantation is done with a focused ion beam system, we are able to create spatially variant arrays of nanowires to create structures that have spatially variant orientation of the retardance. The retardance, diattenuation and orientation of retardance of these structures have been measured by taking a sequence of images using a polarimetric microscope and subsequent image analysis using a sample Jones matrix retrieval algorithm in MATLAB. These results compare favorably with the theoretical optical properties calculated using rigorous coupled wave analysis (RCWA) and the Si:Ga optical constants calculated in chapter 2.

The second half of the thesis presents the amplitude and phase response of two representative types of guided mode resonances. Using more traditional materials and fabrication processes we fabricated silver grating coupled silicon-on-insulator waveguide based guided mode resonators. We presented experimental results showing the reflectance and spectral phase of a 713 nm period guided mode resonator. To obtain the phase information we constructed an experimental apparatus that used a reflection off the substrate to act as a reference beam. This beam, when combined with the reflection off the silver grating of the device provides an interference pattern in the measured spectra. We were then able to extract the phase of this fringe pattern using Fourier analysis to obtain the spectral phase response of the resonance. This data was compared with the theoretical

properties generated using RCWA. We were able to show, using RCWA, that ideal structures can have a very large phase swing through resonance, and that this phase swing is extremely sensitive to process parameters. We believe that this sensitivity could be exploited increase the sensitivity of sensors that currently only use the reflectance of guided mode resonators.

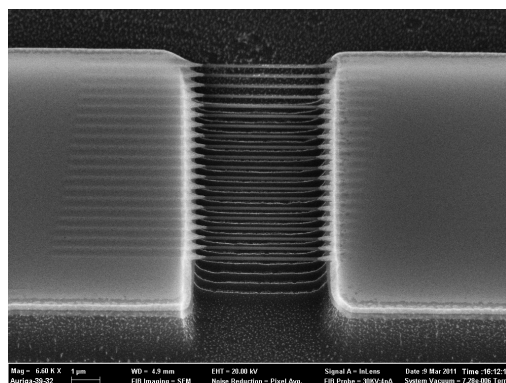
We also presented a look at how the angular phase of surface plasmon polariton varies. Fabrication of the grating coupled surface plasmon polariton structure was done using a patterned grating lift off technique on a silicon wafer like that used in the fabrication of the SOI based guided mode resonance. To measure the angular phase response we adapted the setup that we used for the spectral phase measurement, by adding shearing optics in the imaging path and removing the cylindrical lens. We were able to exploit the fact that the silver surface plasmon polariton only has a slowly varying phase on reflection for light whose electric field is polarized parallel to the grating orientation (TE with respect to the grating). This fact allowed us to use the TE light as a reference to extract the phase of TM light, which excites the surface plasmon polariton. Extraction of the phase from the resulting two dimensional interference image was done similar to the one dimensional Fourier techniques used for the spectral phase, except in two dimensions. We were able to show that the measured phase and reflectance agreed well with the RCWA theory.

Finally, we investigated the phase of an ideal Fano resonance and compared it to the data of an experimental structure. Fitting the experiment to a generalized Fano resonance, we were able extract the amplitude and phase. This method has the potential to bypass problems associated with Fourier techniques that can limit the maximum measurable phase slope. We showed that the parametric phase representation is a useful tool both for designing resonates, and for understanding how the Fano asymmetry parameter influences a resonance.

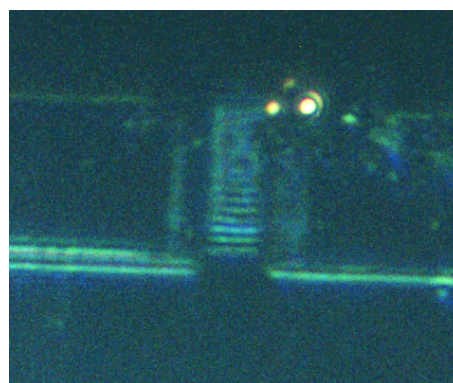
## Future Work

### Coherent Thermal Emission

One of the projects that we feel could be interesting is an extension of the linear Si:Ga nanowire arrays. If we pass an electrical current through a filament, it will heat up and emit light via thermal emission. We also know that when emitters are placed in close proximity to each other, they can acquire coherence by virtue of coupled resonances. It would be interesting to look at the coherence properties and the angular dependence of light that was emitted from an array of nanowires. Initial tests on this proved unsuccessful when using a standard commercial silicon wafer, as seen in figure 7.1. We believe that that the problem in our sample was that the electrical current was passing through our substrate instead of through our nanowires. To combat this, it may be wise to fabricate similar samples on SOI. This way, we can etch down to the oxide layer, which will prevent the nanowires from being short circuited. One worry we had about this is that the nanowires



(a) SEM micrograph of Si:Ga nanowire array.



(b) Light emission from sample when an electric potential was applied across the two sides.

Figure 7.1: Initial Si:Ga nanowire emission results. Sample was fabricated on a commercial silicon wafer, and consisted of two Si:Ga pads separated by Si:Ga nanowires.

need to get extremely hot in order to emit light, and as we noted, Si:Ga is very unstable at elevated temperatures. To test this, we heated nanowires up to 300°C; gallium leached out of the implanted regions where there was silicon below it, but regions that were freed from the substrate by the etch were unaffected by the heat.

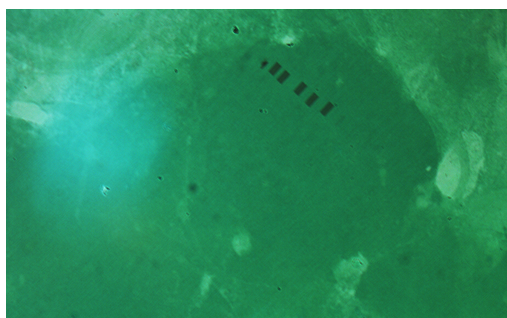
## **Upgrades to the GMR phase measurement apparatus**

The experimental apparatus that we used to measure the phase effects of guided mode resonators works well for samples that have a built in means of producing a reference signal. For the first sample measured (silver grating coupled SOI waveguide based guided mode resonance), we were able to exploit that fact that we were using back side illumination. This allowed us to obtain our reference signal from the substrate reflection. The second sample measured (grating coupled silver surface plasmon polariton), produced its own reference by means of using the slowly varying TE polarized portion of the light when illuminated with 45 degree polarized light.

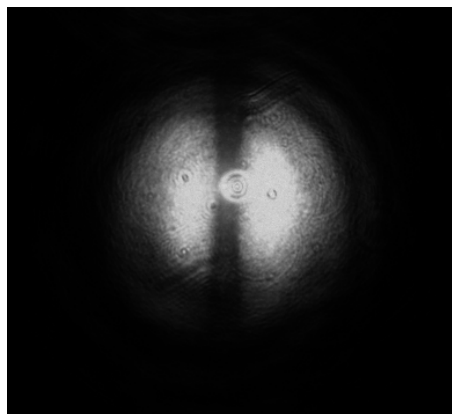
A logical extension of the apparatus would be to accommodate samples that do not provide such niceties. One means of doing this is to place a Nomarski prism prior to the focusing objective, such that the point where the two sheared beams overlap coincides with the entrance pupil of the objective. This setup will produce lateral focal splitting, where the orthogonally polarized sheared light will be focused onto different parts of the sample. This will allow one focal spot to be placed on the grating, and the other to be placed away from the grating on the substrate to act as a reference. This design should work well where the substrate reflection is easily known or modeled. If this is not the case, a reference reflector can be created on the sample during the fabrication process.

## Si:Ga Guided Mode Resonators

An obvious extension of this thesis is to bridge the gap between the two halves by making gallium implanted silicon guided mode resonators. Extensive RCWA design work has been carried out which shows it should be possible to fabricate them in theory. Attempts to fabricate Si:Ga GMRs have been made on an experimental silicon on glass substrate obtained from Corning Inc. but have displayed broadened and shallow resonances. We believe the primary reason the samples exhibited poor resonances is due to loss. The loss could either be caused by the experimental substrate or from the gallium implantation method. It would be beneficial to try fabricating some samples on standard SOI wafers to determine if the implantation method is feasible for guided mode fabrication.



(a) Light microscope image of Si:Ga guided mode resonators.



(b) TE reflectance in the Bertand lens configuration taken with a 20x microscope objective using the setup shown in figure 5.2. The illumination consisted of an ASE light source along with a 1064 nm normal incidence notch filter used at 15 degrees.

Figure 7.2: Si:Ga guided mode resonator fabricated in a silicon on glass substrate.

# Bibliography

- [1] O. Römer, “Demonstration touchant le mouvement de la lumiere trouve par M. ROMER de l’Academie Royale des Sciences,” *Journal des Savans* **10** (1676).
- [2] E. Berthelsen, “Experimenta Crystalli Islandici disdiacastici quibus mira et insólita refractio detegitur,” *Hafniae (Kopenhagen)* **1669**.
- [3] C. Huygens, “Traité de la lumière [Treatise on light],” Pierre vander Aa, *Marchand Libraire* **1690**.
- [4] T. Young, “The Bakerian lecture: Experiments and calculations relative to physical optics,” *Philosophical transactions of the Royal Society of London* **94**, 1–16 (1804).
- [5] J. Biot, “Phénomènes de polarisation successive, observés dans des fluides homogènes,” *Bull. Soc. Philomath* **190** (1815).
- [6] J. F. W. Herschel, “Light,” *Encyclopedia Metropolitana* **4**, 341 (1841).
- [7] C. Brosseau, Fundamentals of polarized light: a statistical optics approach (Wiley New York, 1998).
- [8] L. Pasteur and A. Ladenburg, Ueber die Asymmetrie bei natürlich vorkommenden organischen Verbindungen, no. 28 (W. Engelmann, 1907).
- [9] J.-N. Delisle, “RE’FLEXIONS,” *Mémoires de L’Académie Royale des Sciences* p. 166.
- [10] G. F. Maraldi, “Diverses expériences d’optique,” *Mémoires de L’Académie Royale des Sciences* p. 111.
- [11] A. Fresnel, “Memoire sur la double refraction que les rayons lumineux eprouvent en traversant les aiguilles de cristal de roche suivant des directions paralleles a laxe,” *Oeuvres* **1**, 731–751 (1822).

- [12] H. C. Oersted, “Electricity and magnetic needles,” *Philosophy* **16**, 273–276 (1820).
- [13] R. C. Jones, “A new calculus for the treatment of optical systems,” *JOSA* **31**, 488–493 (1941).
- [14] R. C. Jones, “A new calculus for the treatment of optical systems,” *J. Opt. Soc. Am* **37**, 107–112 (1947).
- [15] H. Mueller, “Memorandum on the polarization optics of the photo-elastic shutter, NDRC project OEMsr-576,” National Defence Research Committee, Tech. Rep **2** (1943).
- [16] M. Born and E. Wolf, Principles of Optics: Electromagnetic theory of propagation, interference and diffraction of light (Cambridge University Press, 1999), seventh edn.
- [17] J. Thomson, “Notes on recent researches in electricity and magnetism,” *Mercury* **8**, 18 (1893).
- [18] R. Wood, “XLII. On a remarkable case of uneven distribution of light in a diffraction grating spectrum,” *The London, Edinburgh, and Dublin Philosophical Magazine and Journal of Science* **4**, 396–402 (1902).
- [19] L. Rayleigh, “III. Note on the remarkable case of diffraction spectra described by Prof. Wood,” *The London, Edinburgh, and Dublin Philosophical Magazine and Journal of Science* **14**, 60–65 (1907).
- [20] U. Fano, “The theory of anomalous diffraction gratings and of quasi-stationary waves on metallic surfaces (Sommerfelds waves),” *JOSA* **31**, 213–222 (1941).
- [21] A. Hessel and A. Oliner, “A new theory of Woods anomalies on optical gratings,” *Applied Optics* **4**, 1275–1297 (1965).
- [22] R. Ritchie, “Plasma losses by fast electrons in thin films,” *Physical Review* **106**, 874 (1957).
- [23] H. Raether, “Dispersion relation of surface plasmons on gold-and silver gratings,” *Optics Communications* **42**, 217–222 (1982).
- [24] W. Barnes, S. Kitson, T. Preist, and J. Sambles, “Photonic surfaces for surface-plasmon polaritons,” *JOSA A* **14**, 1654–1661 (1997).
- [25] I. R. Hooper and J. R. Sambles, “Surface plasmon polaritons on thin-slab metal gratings,” *Physical Review B* **67**, 235 404 (2003).

- [26] G. Bryan-Brown, J. Sambles, and M. Hutley, "Polarisation conversion through the excitation of surface plasmons on a metallic grating," *Journal of Modern Optics* **37**, 1227–1232 (1990).
- [27] R. Gruhlke, W. Holland, and D. Hall, "Surface plasmon cross coupling in molecular fluorescence near a corrugated thin metal film," *Physical Review Letters* **56**, 2838 (1986).
- [28] R. W. Gruhlke, "Optical emission from surface waves supported in thin metal films," (1987).
- [29] A. Otto, "Spectroscopy of surface polaritons by attenuated total reflection," *Optical Properties of Solids, New Developments* pp. 677–727 (1976).
- [30] R. Magnusson and S. S. Wang, "New principle for optical filters," *Appl. Phys. Lett.* **61**, 1022–1024 (1992).
- [31] R. Magnusson and S. Wang, "Transmission bandpass guided-mode resonance filters," *Applied optics* **34**, 8106–8109 (1995).
- [32] S. Tibulac and R. Magnusson, "Reflection and transmission guided-mode resonance filters," *J. Opt. Soc. Am. A* **14**, 1617–1626 (1997).
- [33] S. M. Norton, G. M. Morris, and T. Erdogan, "Experimental investigation of resonant-grating filter lineshapes in comparison with theoretical models," *JOSA A* **15**, 464–472 (1998).
- [34] S. T. Thurman and G. M. Morris, "Controlling the spectral response in guided-mode resonance filter design," *Applied optics* **42**, 3225–3233 (2003).
- [35] A. E. Bieber and T. Brown, "Integral coupler/resonator for silicon-based switching and modulation," *Applied physics letters* **71**, 861–863 (1997).
- [36] A. Bieber and T. Brown, "Coupling anomalies in SimGen/Si/SiO<sub>2</sub> waveguide systems," *Optics express* **10**, 1139–1144 (2002).
- [37] T. Brown, R. Fabrizio, and S. Weiss, "Semiconductor periodic structures for out-of-plane optical switching and Bragg-soliton excitation," *Optics express* **3**, 433–439 (1998).
- [38] T. Tamir, "Beam and waveguide couplers," in *Integrated Optics* (Springer, 1975), pp. 83–137.
- [39] R. R. Boye and R. K. Kostuk, "Investigation of the effect of finite grating size on the performance of guided-mode resonance filters," *Applied optics* **39**, 3649–3653 (2000).

- [40] J. D. Neiser, Metal grating resonators in silicon-on-insulator waveguides (University of Rochester, 2006).
- [41] D. Mills and E. Burstein, “Polaritons: the electromagnetic modes of media,” *Reports on Progress in Physics* **37**, 817 (1974).
- [42] W. L. Barnes, A. Dereux, and T. W. Ebbesen, “Surface plasmon subwavelength optics,” *Nature* **424**, 824–830 (2003).
- [43] H. Manasevit and W. Simpson, “Single-Crystal Silicon on a Sapphire Substrate,” *Journal of Applied Physics* **35**, 1349–1351 (1964).
- [44] G. Celler, P. Hemment, K. West, and J. Gibson, “High quality Si-on-SiO<sub>2</sub> films by large dose oxygen implantation and lamp annealing,” *Applied physics letters* **48**, 532–534 (1986).
- [45] C. Tuppen, M. Taylor, P. Hemment, and R. Arrowsmith, “Effects of implantation temperature on the properties of buried oxide layers in silicon formed by oxygen ion implantation,” *Applied physics letters* **45**, 57–59 (1984).
- [46] S. Cristoloveanu, J. Pumfrey, E. Scheid, P. Hemment, and R. Arrowsmith, “Thermal donor and new donor generation in SOI material formed by oxygen implantation,” *Electronics Letters* **21**, 802–804 (1985).
- [47] J. Lasky, “Wafer bonding for silicon-on-insulator technologies,” *Applied Physics Letters* **48**, 78–80 (1986).
- [48] J. Haisma, G. Spierings, U. Biermann, and J. Pals, “Silicon-on-insulator wafer bonding-wafer thinning technological evaluations,” *Japanese Journal of Applied Physics* **28**, 1426 (1989).
- [49] W. OLeary, “IBM Advances Chip Technology With Breakthrough For Making Faster, More Efficient Semiconductors,” (1998).
- [50] H. Kogelnik, “Theory of optical waveguides,” in Guided-wave optoelectronics (Springer, 1988), pp. 7–88.
- [51] G. P. Agrawal, Lightwave technology: components and devices, vol. 1 (John Wiley & Sons, 2004).
- [52] M. Moharam and T. Gaylord, “Rigorous coupled-wave analysis of planar-grating diffraction,” *JOSA* **71**, 811–818 (1981).
- [53] M. Moharam and T. K. Gaylord, “Diffraction analysis of dielectric surface-relief gratings,” *JOSA* **72**, 1385–1392 (1982).

- [54] M. Moharam and T. Gaylord, “Three-dimensional vector coupled-wave analysis of planar-grating diffraction,” *JOSA* **73**, 1105–1112 (1983).
- [55] T. K. Gaylord and M. Moharam, “Analysis and applications of optical diffraction by gratings,” *Proceedings of the IEEE* **73**, 894–937 (1985).
- [56] M. Moharam and T. Gaylord, “Rigorous coupled-wave analysis of metallic surface-relief gratings,” *JOSA a* **3**, 1780–1787 (1986).
- [57] S. Peng, Polarization-control Components and Narrow-band Filters Based on Subwavelength Grating Structures (University of Rochester, 1996).
- [58] P. Lalanne and G. M. Morris, “Highly improved convergence of the coupled-wave method for TM polarization,” *J. Opt. Soc. Am. A* **13**, 779–784 (1996).
- [59] J. Orloff, L. Swanson, and M. Utlaut, High Resolution Focused Ion Beams: FIB and its Applications: Fib and Its Applications: The Physics of Liquid Metal Ion Sources and Ion Optics and Their Application to Focused Ion Beam Technology (Springer, 2003).
- [60] M. T. Robinson and O. Oen, “The channeling of energetic atoms in crystal lattices,” *Applied Physics Letters* **2**, 30–32 (1963).
- [61] M. Fried, T. Lohner, E. Jároli, G. Vizkelethy, E. Kótai, J. Gyulai, A. Biró, J. Ádám, M. Somogyi, and H. Kerkow, “Optical properties of thermally stabilized ion implantation amorphized silicon,” *Nuclear Instruments and Methods in Physics Research Section B: Beam Interactions with Materials and Atoms* **19**, 577–581 (1987).
- [62] M. G. Blaber, M. D. Arnold, and M. J. Ford, “A review of the optical properties of alloys and intermetallics for plasmonics,” *Journal of Physics: Condensed Matter* **22**, 143 201 (2010).
- [63] P. La Marche, R. Levi-Setti, and Y. Wang, “Focused ion beam microlithography using an etch-stop process in gallium-doped silicon,” *Journal of Vacuum Science & Technology B* **1**, 1056–1058 (1983).
- [64] D. Goldstein, “Polarized light,” *Polarized light*, by D. Goldstein. 2nd, rev. and exp. ed. New York, NY: Marcel Dekker, 2003 **1** (2003).
- [65] S.-Y. Lu and R. A. Chipman, “Interpretation of Mueller matrices based on polar decomposition,” *JOSA A* **13**, 1106–1113 (1996).
- [66] S. Peng and G. M. Morris, “Efficient implementation of rigorous coupled-wave analysis for surface-relief gratings,” *JOSA A* **12**, 1087–1096 (1995).

- [67] N. Chateau and J.-P. Hugonin, “Algorithm for the rigorous coupled-wave analysis of grating diffraction,” *JOSA A* **11**, 1321–1331 (1994).
- [68] R. Magnusson and S. Wang, “New principle for optical filters,” *Applied physics letters* **61**, 1022–1024 (1992).
- [69] S. Wang and R. Magnusson, “Theory and applications of guided-mode resonance filters,” *Applied optics* **32**, 2606–2613 (1993).
- [70] Z. Liu, S. Tibuleac, D. Shin, P. Young, and R. Magnusson, “High-efficiency guided-mode resonance filter,” *Optics letters* **23**, 1556–1558 (1998).
- [71] S. Peng and G. M. Morris, “Experimental demonstration of resonant anomalies in diffraction from two-dimensional gratings,” *Optics letters* **21**, 549–551 (1996).
- [72] A. T. Cannistra, M. K. Poutous, E. G. Johnson, and T. J. Suleski, “Performance of conformal guided mode resonance filters,” *Optics letters* **36**, 1155–1157 (2011).
- [73] I. A. Walmsley and C. Dorrer, “Characterization of ultrashort electromagnetic pulses,” *Advances in Optics and Photonics* **1**, 308–437 (2009).
- [74] M. Soltani, S. Yegnanarayanan, and A. Adibi, “Ultra-high Q planar silicon microdisk resonators for chip-scale silicon photonics,” *Optics express* **15**, 4694–4704 (2007).
- [75] U. P. Dharanipathy, M. Minkov, M. Tonin, V. Savona, and R. Houdré, “High-Q silicon photonic crystal cavity for enhanced optical nonlinearities,” *Applied Physics Letters* **105**, 101 101 (2014).
- [76] J. Schmid, W. Sinclair, J. García, S. Janz, J. Lapointe, D. Poitras, Y. Li, T. Mischki, G. Lopinski, P. Cheben, et al., “Silicon-on-insulator guided mode resonant grating for evanescent field molecular sensing,” *Optics express* **17**, 18 371–18 380 (2009).
- [77] E. Kretschmann, “The ATR method with focused light application to guided waves on a grating,” *Optics communications* **26**, 41–44 (1978).
- [78] I. R. Hooper and J. Sambles, “Surface plasmon polaritons on narrow-ridged short-pitch metal gratings in the conical mount,” *JOSA A* **20**, 836–843 (2003).
- [79] A. Hibbins, J. Sambles, and C. Lawrence, “Azimuth-angle-dependent reflectivity data from metallic gratings,” *Journal of Modern Optics* **45**, 1019–1028 (1998).

- [80] S. Elston, G. Bryan-Brown, and J. Sambles, “Polarization conversion from diffraction gratings,” *Physical Review B* **44**, 6393 (1991).
- [81] T. J. Constant, A. P. Hibbins, A. J. Lethbridge, J. R. Sambles, E. K. Stone, and P. Vukusic, “Direct mapping of surface plasmon dispersion using imaging scatterometry,” *Applied Physics Letters* **102**, 251 107 (2013).
- [82] H. Raether, *Surface plasmons on smooth surfaces* (Springer, 1988).
- [83] T. López-Ríos, D. Mendoza, F. Garcia-Vidal, J. Sánchez-Dehesa, and B. Panetier, “Surface shape resonances in lamellar metallic gratings,” *Physical Review Letters* **81**, 665 (1998).
- [84] J. Homola, “Surface plasmon resonance sensors for detection of chemical and biological species,” *Chemical reviews* **108**, 462–493 (2008).
- [85] B. Luk’yanchuk, N. I. Zheludev, S. A. Maier, N. J. Halas, P. Nordlander, H. Giessen, and C. T. Chong, “The Fano resonance in plasmonic nanostructures and metamaterials,” *Nature materials* **9**, 707–715 (2010).
- [86] K. M. Mayer and J. H. Hafner, “Localized surface plasmon resonance sensors,” *Chemical reviews* **111**, 3828–3857 (2011).
- [87] H. Kogelnik, “Coupled wave theory for thick hologram gratings,” *Bell System Technical Journal* **48**, 2909–2947 (1969).
- [88] S. M. Norton, T. Erdogan, and G. M. Morris, “Coupled-mode theory of resonant-grating filters,” *JOSA A* **14**, 629–639 (1997).
- [89] P. Alonso-Gonzalez, M. Schnell, P. Sarriugarte, H. Sobhani, C. Wu, N. Arju, A. Khanikaev, F. Golmar, P. Albella, L. Arzubiaga, F. Casanova, L. Hueso, P. Nordlander, G. Shvets, and R. Hillenbrand, “Real-space mapping of Fano interference in plasmonic metamolecules,” *Nano letters* **11**, 3922–3926 (2011).
- [90] A. E. Miroshnichenko, S. Flach, and Y. S. Kivshar, “Fano resonances in nanoscale structures,” *Reviews of Modern Physics* **82**, 2257 (2010).
- [91] U. Fano, “Effects of configuration interaction on intensities and phase shifts,” *Physical Review* **124**, 1866 (1961).
- [92] W. Zhang and A. O. Govorov, “Quantum theory of the nonlinear Fano effect in hybrid metal-semiconductor nanostructures: the case of strong nonlinearity,” *Physical Review B* **84**, 081 405 (2011).

# Appendix A

## Si:Ga Nanowire Fabrication Using a Focused Ion Beam (FIB)

### I. Sample Cleaning and Preparation

1. Start out with an undoped silicon wafer, and dice into smaller samples. Sample must be less than 3" to pass through the airlock of the Zeiss Auriga SEM/FIB. A 1" sample size is recommended as larger samples can become unwieldy resulting in a higher chance of collision with the SEM final lens.
2. Once the silicon is diced up, soak in Acetone for 30 mins and sonicate for 5 mins.



3. Immediately after removing the silicon from the Acetone, place in Isopropyl Alcohol (IPA), as Acetone tends to leave residue on the surface as it dries.
4. Remove substrate from the IPA after about 30 secs, and dry sample with  $N_2$  or compressed air.
5. Place substrate in SouthBay Plasma Cleaner, plasma clean in argon for 15mins at 30 Watts followed by a 5 min oxygen plasma clean at 30 Watts.



6. Final step in sample preparation is to affix the substrate to a 1" SEM stub with double sided carbon tape.

## II. Sample Insertion

1. Place the 1" SEM stub with sample attached in the center of the multi sample holder, and tighten with hex wrench. (WARNING: Do not over tighten the set screw, it will strip out over time.)

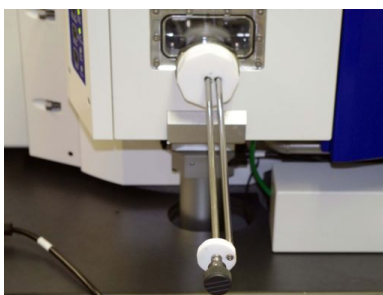


2. Launch SmartSEM software on SEM computer and log in.

3. Vent SEM airlock with the Vent button on the airlock. (WARNING: Do not use the Vent button in the SmartSEM toolbar, this will vent the entire chamber.)



4. Open airlock with handle on the bottom of the airlock, and slide the sample holder on the teflon block with the threaded hole facing the specimen exchange rods. Make sure the stage is slid such that it is attached to the teflon dovetail (trapezoidal shaped block mated with the trapezoidal void in the bottom of the stage). With your left hand placed on the left side of the stage, screw the specimen exchange rods (the black knob) into the stage until snug (Do not over tighten).



5. Close airlock by pushing on the door or handle, do not close door with the specimen exchange rods.
6. Press the transfer button on the airlock. (This will pump out the airlock and open the gate valve into the chamber.) If the stage is not in the exchange position, the stage ready light will not be green. If this happens press the exchange button on the keyboard. This will move the stage to the exchange position and open the gate valve.



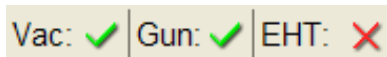
7. Once the gate valve is open fully, push the sample holder into the chamber by pushing on the white teflon disk mounted on the specimen exchange rods. Watch as the sample holder mates with its corresponding dovetail on the stage. Make sure the sample holder is on the dovetail and pushed completely on the stage.
8. Unscrew the specimen exchange rods from the sample holder (12 half turns) and retract the specimen exchange rods until you hear a click.
9. Press the store button on the airlock. This will close the gate valve into the chamber and keep the airlock under vacuum.



### III. SEM Set-Up

1. Press the resume button on the keyboard. This will open the SEM column chamber valve which isolates the chamber from the electron gun. (It may take a few seconds for it to happen, be patient.)
2. Turn on the high voltage for the electron beam. To do this, press the button labeled EHT: in the bottom toolbar in SmartSEM. Next click

EHT On. (Note: EHT = Extra High Tension)



3. Use the XY joystick (right joystick) to place sample in the path of the electron beam.
4. In the stage tab in SmartSEM, set  $M = 4\text{mm}$ . (This is the thickness of the multistage holder. If total thickness of holder and sample is known, use that value. Note: Limits of  $M$  are 0 - 10mm)
5. Bring sample into focus. (Use Focus, X and Y Stigmator knobs.)

#### IV. Sample Eucentricity

1. Find a feature on the surface that can be used as a reference at about  $750\times$ .
2. Turn on the crosshairs, this option can be found in the View menu at the top of SmartSEM.
3. In the stage tab, set the tilt  $T = -2^\circ$ .
4. Set the tilt back to  $0^\circ$ . This will remove the backlash from the tilt motor.
5. Use the XY Joystick to move the bottom of your reference to just touch the X axis of the crosshairs.
6. Set the tilt to  $2^\circ$ .
7. Adjust M-Axis (Z-Axis relative to the tilt orientation).
  - If reference particle moved *up* in Y, use the *up* M-axis button on the joypad to bring it back to the crosshair.
  - If reference particle moved *down* in Y, use the *down* M-axis button on the joypad to bring it back to the crosshair.
8. Set the tilt to  $4^\circ$ . and repeat step 7.

9. Set the tilt to  $7^\circ$ . and repeat step 7.
10. Set the tilt to  $10^\circ$ . and repeat step 7.
11. Set the tilt to  $54^\circ$ . and repeat step 7.
12. Set the tilt to  $0^\circ$ .
13. Repeat steps 3. to 12. for a reference at a magnification of  $1,500\times$ .
14. With the tilt set at  $0^\circ$ , set the working distance to 5.07mm (double click on the WD in the data zone), and adjust Z (Use the joystick) to get the sample back in focus.
15. Set the tilt to  $-2^\circ$  and then to  $0^\circ$ , to remove backlash.
16. Use the XY joystick to place the reference on the crosshair at a magnification of  $1,500\times$ .
17. Set the tilt to  $0^\circ$ . and repeat step 7.
18. Set the tilt to  $4^\circ$ . and repeat step 7.
19. Set the tilt to  $7^\circ$ . and repeat step 7.
20. Set the tilt to  $10^\circ$ . and repeat step 7.
21. Focus the SEM beam using the focus knob. Check working distance. If it is less than 5.05mm, set it to 5.07mm and adjust Z to get it in focus.
22. Adjusting Z may move your reference off the crosshair. If it has, use the XY joystick to place it back.
23. Set the tilt to  $54^\circ$ . and repeat step 7. (Do not panic, if you have done everything correct up to this point, it will not hit the final lens...but it will be close.)
24. Your sample is now eucentric.

## V. SEM-FIB Coincidence

1. Turn on the FIB. Press the button in the top toolbar with a yellow focused beam on it. This will open another window labeled FIB Control. In the FIB tab (first tab) in this window, press the On button under the Gun State heading. This will ramp the FIB EHT up to the voltage of the probe that is currently selected as the imaging probe in the Mill panel (this is usually 30 KV).
2. Make sure that the Regulate box is checked at the bottom of the page. Watch the FIB Suppressor Target, it will adjust the suppressor voltage to stabilize the FIB emission current to  $2.0\mu A$ .
3. Wait until the FIB Suppressor Target stabilizes and you have  $2.0\mu A$  FIB emission. If the gun does not start, use procedure outlined in Appendix B.
4. In the same panel, check the status of the FIB apertures if they are uninitialized, initialize them by pressing the Init Aperture button.
5. Switch to the Mill panel, and select the 30KV: 50pA (reference probe) imaging probe.
6. With your reference object still on the crosshair in SEM mode, switch to FIB imaging by pressing the F8 key on the keyboard. Your reference may move on the screen in both X and Y.
7. Locate the reference object in the FIB image, without moving the stage or shifting the beam. You may need to adjust magnification, focus, X and Y stigmators.
8. Bring the reference object back to the horizontal crosshair by using the Z joystick. (Caution: only move the joystick in the Y direction, moving it in X will tilt the sample, and you may strike the final lens.)
  - If the object is *above* the crosshair, push the Z joystick *up*.
  - If the object is *below* the crosshair, pull the Z joystick *down*.

9. Move your reference object so that it is just touching the vertical crosshair by using the X-axis of the XY joystick.
10. Press F8 to switch back to SEM imaging, and use the X Beam Shift knob on the keyboard to bring the reference object back to the crosshair.
11. Your sample should now be located at the coincident point. To check, switch between SEM and FIB imaging to make sure the reference object does not move. (Note: It will appear different in each imaging mode since you are viewing it at two different angles.) If your reference does move, repeat steps 6. to 10.

## VI. FIB Probe Setup

1. In SEM mode, chose a location on your sample to do the FIB probe setup, as it will damage the surface.
2. Find an object for imaging, or mill one in Fibics (an X with  $20\mu m$  long lines works well).
3. Switch to FIB mode, and fix focus, X and Y stigmators. (It may be beneficial to use Fine mode, to switch between fine and coarse mode press Tab on the keyboard.)
4. In the FIB Control window, switch to the Align tab. Click the Save button at the bottom of the page multiple times. (It does not always save the first time you click it, five or six times should suffice.)
5. Place the imaging object at the center of the crosshair using the XY joystick.
6. In the Align tab, change your probe to FIB Current = 30KV: 2pA.
7. Fix focus, X and Y stigmators. If object is no longer in the center of the crosshair, press the Beam Shift Corr. button under the Additional heading in the Align tab. Use the X and Y adjustments in the right of

the panel to bring the object back into the crosshair. Click the Save button at the bottom of the page multiple times.

8. Repeat step 7. for FIB Current = 30KV: 120pA.

## VII. Fibics File Creation

1. Open Fibics' Nanopattern Visualization Engine 3 by launching the NPVE3.exe shortcut on the fibics computer (upper left monitor).
2. Draw one line using the line tool: Width =  $10\mu m$ , Height =  $0\mu m$ , Angle =  $0.00^\circ$ .
3. Set its thickness to  $0.100\mu m$
4. Click on the array builder button. (Button has four small squares)
5. Set the #Cols to 1, the #Rows to 10 and the spacing to  $0.250\mu m$ . Click Ok.
6. Highlight all lines (Highlighted objects are green) and set X and Y to  $0.000\mu m$ .
7. Create a rectangle with the rectangle tool with the following parameters: Width =  $7.000\mu m$ , Height =  $7.000\mu m$ , Angle =  $0.00^\circ$ , X and Y =  $0.000\mu m$ . Check the void box below where you set the angle.
8. Highlight all lines and the rectangle. Press the array builder button. Set the #Cols to 2, the #Rows to 2 and the spacing to  $12.000\mu m$ . Click Ok.
9. Highlight one set of lines with corresponding rectangle and click array builder. Set the #Cols to 1, the #Rows to 1, and set the Rotation to  $-45.0^\circ$ .
10. Repeat step 9. for two other sets of lines and use Rotation =  $45.0^\circ$  and  $90.0^\circ$  respectively.

11. Highlight all lines and boxes and set X and Y =  $0.000\mu m$ .
12. Click the FIB button below the image. It should be in black font now. If it is still in red font, click it again.
13. Unselect the four boxes so only the lines are selected, and set Beam to 30KV: 2pA. Set the dose to be  $0.1\frac{nC}{\mu m^2}$ .
14. Create another rectangle set its Width =  $25\mu m$ , Height =  $25\mu m$ , Angle =  $0.00^\circ$ , X and Y =  $0.000\mu m$ .
15. With only the new large rectangle selected set its beam to 30KV: 120pA, and its dose to  $0.25\frac{nC}{\mu m^2}$ .
16. Save pattern by clicking on the button with the disk icon, and select save all shapes.
17. Press SEM button below the image. Both SEM and FIB should be in red font now. SmartSEM should now have control of the electron beam.

### **VIII. Gallium Patterning**

1. Move sample to location where patterning is desired with XY joystick.
2. Press SEM button below the image. It should be in black font now. Fibics should now have control of the electron beam.
3. Press the button labeled single in the imaging panel. The SEM will scan and show the image in the center window.
4. Click the FIB button below the image. It should be in black font now.
5. If pattern is not still open, open it with the button that has a folder icon below the save button.
6. Make sure all shapes are highlighted and press the start button (to the right of the rectangle button).

7. Once patterning is finished, Press SEM button below the image to give control back to SmartSEM.

## **IX. Sample Extraction**

1. Press the Off button in the FIB panel of the FIB Control window.
2. Press the Exchange button on the keyboard. It will take a while for the stage to move to the exchange position since the M axis is slow.
3. Once the gate valve is completely open, push specimen exchange rods in using the white plastic disk.
4. Screw rod into sample holder until snug.
5. Pull sample holder into airlock using the white disk. Pull until you hear the specimen exchange rods click. The rod retracted light will turn on once sample holder is fully in position.
6. Press vent on the airlock.
7. Pull airlock open with handle on bottom, and unscrew specimen exchange rods.
8. Slide sample holder off teflon block with your left hand while holding the airlock door with your right.
9. Push airlock door closed and press the pump button.
10. Close the NPVE3 program, and log off of the SmartSEM software.

## **X. Reactive Ion Etch**

1. Use the South Bay RIE-2000 that has SF<sub>6</sub> and Ar connections.
2. Set the standby turbo speed to 15,500 RPM.
3. Set the SF<sub>6</sub> mass flow controller (MFC) set point to 3.0 SCCM.
4. Set the Ar MFC set point to 30.0 SCCM.

5. Open the N<sub>2</sub>, Ar and SF<sub>6</sub>.
6. Vent chamber and place sample inside.
7. Turn off vent and pump chamber.
8. Once chamber vacuum reaches 10<sup>-6</sup> Torr, open gas 1 and 2 solenoid valves.
9. Wait 30 seconds. (Vacuum will spike but recover when solenoid valves are opened.)
10. Begin SF<sub>6</sub> and Ar gas flow.
11. Wait until turbo pump reaches a steady state speed of 15,500 RPM.
12. Set the process time to 1minute.
13. Turn the forward power knob so it points to the left (9 o'clock position).
14. Press the RF power button.
15. Tune the reflected power knob so that it minimizes the reflected power.  
(It will not reach zero, 3-6 Watts is normal.)
16. Stop the flow of the SF<sub>6</sub> and Ar MFCs.
17. Once etch is completed, turn off gas 1 and 2 solenoid valves.
18. Stop pumping, and vent the chamber.
19. Once the turbo pump reaches a speed of 750 RPM it is safe to open the chamber, and remove the sample.
20. Pump the chamber until the thermocouple gauge reads less than 999.9 Torr.
21. Stop pumping, and turn off the RIE.
22. Shut off the N<sub>2</sub>, Ar and SF<sub>6</sub>.

## **XI. Wet Etch**

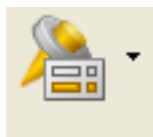
1. Prepare a 50C saturated solution of sodium hydroxide (NaOH), and accompanying beaker of isopropyl alcohol (IPA).
2. Etch sample in NaOH for 90 seconds, place in IPA immediately following.
3. Move sample from IPA to ethanol, and critical point dry it.

# Appendix B

## FIB Beam Start-up Troubleshooting Guide

### I. Normal Startup

1. Turn on the FIB. Press the button in the top toolbar with a yellow focused beam on it. This will open another window labeled FIB Control.



In the FIB tab (first tab) in this window, press the On button under the Gun State heading. This will ramp the FIB EHT up to the voltage of the probe that is currently selected as the imaging probe in the Mill panel (this is usually 30 KV).

2. Make sure that the Regulate box is checked at the bottom of the page. Watch the FIB Suppressor Target, it will adjust the suppressor voltage to stabilize the FIB emission to  $2.0\mu A$ .
3. Wait until the FIB Suppressor Target stabilizes and you have  $2.0\mu A$  FIB emission. If the gun does not start, continue with troubleshooting guide.

**II. Emission starts but FIB suppressor target never stabilizes (cyclic)**

1. Wait until the suppressor voltage is at a maximum (farthest to the left) and uncheck the regulate button.
2. Use the slider to slowly reduce the suppressor voltage to bring the FIB emission to  $2.0\mu\text{A}$ .
  - It is best to change it very slowly. Click the right arrow on the slider a few times then wait for the emission to stabilize before reducing further.
3. Once you get the fib emission stabilized between  $2.0\mu\text{A}$  and  $2.2\mu\text{A}$ , click the regulate button again.

**III. FIB emission never starts and suppressor voltage is at  $-2000\text{V}$** 

1. Uncheck the regulate box, and keep the suppressor voltage at  $-2000\text{V}$
2. Click the Heating.. button on the bottom of the panel. This will open up a new window.
3. Set the filament heating target to  $3600\text{mA}$ .
4. Begin heating the filament. Watch the FIB emission current.
5. Turn filament heating off once the emission current reaches  $50\mu\text{A}$ .
6. Wait 5 seconds then begin to decrease the FIB suppressor voltage. (As before, let it stabilize before moving too far.)
7. Once you get the fib emission stabilized between  $2.0\mu\text{A}$  and  $2.2\mu\text{A}$ , click the regulate button again.

**IV. FIB emission is over  $2.0\mu\text{A}$  with suppressor all the way at  $0\text{V}$ .**

1. Turn off FIB gun.
2. Turn on FIB gun, and let it stabilize. (Regulate is on.)

3. If FIB emission is still above  $2.0\mu\text{A}$ , reduce the FIB extraction target.  
(20-30 Volts at first)
4. Let the emission current stabilize again. If necessary reduce the FIB extraction target again.
5. Repeat as necessary to have an emission current of  $2.0\mu\text{A}$  and a suppressor voltage around  $-100\text{V}$ .

## Appendix C

# Sample Fabrication Using Electron Beam Lithography (Nanopattern Generation System)

### I. Sample Preparation

1. Electron beam lithography requires a grounded sample. If your substrate is not conductive (i.e. glass), it can be coated with a layer of indium tin oxide (ITO). The sample need not be extremely conductive, 35nm of ITO should suffice. (Silicon has enough conductivity to alleviate charging.)
2. Sample must be less than 3" to pass through the airlock of the Zeiss Auriga SEM/FIB.
3. It is recommended that your sample be sized to fit on a 1" SEM stub. (A 1" stub can be provided that has a gold focus standard, spring clip and Faraday cup.)

### II. Sample Insertion

1. Affix sample to stub, and place stub in single sample holder. (WARNING: Do not over tighten the set screw, it will strip out over time.)
2. Launch SmartSEM software on SEM computer and log in.
3. Vent SEM airlock with the Vent button on the airlock. (WARNING: Do not use the Vent button in the SmartSEM toolbar, this will vent the entire chamber.)
4. Open airlock with handle on the bottom of the airlock, and slide the sample holder on the teflon block with the threaded hole facing the specimen exchange rods. Make sure the stage is slid such that it is attached to the teflon dovetail (trapezoidal shaped block mated with the trapezoidal void in the bottom of the stage). With your left hand placed on the left side of the stage, screw the specimen exchange rods (the black knob) into the stage until snug (Do not over tighten).
5. Close airlock by pushing on the door or handle, do not close door with the specimen exchange rods.
6. Press the transfer button on the airlock. (This will pump out the airlock and open the gate valve into the chamber.) If the stage is not in the exchange position, the stage ready light will not be green. If this happens press the exchange button on the keyboard. This will move the stage to the exchange position and open the gate valve.
7. Once the gate valve is open fully, push the sample holder into the chamber by pushing on the white teflon disk mounted on the specimen exchange rods. Watch as the sample holder mates with its corresponding dovetail on the stage. Make sure the sample holder is on the dovetail and pushed completely on the stage.
8. Unscrew the specimen exchange rods from the sample holder (12 half turns) and retract the specimen exchange rods until you hear a click.

9. Press the store button on the airlock. This will close the gate valve into the chamber and keep the airlock under vacuum.

### **III. SEM Start-Up**

1. Press the resume button on the keyboard. This will close the SEM column chamber valve which isolates the chamber from the electron gun.
2. Turn on the high voltage for the electron beam. To do this, press the button labeled EHT: in the bottom toolbar in SmartSEM. Next click EHT On. (Note: EHT = Extra High Tension)

### **IV. NanoPattern Generation System (NPGS)**

1. Change the input on the upper left monitor to DVI-D 1. (Its normal state is HDMI, as it is used as the FIBICs display as well.)
2. Remove the serial connector from the EDAX computer and plug it into the back of the NPGS computer. (Gray cable with 9-pin connector)
3. Turn on the Raith beam blanker. (White box on the back of the SEM desk. It only has one button (on/off))
4. Launch NPGS using proper keyboard and mouse. Be sure to allow the DAC auto-calibration to finish.

### **V. NPGS Pattern File Creation (.DC2)**

1. Open Design CAD Express v16 through NPGS.
2. Create desired pattern using CAD tool.
  - Objects of different color may be given different dose in NPGS.
  - Layers 1-19 can be used for pattern creation. (Layer 20 can be used for comments)

- Objects on different layers can be given different dose, center-to-center and line spacing.
3. Once pattern is finished click the MaxMag option under the NPGS menu. Press the O button on the keyboard to recenter the pattern.
  4. Save the pattern under the NPGS menu option. (Do not use save option in the File menu.)
  5. Close DesignCAD.

## VI. NPGS Run File Creation (.RF6)

1. Right click on the .DC2 file you wish to create a run file for, and select run file editor.
2. Set parameters nonstop writing mode .... in first tab
3. Set the center-to-center and line spacing.)
  - For high resolution lithography use  $2 - 3 \times$  the least significant bit on the DAC. (Highlight the value and press the + button twice.)
  - For low resolution lithography use a larger value as it will save some time in the exposure (50 – 75nm is fine).
  - Note: Line spacing is not used if you are only writing points or zero line width lines.
4. Set the dose. There are three types of dose.
  - Point: used only if you are writing single points or holes (i.e. photonic crystals).
  - Line: typically used only for narrow lines of less than 100nm.
  - Area: most commonly used dose. Use for polyfills, and non-zero line width lines.)
    - For 4% 495K PMMA in chlorobenzene an area dose of about  $400 - 575nC/cm^2$  should work for positive resist features. To

create negative resist features, a dose of at least  $9\times$  that should be used.

5. It is often useful to do a dose array on your first run to determine the exact dose necessary to obtain your desired structure. You can do this by changing the entity type from pattern to array. Then you have to adjust the doses of the array. (Note: array doses are shown as a percentage of the value you enter in the main dose window.)
6. Save file by pressing ok. (Note: NPGS does not allow spaces in file names, you may use underscores in their place.)

## VII. SEM Exposure Set-Up

1. Focus the SEM beam and slowly move your sample toward the beam with the XY joystick (right joystick). Do not image your sample directly, but move along the edge of the stub until you get to the gold focus standard.
2. Set your working distance to 6mm. (Double click on the WD in the data zone and enter 6mm.)
3. Bring gold standard into focus by adjusting Z. (Use the left Joystick)
4. Set the SEM aperture to aperture 2:  $10\mu\text{m}$ .
5. Use the Focus, stigmators, and magnification knobs to adjust the beam until you see a 10nm gold particle.
6. Reset the working distance to 6mm and adjust Z until gold particle is in focus again.
7. Turn on specimen current monitor. (Press the small left arrow on the right of the SEM image. This will expand into another window. Double click on the Spec. Current Monitor, and check the box for Spec. Curr. Monitor.)

8. Move the stage until you can see the Faraday cup. (It will be out of focus. This is OK. DO NOT adjust focus or stigmators.)
9. Increase magnification until you are only looking into the cup. (Screen will be black.)
10. Write down the specimen current from the monitor. You will need to put this value into NPGS later.
11. Move to the edge of your sample. Bring the image into focus by using Z. DO NOT adjust focus or stigmators.

### **VIII. NPGS Patterning Run**

1. Switch back to the NPGS computer and press the NPGS mode button twice. You should hear a series of beeps for the computer and the SEM should stop rastering. NPGS should now have control over the SEM.
2. The beam is now blanked so it is safe to move to the location you wish to create your pattern. (Use the XY joystick.)
3. Right click on the .RF6 run file you created, and select process run file.
4. Do not touch anything while the pattern is running.
5. Once all patterning is done move the sample away from the beam so you cannot accidentally expose the sample.

### **IX. Sample Extraction and System Shutdown**

1. Close the NPGS software. This should give electron beam control back to SmartSEM.
2. Press the Exchange button on the keyboard.
3. Once the gate valve is completely open, push specimen exchange rods in using the white plastic disk.
4. Screw rod into sample holder until snug.

5. Pull sample holder into airlock using the white disk. Pull until you hear the specimen exchange rods click. The rod retracted light will turn on once sample holder is fully in position.
6. Press vent on the airlock.
7. Pull airlock open with handle on bottom, and unscrew specimen exchange rods.
8. Slide sample holder off teflon block with your left hand while holding the airlock door with your right.
9. Push airlock door closed and press the pump button.
10. Log off of the SmartSEM software.

## **X. Sample Development**

The process chemicals used from sample development depend on the resist and in the case of PMMA the style you are using it in. When using PMMA to create features in positive resist, a 3 : 1 solution of isopropyl alcohol (IPA) : methyl isobutylketone (MIBK) is used. When making features in positive resist, acetone is used. In either case, place the sample directly into isopropyl alcohol after development.

Positive PMMA Development:

1. Place sample in 3 : 1 solution of IPA : MIBK for 45 seconds.
2. Put sample in IPA for 45 seconds.
3. Remove sample from IPA, and use compressed air or N<sub>2</sub> to gently dry sample. (It is important to do this carefully so there are no streaks or residue left on the surface.)

Negative PMMA Development:

1. Place sample in acetone for 45 seconds.

2. Put sample in IPA for 45 seconds.
3. Remove sample from IPA, and use compressed air or N<sub>2</sub> to gently dry sample. (It is important to do this carefully so there are no streaks or residue left on the surface.)

## **XI. Sample Inspection and Further Processing**

You can use either the light microscope or the electron microscope to inspect your pattern, though you should be aware that if you look at it in the SEM, it may not result in good liftoff if you are planning on coating it with another substance prior to inspection.

# Appendix D

## Fabrication of Silver Guided Mode Resonators

The fabrication recipe is as follows:

- Start with a double side polished SOI wafer. Our wafer was nominally  $500\mu m$  thick with a buried oxide layer of  $1.08\mu m$  and a device layer of about  $2.41\mu m$ .
- Clean the wafer.
- Deposit  $110nm$  of silicon dioxide to act as an isolation layer. Our layer was sputtered with a Kurt J. Lesker PVD75 system.
- Fabricate a silver grating on top of the isolation layer. Our grating was patterned using electron beam lithography but for large patterns, photolithography is recommended.
  - Spin coat the sample with electron beam resist. Our resist used was a 4% solution of 495k molecular weight polymethyl methacrylate (PMMA) in chlorobenzene produced by Microchem. The resist was spun on at 4,000RPM for 60 seconds, which yielded a resist layer that was approximately  $325nm$  thick.

- Expose the grating into the resist. We used a scanning electron microscope (SEM Zeiss Auriga Dual Beam Tool) that was controlled by an external scan generation system (Nabitys Nano Pattern Generation System in conjunction with a Wraith beam blanker)
- Develop the resist. Based on the  $400nC/cm^2$  dose applied to our resist, we developed our sample for 45 seconds in a 3:1 solution of isopropyl alcohol (IPA) : methyl isobutyl ketone (MIBK) followed by a 45 second rinse in IPA to stop the development process.
- Deposit an adhesion layer for the silver grating. If an adhesion layer is not deposited before the silver, the grating may be destroyed when trying to lift the PMMA off. We used a  $0.5nm$  chromium layer which was deposited via electron beam evaporation in a Lesker PVD75.
- Deposit the silver layer for the grating. We coated the sample with  $40nm$  of silver (evaporated via Kurt J. Lesker PVD75 system). Due to the deposition angle and the aspect ratio of the PMMA trenches, less than  $1/2$  of that lands on the surface of the  $SiO_2$  isolation layer. The fabricated grating has a thickness of  $18nm$  as measured by an SEM micrograph of a cross section created by a focused ion beam.
- Lift off the PMMA grating. In order to remove the PMMA grating, the sample was then placed in a bath of acetone for 30 minutes followed by a 5-10 second sonication (until the silver film is removed) followed by a rinse in IPA.
- Fabricate a silver reflector on top of the grating. In our case, a  $95nm$   $SiO_2$  cap layer was then added (sputter deposition via PVD75) on top of the grating followed by a  $125nm$  silver reflecting layer (evaporated via PVD75).

An example SEM micrograph of the final structure is shown in figure 4.1(b).

# Appendix E

## Fano Phase Derivation

Using the following form for the Fano resonance:

$$p(\delta) = \frac{i(\delta - q)}{(1 + i\delta)(1 + iq)},$$

we normalize the denominator and separate real and imaginary parts:

$$p(\delta) = \frac{i(\delta - q)(1 - i\delta)(1 - iq)}{(1 + \delta^2)(1 + q^2)} = \left( \frac{(\delta - q)}{(1 + \delta^2)(1 + q^2)} \right) ((\delta + q) + i(1 - q\delta)).$$

Since

$$|p(\delta)| = \frac{|\delta - q|}{\sqrt{(1 + \delta^2)(1 + q^2)}},$$

we can write

$$e^{i\phi} = \frac{p(\delta)}{|p(\delta)|} = \frac{((\delta + q) + i(1 - q\delta))}{\sqrt{(1 + \delta^2)(1 + q^2)}} \operatorname{sgn}(\delta - q).$$

The phase  $\phi$  of the response is then:

$$\begin{aligned} \cos \phi &= \frac{(\delta + q) \operatorname{sgn}(\delta - q)}{\sqrt{1 + \delta^2}}, \\ \sin \phi &= \frac{(1 - q\delta) \operatorname{sgn}(\delta - q)}{\sqrt{1 + \delta^2}}. \end{aligned}$$